Multifaceted moiré superlattice physics in twisted WSe₂ bilayers

S. J. Magorrian [1,2] V. V. Enaldiev [1,3,4] V. Zólyomi,[5] F. Ferreira [1,3] V. I. Fal'ko,[1,3,6,*] and D. A. Ruiz-Tijerina [7,†]

[1]*National Graphene Institute, University of Manchester, Booth Street E, Manchester, M13 9PL, United Kingdom*
[2]*Department of Physics, University of Warwick, Coventry, CV4 7AL, United Kingdom*
[3]*Department of Physics & Astronomy, University of Manchester, Oxford Road, Manchester, M13 9PL, United Kingdom*
[4]*Kotel'nikov Institute of Radio-engineering and Electronics of the Russian Academy of Sciences,*
11-7 Mokhovaya Street, Moscow, 125009 Russia
[5]*Hartree Centre, STFC Daresbury Laboratory, Daresbury, WA4 4AD, United Kingdom*
[6]*Henry Royce Institute for Advanced Materials, University of Manchester, Manchester, M13 9PL, United Kingdom*
[7]*Secretaría Académica, Instituto de Física, Universidad Nacional Autónoma de México, Ciudad de México, C.P. 04510, México*

Lattice reconstruction in twisted transition-metal dichalcogenide (TMD) bilayers gives rise to piezo- and ferroelectric moiré potentials for electrons and holes, as well as a modulation of the hybridization across the bilayer. Here, we develop hybrid $\mathbf{k} \cdot \mathbf{p}$ tight-binding models to describe electrons and holes in the relevant valleys of twisted TMD homobilayers with parallel (P) and antiparallel (AP) orientations of the monolayer unit cells. We apply these models to describe moiré superlattice effects in twisted WSe₂ bilayers, in conjunction with microscopic *ab initio* calculations, and considering the influence of encapsulation, pressure, and an electric displacement field. Our analysis takes into account mesoscale lattice relaxation, interlayer hybridization, piezopotentials, and a weak ferroelectric charge transfer between the layers, and it describes a multitude of possibilities offered by this system, depending on the choices of P or AP orientation, twist angle magnitude, and electron/hole valley.

I. INTRODUCTION

Moiré superlattices—emergent structures with long-range stacking periodicity—are a generic feature of van der Waals (vdW) heterostructures [1]. The presence of a small misalignment angle θ or lattice mismatch δ between their constituent layers amplifies the atomic periodicity as $a_M = a/\sqrt{\theta^2 + \delta^2}$, with a the monolayer lattice constant. Moiré superlattices induce a plethora of physical effects, such as long-range interlayer hybridization, leading to flat minibands with strongly correlated electronic states [2–10] and minibands for excitons in transition metal dichalcogenide (TMD) bilayers [11,12] at twist angles $\theta \ll 10°$, for which the moiré periodicity exceeds the exciton Bohr radius, thus affecting the system's optoelectronic properties [13–17]. Moreover, piezoelectric effects caused by lattice reconstruction in TMD bilayers [1,18,19] create periodic traps for charge carriers [20,21] and excitons [22], whereas interlayer charge transfer [23,24] induces ferroelectric polarization in these structures [25–27].

For marginal twist angles, moiré superlattices in twisted TMD homobilayers undergo strong lattice reconstruction, resulting in the formation of energetically preferential domains separated by networks of dislocationlike domain walls [1,18,28–30]. Due to the inversion asymmetry of TMD monolayers, the emerging domain structures differ for homobilayers with parallel (P, $\theta = \theta_{\mathrm{P}}$) and antiparallel (AP,

$\theta = \pi + \theta_{\mathrm{AP}}$) orientations of their unit cells (Fig. 1). Whereas for P bilayers the reconstructed moiré pattern consists of alternating triangular domains with MX′/XM′-type stacking (here, MX′ indicates that the bottom-layer metallic atoms are vertically aligned with the top-layer chalcogen atoms, as in bulk 3R structures), domains in AP bilayers are hexagonal and feature 2H-type stacking [18,19,28,30]. In-plane lattice reconstruction is accompanied by interlayer distance modulation across the supercell, which is of especial importance for the hybridization of the top valence band states at the Γ valley, formed by d_{z^2} and p_z orbitals of metals and chalcogens, respectively. A theoretical analysis of the electron properties in twisted TMD homobilayers must take into account the competition between various comparable factors, such as the piezoelectric potential, variation of the local band structure throughout the moiré superlattice with local stacking and interlayer distance, and interlayer (ferroelectric) charge transfer, relevant for P bilayers [23,24].

Here, we develop a unified approach for the theoretical description of electronic properties in twisted TMD homobilayers, taking into account interlayer hybridization, lattice reconstruction, piezoeffects, and interlayer charge transfer, and we demonstrate a great variety of emergent features when applying it to twisted WSe₂ bilayers. The proposed theory is based on the multiscale analysis [28] of atomic reconstruction in twisted TMD bilayers, combining elasticity theory with density functional theory (DFT) modeling of the interlayer adhesion energy, and the derivation of hybrid $\mathbf{k} \cdot \mathbf{p}$ tight-binding interpolation models for the hybridization of relevant conduction- or valence-band states based on DFT band

*vladimir.falko@manchester.ac.uk
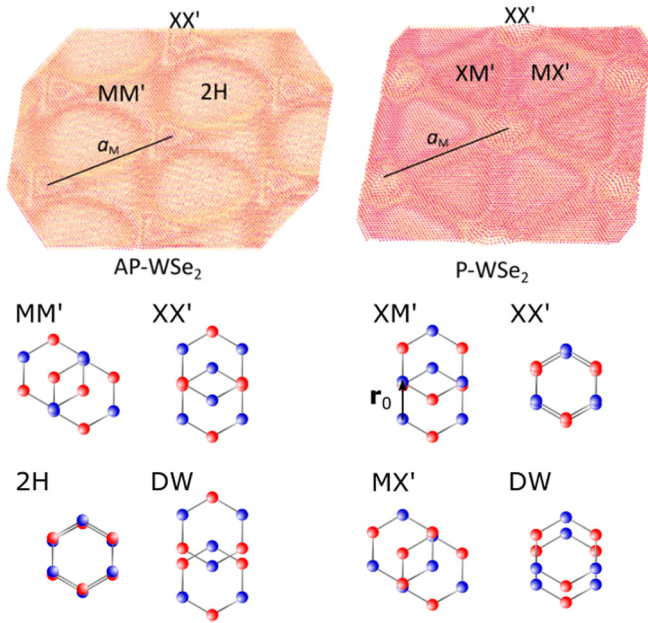†d.ruiz-tijerina@fisica.unam.mx

FIG. 1. Examples of reconstructed twisted WSe_2 bilayers with antiparallel (AP) and parallel (P) orientations of layers' unit cells. In-plane lattice reconstruction promotes the growth of hexagonal domains with 2H stacking for AP bilayers and triangular domains with XM'/XM' stackings for P bilayers, whereas out-of-plane relaxation leads to bulging of energetically unfavorable XX' stacking areas and domain walls. In the top panels, a_M indicates the moiré superlattice period. In our stacking notation, A_bA_t' indicates which atoms in the bottom and top layers are vertically aligned ($A_{t/b} = M$ for metal and X for chalcogen), using the more familiar notation 2H for MX' stacking in AP structures. The bottom panels illustrate the different stacking configurations, showing the in-plane stacking vector r_0.

structures. This allows us to trace the evolution of the potential energy landscapes for electrons and holes in the range of twist angles $0° < \theta_{P,AP} \leqslant 4°$. In addition, we analyze the effects of external perturbations, such as homogeneous strain, out-of-plane electric fields and pressure, on the energy and momentum of ground-state excitons in 3R- and 2H-stacked WSe_2 bilayers, within the framework of DFT.

Our findings for AP-WSe_2 bilayers are as follows:

(1) The Γ-point valence band maximum is modulated across the moiré supercell by a combination of piezopotential and strong interlayer hybridization. The large effective mass at the Γ point promotes the formation of strongly localized quantum dot (QD) states for holes at superlattice regions with 2H stacking for twist angles $1° < \theta_{AP} \lesssim 4°$.

(2) The K-point valence-band-edge variation throughout the supercell is dominated by the piezopotential. At marginal twist angles $\theta_{AP} \lesssim 1°$, piezopotential wells form QDs that localize K-point holes at corners of the domain wall structure with local XX' stacking (see Fig. 1). For $1° < \theta_{AP} < 2°$, these QD states mix to form narrow minibands for holes, realizing an SU_4 Hubbard model [31] on a mesoscale triangular lattice.

(3) The K-point conduction-band-edge modulation is also dominated by the piezopotential. For $\theta_{AP} \lesssim 1°$, MM' corners host QDs for electrons, giving rise to narrow bands for

$1° < \theta_{AP} < 2°$, and again realizing an SU_4 Hubbard model on a mesoscale triangular lattice.

(4) The Q-point conduction band energy landscape is dominated by the piezopotential for $\theta_{AP} \lesssim 1°$, forming QDs for electrons in MM' corners. The resulting QD states have a total spin and valley degeneracy factor of 12, realizing a large-N SU_N Hubbard model. For $\theta_{AP} \gtrsim 3°$, the conduction band edge shifts to 2H regions.

Our findings for P-WSe_2 bilayers are as follows:

(1) We quantify the stacking dependence of the ferroelectric interlayer charge transfer, and calculate the variation of areal density of electric dipole moments across the moiré supercell.

(2) The Γ-point valence band energy is highest at MX' and XM' sites, raised by the piezo- and ferroelectric potentials, forming a honeycomb lattice of quantum boxes for holes. For $1° < \theta_P \lesssim 4°$, hole states in these quantum boxes hybridize, mostly through interlayer tunneling, producing narrow minibands with Dirac-like features, realizing a narrow-band version of "mesoscale graphene."

(3) The K-point valence band edge behaves differently for $\theta_P \lesssim 1°$ and $1 < \theta_P < 2°$. In the former case, the band maximum appears at MX' and XM' regions of the superlattice, where the combined piezo- and ferroelectric potential energy is highest. In the latter case, interlayer hybridization dominates, shifting the band maxima to XX' corners, forming a mesoscale triangular QD lattice.

(4) The K-point conduction-band-edge modulation is dominated by the piezo- and ferroelectric potentials, defining quantum boxes for electrons at MX' and XM' regions across the whole studied range of misalignment angles. In contrast to K-point holes, interlayer tunneling of K-point electrons is suppressed, so that when overlapping minibands form for $\theta > 1°$, they are based on separate triangular QD arrays in the top and bottom layers.

(6) The Q-point conduction band edge is affected by variations of the resonant interlayer coupling and piezopotential across the moiré superlattice. For $\theta_P \lesssim 2°$, the Q-point conduction band edge appears at one-dimensional channels along two out of every three domain walls in each moiré supercell, as a consequence of the low symmetry of the Q-point states.

We note that the analysis presented here, corresponding to suspended WSe_2 bilayers, shows that the Γ-point valence band edge is systematically below that of the K point. However, their relative energies may depend on the sample encapsulation, as these two edges are formed by orbitals with different symmetry: The Γ-point states, formed by selenium d_z and tungsten p_z orbitals [32], are likely to interact more strongly with the environment [e.g., hexagonal boron nitride (hBN) substrate or encapsulation] than the K-point states, which consist of tungsten $d_{(x \pm iy)^2}$ orbitals. Therefore, for encapsulated bilayers the energy shift of the Γ point valence band edge will be also determined by its relative order with respect to energies of orbitals of the encapsulating material.

The main body of this paper is organized as follows: In Sec. II we overview the model for adhesion energy and lattice reconstruction [28], including the analysis of piezoelectric potentials [33]. In Sec. III, we employ *ab initio* DFT to analyze interlayer charge transfer and to develop interpolation
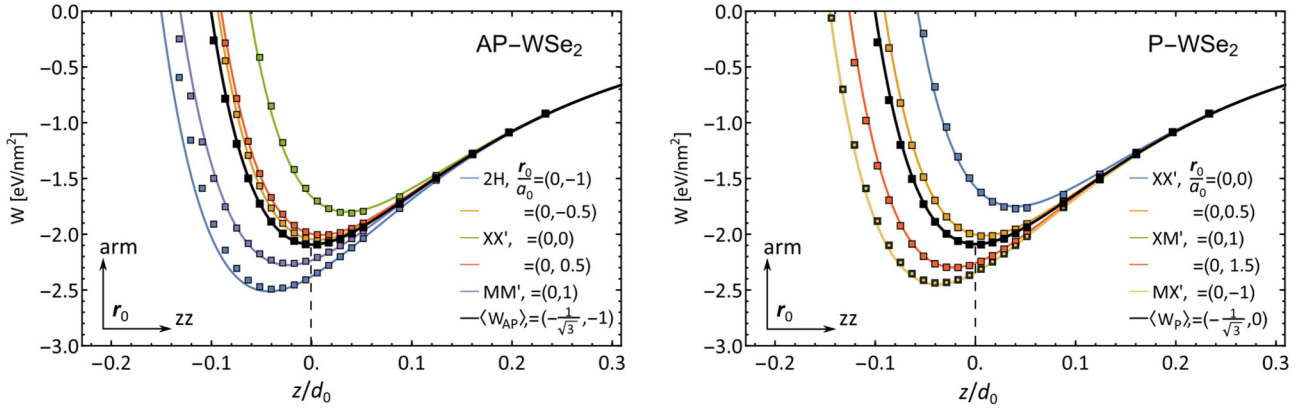
FIG. 2. Adhesion energy density of AP-WSe$_2$ (left) and P-WSe$_2$ (right) bilayers with various in-plane offsets $\mathbf{r}_0$ between the layers. $\mathbf{r}_0 = a_0(0, 0)$ corresponds to XX′ stacking, and $a_0 = 3.282/\sqrt{3}$ Å is the in-plane metal-chalcogen distance. Dots represent data calculated in Ref. [28] using the optB88 vdW-DFT functional, whereas lines are their fit by Eq. (1). Interlayer distances are counted from the configuration-averaged adhesion energy minimum $\langle W_{P/AP} \rangle_{\mathbf{r}_0}$. For AP bilayers the most stable configuration is 2H, being an elementary building block in the bulk 2H-TMD crystals. For P bilayers, the MX′ and XM′ configurations are mirror twins of each other and have the same d-dependence corresponding to the most energetically favorable configuration.

formulas for its analytical description in P bilayers. In Sec. IV we construct minimal effective Hamiltonians describing interlayer hybridization between relevant band-edge states at the Γ and K points. In Secs. V and VI we combine these Hamiltonians with lattice reconstruction, piezo- and ferroelectric potential contributions to study the conduction and valence-band-edge modulation across the moiré supercell in twisted WSe$_2$ bilayers, and we compute the corresponding moiré minibands in Sec. VII. Finally, in Sec. VIII we discuss how the band-edge position across the Brillouin zone of WSe$_2$ bilayers can be modified by external electric fields, strain, and encapsulation using, e.g., hBN.

II. INTERLAYER ADHESION ENERGY

We begin with an analysis of the lattice structure of twisted WSe$_2$ bilayers, based on a previously established model for the adhesion energy $W_{P/AP}$ between two aligned monolayers [28] (see Fig. 2):

$$W_{P/AP}(\mathbf{r}_0, z) = \overline{W} + \gamma z^2 + A_1 e^{-\sqrt{G^2 + \rho^{-2}} z} f_s(\mathbf{r}_0)$$
$$+ A_2 e^{-Gz} f_{s/a}(\mathbf{r}_0),$$
$$f_s(\mathbf{r}_0) = 2\cos\left(2\pi\frac{x_0}{a}\right)\cos\left(\frac{2\pi}{\sqrt{3}}\frac{y_0}{a}\right) + \cos\left(\frac{4\pi}{\sqrt{3}}\frac{y_0}{a}\right),$$
$$f_a(\mathbf{r}_0) = 2\sin\left(2\pi\frac{x_0}{a}\right)\cos\left(\frac{2\pi}{\sqrt{3}}\frac{y_0}{a}\right) - \sin\left(\frac{4\pi}{\sqrt{3}}\frac{y_0}{a}\right).$$
$$(1)$$

Here, $\mathbf{r}_0 = (x_0, y_0)$ is a lateral offset between layers characterizing different stacking configurations [$\mathbf{r}_0 = (0, 0)$ for XX′ stacking corresponding to overlaying of chalcogens in two layers] in a Cartesian reference frame with x and y axes along zigzag and armchair directions, respectively, and $a = 3.282$ Å is the lattice constant. The interlayer distances $d = z + d_0$ in Eq. (1) are counted from an optimal interlayer distance d_0 obtained from the configuration-averaged adhesion energy profile $\langle W_{P/AP} \rangle_{\mathbf{r}_0} = -\sum_{n=1,2,3} C_n/(d_0 + z)^n \approx$

$\overline{W} + \gamma z^2$, where after the second approximate equality we leave only the lowest terms in a Taylor series over z ($\gamma = 190$ eV nm^{-4}). In Eq. (1), $G = 4\pi/a\sqrt{3}$ is the magnitude of the basis reciprocal vectors of monolayer WSe$_2$, $\mathbf{G}_{1,2} = G(\pm\frac{\sqrt{3}}{2}, \frac{1}{2})$. The values of the fitting parameters $C_{1,2,3}$, $A_{1,2}$ and ρ are listed in Table I.

Linearization of the exponentials in Eq. (1), followed by minimization with respect to z, gives an expression for the optimal interlayer distance variation with stacking configuration [28]:

$$z_{P/AP}(\mathbf{r}_0) = \frac{1}{2\gamma}[A_1\sqrt{G^2 + \rho^{-2}} f_s(\mathbf{r}_0) + A_2 G f_{s/a}(\mathbf{r}_0)]. \quad (2)$$

Equation (2) leads to a slightly larger interlayer distance (≈ 6.66 Å) for 2H-stacked WSe$_2$ bilayers than that extracted from experiments with bulk samples (≈ 6.48 Å [34]). This is because vdW-DFT calculations overestimate $d_0 = 6.89$ Å used as a reference interlayer distance, while γ, which determines the amplitude of the optimal distance variation, is computed more accurately [35]. This is confirmed by its comparison with the frequency of the layer breathing mode measured using Raman scattering (see SI in Ref. [28]). Below, to compensate for the discrepancy between the calculated and measured interlayer distances for 2H bilayers, we will use a shifted value $d_0 = 6.71$ Å for the reference interlayer distance in DFT calculations of the band structures.

In moiré superlattices of twisted WSe$_2$ bilayers, the existence of an energetically favorable local stacking configuration promotes lattice reconstruction. As shown in Ref. [28],

TABLE I. Interpolation parameters for the adhesion energy density, Eq. (1), of WSe$_2$ bilayers. Equivalent to the results presented in Ref. [28].

C_1, eV nm^2	C_2, eV nm^6	C_3, eV nm^{10}	A_1, eV/nm^2	A_2, eV/nm^2	ρ nm
0.1488	0.2478	-0.0395	0.1428	0.0275	0.0497

the magnitude of the twist angle distinguishes between strong ($\theta_{P/AP} < \theta^*_{P/AP}$) and weak ($\theta_{P/AP} \gtrsim \theta^*_{P/AP}$) reconstruction regimes, where $\theta^*_P = 2.5°$ and $\theta^*_{AP} = 1°$. The former regime is characterized by the expansion of the regions with the lowest energy into domains separated by domain wall networks, whereas for the latter domains do not form, leaving a smooth variation of the interlayer atomic registry across the supercell. Qualitatively, strong reconstruction happens when the energy gain from developing the lowest energy domains outweighs the elastic energy cost of domain wall formation. Since the gain grows as the square of the superlattice period ($\propto a_M^2$) and the cost linearly ($\propto a_M$), the moiré superlattice experiences a commensurate-incommensurate transition only at sufficiently large periods, i.e., below some critical angle, as described above.

For twisted AP bilayers, the reconstructed moiré superlattice consists of 2H-stacking domains, each analogous to the layer alignment found in bulk crystals. These domains are separated by a network of domain walls, each of which is a full screw dislocation. The other high symmetry registries, XX′ and MM′, occupy sites of the domain wall network (Fig. 3).

In the moiré supercells of P-WSe$_2$ bilayers there are two registries, MX′ and XM′, representing the same energetically favorable layer alignment, analogous to 3R stacking in bulk crystals. This allows an easier transition into the commensurate phase for P bilayers (see Fig. 5), as in this case triangular MX′ and XM′ domains are separated by less energetically expensive partial-screw-dislocation-like domain walls [28].

In-plane strain $u_{ij}^{t/b}$, caused by reconstruction, induces piezoelectric charges

$$\rho^{t/b} = e_{11}^{t/b}\big[2\partial_x u_{xy}^{(t/b)} + \partial_y\big(u_{xx}^{(t/b)} - u_{yy}^{(t/b)}\big)\big], \quad (3)$$

in the top and bottom layers of P- and AP-WSe$_2$ structures, due to the lack of inversion symmetry of the individual layers (the piezocoefficient for WSe$_2$ monolayers is $|e_{11}^{t/b}| = 2.03 \times 10^{-10}$ C/m [36]). For AP bilayers, both layers have equal piezocharge densities as a result of a sign compensation between the piezocoefficients ($e_{11}^t = -e_{11}^b$) and the strain tensors ($u_{ij}^t = -u_{ij}^b$) of opposite layers. The latter is due to the tendency of the monolayers to deform toward each other. In Fig. 3 we show the distribution of piezocharges, piezopotentials, and interlayer distances in the two reconstruction regimes for AP-WSe$_2$ bilayers. At small twist angles $\theta_{AP} < \theta^*_{AP}$, the piezocharge density extrema appear at the corners of hexagonal 2H domains, with opposite signs in XX′ and MM′ areas. For large twist angles $\theta_{AP} \gtrsim \theta^*_{AP}$, the piezocharge and potential modulation amplitudes decay significantly.

Because of the negligible energy cost of bending deformations of WSe$_2$ monolayers [28] as compared with in-plane strain and adhesion energy variation, interlayer distance modulation, expressed by Eq. (2) with local lateral shift $\mathbf{r}_0(\mathbf{r}) = \theta_{P/AP}\hat{z} \times \mathbf{r} + \mathbf{u}^t - \mathbf{u}^b$, occurs in both the strong and weak reconstruction regimes, as shown in the top panels of Figs. 3 and 5.

The spatial variation of the interlayer distance in twisted P and AP bilayers can be expressed as a Fourier series over moiré superlattice reciprocal vectors $\mathbf{g}_j$ [see Eq. (29)
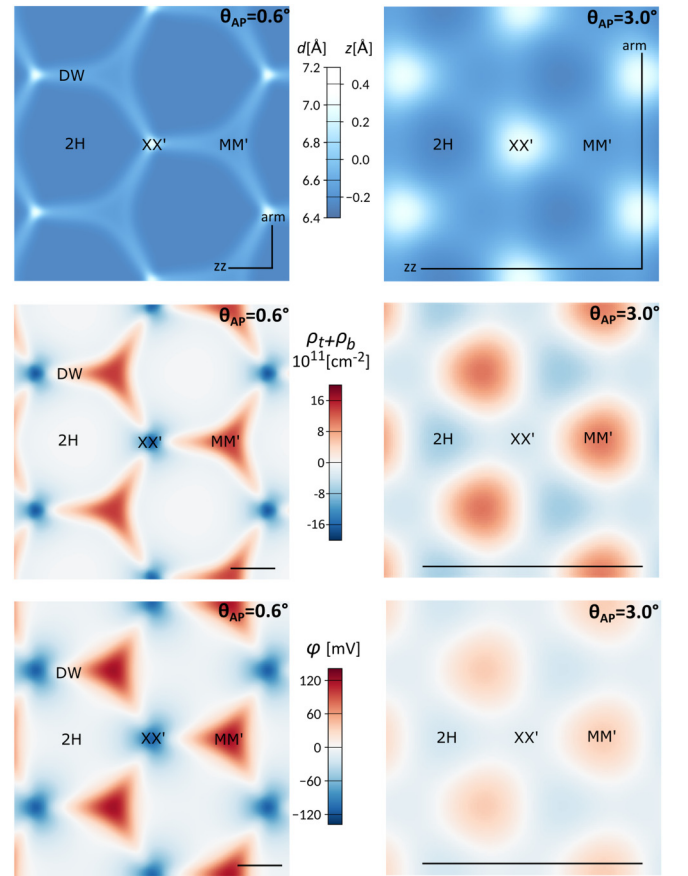

FIG. 3. Maps of interlayer distance $d(\mathbf{r}) = d_0 + z_{AP}[\mathbf{r}_0(\mathbf{r})]$ (top), total piezocharge density in the top and bottom layers $\rho_t + \rho_b$ (middle), and piezoelectric potential $\varphi_t = \varphi_b \equiv \varphi$ (bottom), in the reconstructed superlattices of twisted AP-WSe$_2$ bilayers at two different twist angles $\theta_{AP} = 0.6°$ (left panels) and $\theta_{AP} = 3°$ (right panels). We used $d_0 = 6.71$ Å as the reference distance and local lateral offset $\mathbf{r}_0(\mathbf{r}) = \theta_{P/AP}\hat{z} \times \mathbf{r} + \mathbf{u}^t - \mathbf{u}^b$ for producing the interlayer distance maps. For calculation of piezocharge densities and piezopotential we took into account screening coming from polarization of filled bands and encapsulation in hBN (see Appendix E). The piezocharge magnitudes remain the same for smaller twist angles. The scale bar in all panels is 10 nm. On the top panels we show armchair (arm) and zigzag (zz) crystallographic axes in each layer; all maps are shown at the same crystallographic orientation.

below]:

$$z_{P/AP}[\mathbf{r}_0(\mathbf{r})] = z_0 + \sum_j \big[z_j^s \cos(\mathbf{g}_j \cdot \mathbf{r}) + z_j^a \sin(\mathbf{g}_j \cdot \mathbf{r})\big], \quad (4)$$

where

$$z_j^s + i z_j^a = \frac{2}{S_{sc}} \int_{sc} d^2\mathbf{r} \, z_{P/AP}[\mathbf{r}_0(\mathbf{r})]e^{i\mathbf{g}_j \mathbf{r}}$$

are Fourier coefficients, with $z_0 \equiv z_0^s$ and $z_j^a = 0$ for P bilayers, and S_{sc} is the supercell area. For not too small angles ($\theta_{P/AP} \gtrsim 1°$) the summation in Eq. (4) involves a few stars of the moiré harmonics (see Appendix F), simplifying the calculation of miniband structures presented in Sec. VII.
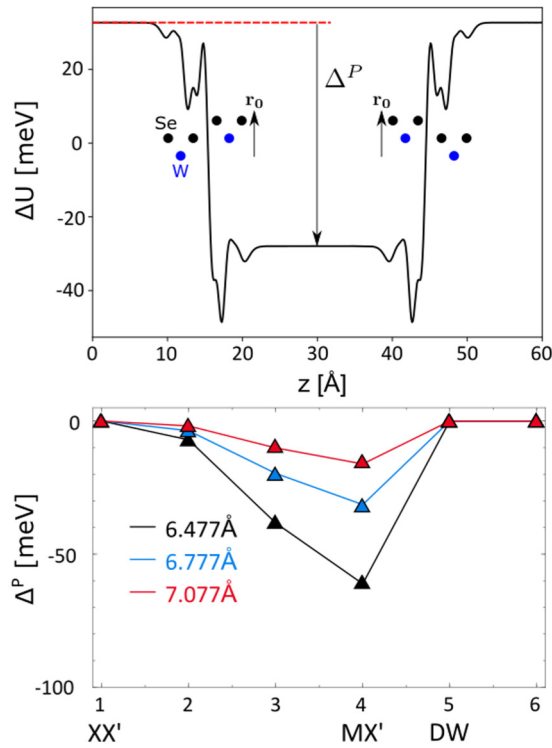
FIG. 4. Top panel: Difference between the plane-averaged local potential for XM′-stacked bilayer WSe$_2$ with $d = 6.477$ Å (calculated using a supercell containing two images of the bilayer σ_h reflected relative to each other as shown in the schematic) and that from the sum of isolated monolayers. The net charge transfer between the layers gives a potential difference across the bilayer, with the majority of the potential drop taking place between the layers. Bottom panel: Dependence of the difference between the DFT-calculated vacuum potentials (triangles) Δ^P (indicated in the top panel) on interlayer distance and stacking configuration, fitted (lines) according to Eq. (5).

III. INTERLAYER CHARGE TRANSFER FROM DENSITY FUNCTIONAL THEORY MODELING OF P-WSe$_2$ BILAYERS

Using the interlayer adhesion model described in Ref. [28] and set out above, we determined the stacking patterns and interlayer distances realized in twisted WSe$_2$ bilayers. To find the resulting band energies, we constructed the model Hamiltonians presented below, fully parametrized using DFT band structure calculations for aligned bilayers with a range of local in-plane offsets $\mathbf{r}_0$ and interlayer distances d, as discussed in detail in Appendix D.

In these DFT calculations, P-stacked bilayers were placed in a periodic three-dimensional box with a separation of 30 Å between the mean planes of the repeated bilayer images, to ensure that no interaction occurred between them. For P-stacked bilayers, the lack of inversion symmetry in the monolayer means that, away from certain high-symmetry configurations, layer interchange is not a symmetry operation. Therefore, it is possible for layer-asymmetric interband hybridization to give rise to some interlayer charge transfer for XM′ and MX′ bilayers [23], resulting in a potential jump across the WSe$_2$ bilayer, for XM′ stacking, shown in Fig. 4.
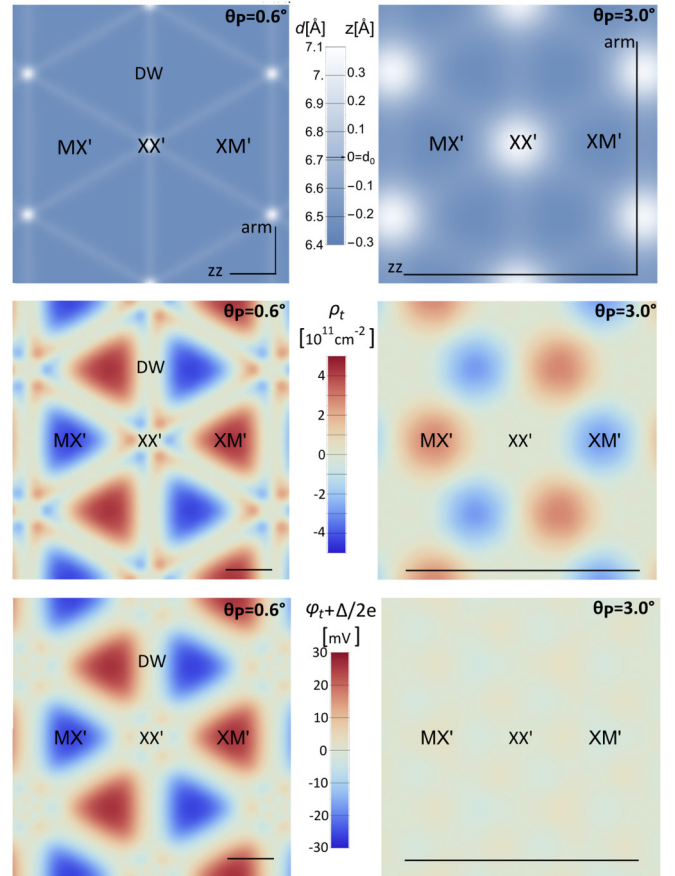
FIG. 5. Maps of the interlayer distance $d(\mathbf{r}) = d_0 + z_P[\mathbf{r}_0(\mathbf{r})]$ (top), sum of the piezo- and ferroelectric charge densities in top layer (middle), and their total potential (bottom) for twisted P-WSe$_2$ bilayers at different twist angles $\theta_P = 0.6°$ (left panels) and $\theta_{AP} = 3°$ (right panels). In the bottom layer the charges and potential have opposite signs. For the interlayer distance maps we used the parameters discussed in the caption of Fig. 3. The scale bar is 10 nm in all panels. The monolayer zigzag (zz) and armchair (arm) crystallographic axes are shown in the top panels; all maps are shown at the same crystallographic orientation.

We therefore construct supercells containing two P-stacked bilayers separated by a large vacuum, with the second supercell mirror-reflected with respect to the first: this avoids the need to artificially resolve the potential mismatch at the supercell boundary [37].

The $\mathbf{r}_0$- and z-dependencies of the electron potential energy jump across the WSe$_2$ bilayer can be described as

$$\Delta^P(\mathbf{r}_0, z) = \Delta_a^P(z) f_a(\mathbf{r}_0), \qquad (5)$$

where the z-dependent function $\Delta_a(z)$ is fitted by a simple exponential (see Fig. 4 and Sec. IV A). The magnitude of the jump is maximal for XM′ and XM′ stackings, reaching 66 meV. This is produced by the charge double layer located between the inner chalcogen sublayers, characterized by the areal polarization density (in CGS units)

$$P \approx \frac{\Delta^P}{4\pi e}. \qquad (6)$$

TABLE II. Fitting parameters for interlayer-distance-dependent functions in Hamiltonian Eq. (7) for Γ-point state hybridization (each function was fitted by $Ae^{-q_A z}$) and ferroelectric parameters for preferential stacking domains.

	A	q_A, Å^{-1}
t_0	0.5 eV	1.0
t_1	20.3 meV	2.4
t_2^{AP}	2.1 meV	2.3
$v_{\Gamma,0}$	0.5 eV	0.4
$v_{\Gamma,1}$	3.3 meV	3.3
Δ_a	14.1 meV	2.2
$\varepsilon_{A'}$	−5.8 eV	N.A.
$\Delta^{MX'} = -\Delta^{XM'} = 66.0\,\text{meV}$		
$P^{MX'} = -P^{XM'} = 3.7 \times 10^{-3}\,e/\text{nm}$		

The ferroelectric polarization is opposite in MX′ and XM′ domains, attaining a value (see Table II)

$$P^{XM'} = -P^{MX'} = 3.7 \times 10^{-3} \frac{e}{\text{nm}}.$$

In Fig. 5 we show maps of interlayer distance, sum of piezo- and ferro-charge densities, and electric potential in the top layer for the two reconstruction regimes. For marginal twist angles $\theta_P < \theta_P^*$, ferrocharges determine the polarization of XM′ and MX′ domains, while their effect is compensated by piezocharges along domain walls, giving the domain corners a charge opposite to that of the main body. For larger twist angles $\theta_P \gtrsim \theta_P^*$, piezo- and ferrocharges almost completely suppress each other, leading to vanishingly small total interlayer charge polarization (see Fig. 5).

In Fig. 6, we show DFT-calculated bands for high-symmetry stacking configurations, choosing the optimal interlayer distance for each configuration, as set out in Sec. II. The band energies are aligned with respect to their corresponding vacuum levels, using the mean of the two vacuum energies at either side of a P-stacked bilayer. The Γ-point valence band edge shows strong variation with stacking because interlayer hybridization at Γ is strong, and therefore sensitive to changes in stacking configuration and interlayer distance. By contrast, the stacking-dependent variation of the K-point valence band edge is weaker, but still present.

IV. MINIMAL MODELS FOR RESONANT HYBRIDIZATION OF CONDUCTION/VALENCE STATES IN BILAYERS

In a reconstructed twisted bilayer, the stacking orders and interlayer distances, and hence the interlayer hybridization and band-edge state energies, vary continuously across the moiré supercell. To determine the band energies in the different regions of the twisted bilayer, it is therefore necessary to interpolate and understand the $(\mathbf{r}_0, z)$-dependence seen in the DFT results. We have developed and applied models for interlayer coupling between the relevant conduction- and valence-band-edge states described in the following sections, taking into account the competing effects of changes in stacking order and interlayer distance, and revealing the underlying symmetries and physical mechanisms responsible

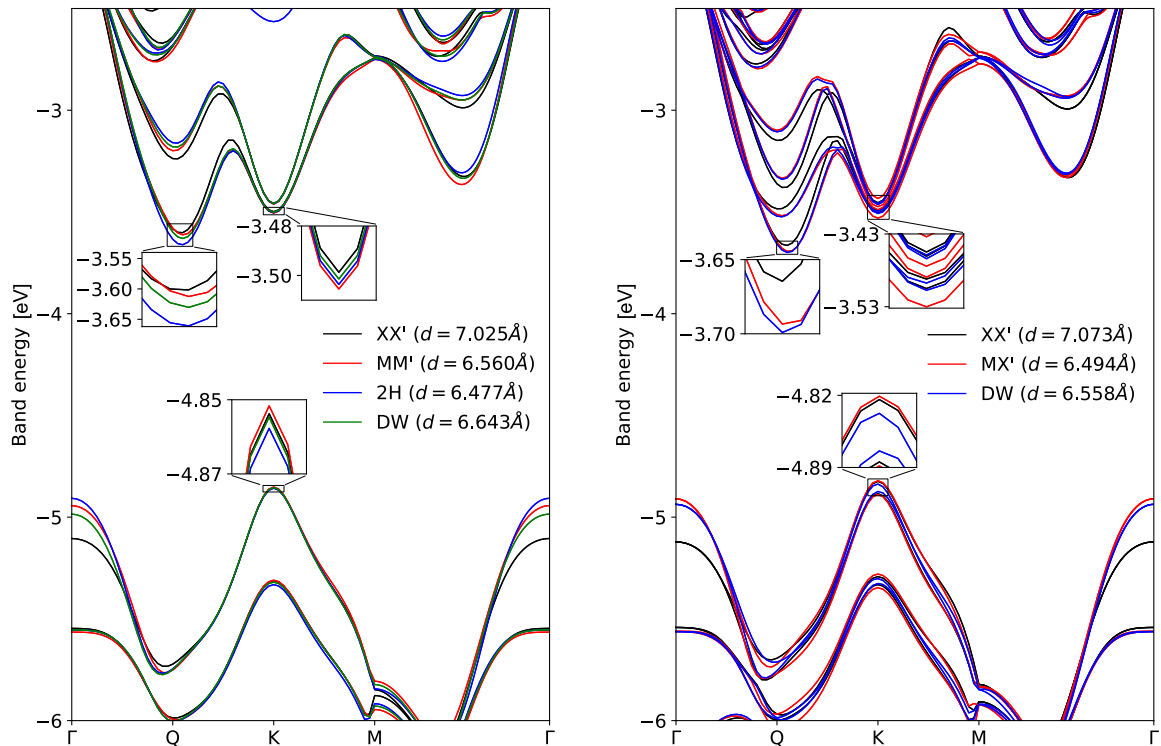FIG. 6. Band energies for high-symmetry configurations of AP-stacked (left panel) and P-stacked (right panel) WSe$_2$ bilayers. The vacuum level is set to 0 eV (for MX′ stacking in the P case, the mean of the two vacuum levels at either side of the bilayer). The interlayer distances d are given by Eq. (2) with a reference distance d_0. The structure parameters for the monolayer are taken from experiment.

for the demonstrated behavior. Since in P bilayers the interlayer charge transfer, induced by nonresonant hybridization between filled valence- and empty conduction-band states, is intrinsically taken into account in DFT computations, the weak ferroelectric effect in the P orientation is captured in the models below. Due to the nonuniform strain patterns that arise from atomic reconstruction, a complete picture of the varying band energies in the moiré superlattice must also include a contribution that takes piezoelectric effects into account.

In Secs. IV A and IV B we present the resulting resonant hybridization Hamiltonians for Γ-point states in the valence band, and K-point states in the valence and conduction bands for P- and AP-aligned bilayers. The corresponding Hamiltonian for Q-point states in the conduction band is discussed in Sec. IV C. In each of these cases we offer interpolation formulas applicable to both P and AP orientations of the bilayers and illustrate the resulting variation of the corresponding band edges throughout the moiré supercells using numerically computed maps for both $\theta_{P/AP} < \theta^*_{P/AP}$ and $\theta_{P/AP} < \theta^*_{P/AP}$.

A. Γ-point valence band for P and AP bilayers

Hybridization between the local Γ-point VBM of two WSe$_2$ monolayers can be described by the following Hamiltonian:

$$H^{P/AP}_{\Gamma,VB} = H^{P/AP}_{\Gamma} + \delta H^{P/AP}_{\Gamma}. \tag{7}$$

Here, the dominant contribution to the coupling reads

$$H^{P/AP}_{\Gamma} = \varepsilon^{P/AP}_{\Gamma} \Lambda_0 + T^{P/AP}_{\Gamma} \Lambda_x - \frac{S^{P/AP}_{\Gamma}}{2} \Lambda_z,$$

$$\delta H^{P/AP}_{\Gamma} = \delta\varepsilon^{P/AP}_{\Gamma} \Lambda_0 + \delta T^{P/AP}_{\Gamma}(\boldsymbol{r}_0, d) \Lambda_x, \tag{8}$$

where Λ_0 is a 2×2 unit matrix, and $\Lambda_{x,y,z}$ are the Pauli matrices acting on the layer subspace. The matrix elements are

$$\varepsilon^{P/AP}_{\Gamma}(\boldsymbol{r}_0, z) = \varepsilon_{A'} + v^{P/AP}_{\Gamma,0}(z),$$

$$T^{P/AP}_{\Gamma}(\boldsymbol{r}_0, z) = \frac{t^{P/AP}_0(z)}{2} + \frac{t^{P/AP}_1(z)}{2} f_s(\boldsymbol{r}_0),$$

$$S^{P}_{\Gamma}(\boldsymbol{r}_0, z) = \Delta^{P}(\boldsymbol{r}_0, z), \; S^{AP}_{\Gamma}(\boldsymbol{r}_0, z) = 0, \tag{9}$$

$$\delta\varepsilon^{P/AP}_{\Gamma}(\boldsymbol{r}_0, z) = v^{P/AP}_{\Gamma,1}(z) f_s(\boldsymbol{r}_0),$$

$$\delta T^{AP}_{\Gamma}(\boldsymbol{r}_0, z) = \frac{t^{AP}_2(z)}{2} f_a(\boldsymbol{r}_0), \; \delta T^{P}_{\Gamma}(\boldsymbol{r}_0, z) = 0.$$

Here, $T^{P/AP}_{\Gamma}$ and $\delta T^{P/AP}_{\Gamma}$ describe resonant hybridization of the monolayer states, whereas $\varepsilon^{P/AP}_{\Gamma}$ and $\delta\varepsilon^{P/AP}_{\Gamma}$ are due to coupling of one monolayer's top valence band at the Γ point with remote bands in the opposite layer. Functions $t^{P/AP}_{0,1}(z)$ and $v^{P/AP}_{\Gamma;0,1}(z)$, characterizing the interlayer distance dependence of the matrix elements, are found to be the same for P and AP configurations (i.e., $t^{P}_0 = t^{AP}_0 \equiv t_0$, $t^{P}_1 = t^{AP}_1 \equiv t_1$, $v^{P}_{\Gamma,0} = v^{AP}_{\Gamma,0} \equiv v_{\Gamma,0}$, $v^{P}_{\Gamma,1} = v^{AP}_{\Gamma,1} \equiv v_{\Gamma,1}$) from analysis of the DFT results (see Fig. 7), allowing us to remove the P and AP superscripts in the following discussion. We find that these functions can be described by exponential functions, $A(z) = A e^{-q_A z}$, and parametrize them in Table II. In Eq. (9), $\varepsilon_{A'}$ is the energy of the top valence band state at the BZ center

FIG. 7. (a) Interlayer distance dependence of the parameters in the effective Hamiltonian Eq. (7) describing hybridization of Γ-states in P and AP bilayers, extracted from DFT data. The analysis shows that $t^{AP}_{0,1}(d) = t^{P}_{0,1}(d)$ and $v^{AP}_{\Gamma;0,1}(d) = v^{P}_{\Gamma;0,1}(d)$. (b) Twist-angle dependence of piezopotential (for AP) and difference of piezopotentials in two layers (for P) in various areas of the moiré supercell. Comparing the piezopotential magnitudes with the values of major terms in the model Eq. (7) (t_0 and $v_{\Gamma,0}$, shown in top panel), we conclude that accounting for the piezopotential is essential to correctly establish the form of the Γ-point valence band edge at marginal twist angles $\theta_{AP} \lesssim \theta^*_{AP}$, whereas in the weak reconstruction regime $\theta_{AP} \gtrsim \theta^*_{AP}$ the effect of piezopotential is small.

of an isolated WSe$_2$ monolayer, and S^{P}_{Γ} describes the electron energy jump due to the interlayer charge transfer introduced in the previous section. Note that this term vanishes in AP bilayers as they are centrosymmetric.

Decomposition of $H^{P/AP}_{\Gamma,VB}$ into $H^{P/AP}_{\Gamma}$ and $\delta H^{P/AP}_{\Gamma}$ reflects the hierarchy of these two contributions to the model. Comparing t_0 and t_1 with t^{AP}_2, and $v_{\Gamma,0}$ with $v_{\Gamma,1}$, shown in Fig. 7(a), we conclude that

$$t_0 \gg t_1 \gg t^{AP}_2, \quad v_{\Gamma,0} \gg v_{\Gamma,1}. \tag{10}$$

Therefore, $H_\Gamma^{P/AP}$ gives the dominant effect of interlayer hybridization, while $\delta H_\Gamma^{P/AP}$ characterizes only its fine features (see Appendix B). For this reason, it is the variation of interlayer distance across the moiré supercell that is mainly responsible for the position dependence of the Γ-point band-edge energy in the supercell of twisted WSe_2 bilayers (see Sec. V) [38].

B. Interlayer hybridization at the K point

Unlike the spin-degenerate Γ-point states considered above, the valence and conduction states of monolayers at the K points are split by the atomic spin-orbit (SO) interaction. This leads to spin-valley locking of the K-valley states [39] and, consequently, to different hybridization between them in P and AP bilayers. For P bilayers, the local valence- and conduction band-edge states at the τK point ($\tau = \pm 1$) are formed by resonantly coupled monolayer states with spin projection $s = -\tau$ and $s = \tau$, respectively, whereas for AP-bilayers hybridization at the τK point is off-resonance, because same-spin valence and conduction band-edge states in opposite layers are shifted in energy due to the SO splitting of monolayer states.

Nonetheless, an effective Hamiltonian describing hybridization of the monolayer band-edge states in the τK point of P/AP bilayers can be represented in the form of Eq. (7) ($\alpha = $ CB, VB for conduction and valence band, respectively):

$$H_{\alpha,\tau K}^{P/AP} = \varepsilon_\alpha^{P/AP}\Lambda_0 - \frac{S_\alpha^{P/AP}}{2}\Lambda_z + \frac{T_{\alpha,\tau}^{P/AP}}{2}\Lambda_+$$
$$+ \frac{T_{\alpha,\tau}^{P/AP*}}{2}\Lambda_-. \tag{11}$$

Here, $\Lambda_\pm = \Lambda_x \pm i\Lambda_y$, and the matrix elements are

$$T_{VB,\tau}^{P}(\mathbf{r}_0, z) = t_{VB}^{P}(z)T_\tau(x_0, y_0),$$

$$T_{VB,\tau}^{AP}(\mathbf{r}_0, z) = t_{VB}^{AP}\left(z\right)T_\tau\left(x_0, y_0 + \frac{a}{\sqrt{3}}\right),$$

$$T_{CB,\tau}^{P}(\mathbf{r}_0, z) = t_{CB}^{P}(z)T_\tau(x_0, y_0),$$

$$T_{CB,\tau}^{AP}(\mathbf{r}_0, z) = t_{CB}^{P}(z)T_\tau(x_0, y_0),$$

$$S_{CB/VB}^{P}(\mathbf{r}_0, z) = \Delta^{P}(\mathbf{r}_0, z),$$

$$S_\alpha^{AP}(\mathbf{r}_0, z) = \lambda_\alpha\left[\Delta_\alpha^{SO} + \tilde{\Delta}_{\alpha,1}^{SO}(z)f_s(\mathbf{r}_0) + \tilde{\Delta}_{\alpha,2}^{SO}(z)f_a(\mathbf{r}_0)\right],$$

$$\varepsilon_\alpha^{P/AP}(\mathbf{r}_0, z) = \varepsilon_\alpha - v_0(z) - v_{\alpha,1}^{P/AP}(z)\left[\cos(\chi_{P/AP})f_s(\mathbf{r}_0)\right.$$
$$\left. - \lambda_\alpha\sin(\chi_{P/AP})f_a(\mathbf{r}_0)\right], \tag{12}$$

where $\chi_P = 0$, $\chi_{AP} = \pi/4$, $\lambda_{VB} = 1$, $\lambda_{CB} = -1$, and we have defined the function

$$T_\tau(x, y) = e^{i\tau\frac{4\pi x}{3a}} + 2e^{-i\tau\frac{2\pi x}{3a}}\cos\left(\frac{2\pi y}{a\sqrt{3}}\right).$$

In Eq. (12), $t_\alpha^{P/AP}(z)$ is the tunneling parameter between bands $\alpha = $ CB, VB of the two layers. For P bilayers, S_α^{P} accounts for the potential energy drop caused by the interlayer charge transfer, while for AP bilayers S_α^{AP} represents the SO splitting in the corresponding band, containing the monolayer SO splitting Δ_α^{SO}, as well as small z-dependent corrections $\tilde{\Delta}_1^{SO}$ and $\tilde{\Delta}_{\alpha,2}^{SO}$. The DFT analysis displayed in
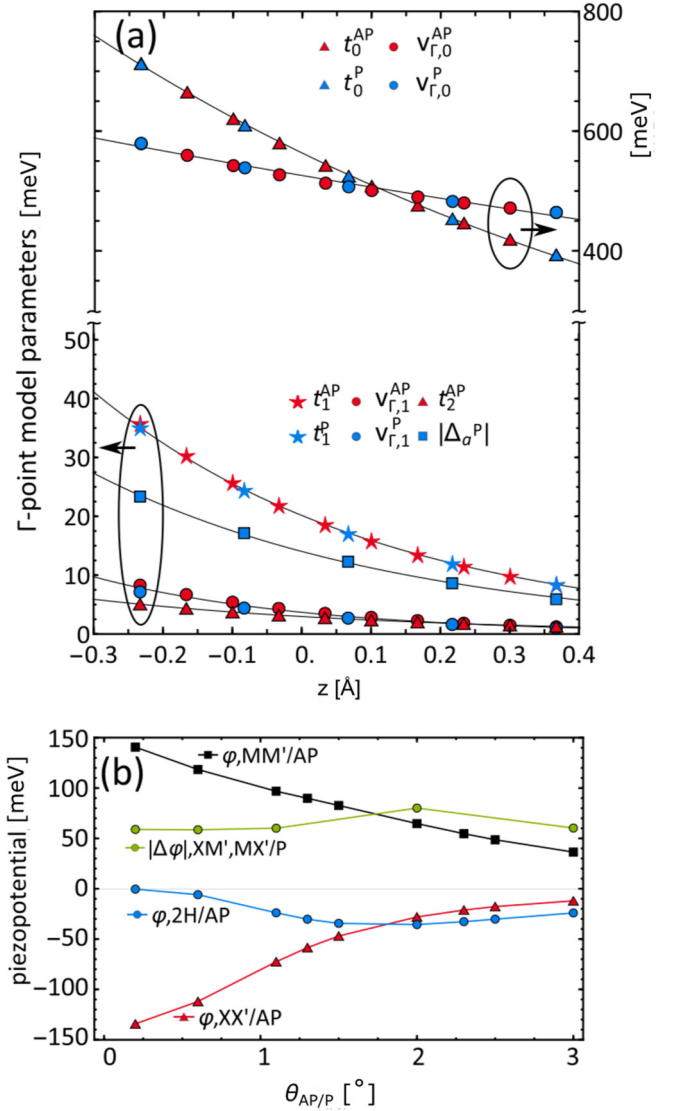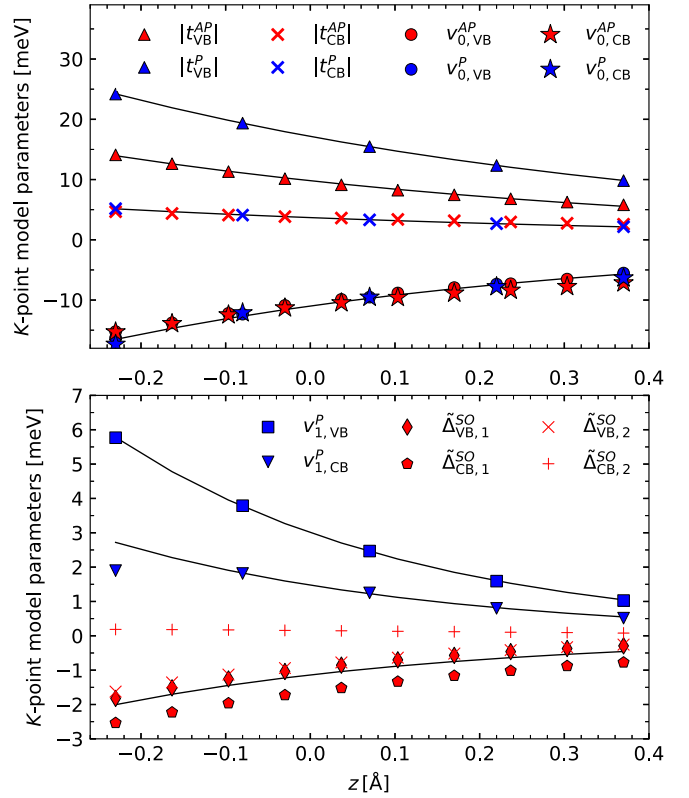

FIG. 8. Interlayer distance dependence of the parameters in the effective Hamiltonian Eq. (11) describing hybridization of the highest valence and lowest conduction bands at the K point. DFT results are shown with symbols, whereas lines show the interpolation described in Table III, with the definition $\tilde{\Delta}_{CB,1}^{SO} = \tilde{\Delta}_{VB,1}^{SO} = \tilde{\Delta}_{VB,2}^{SO} \equiv \tilde{\Delta}_1^{SO}$.

Fig. 8 shows that $|t_{CB}^{P}| = |t_{CB}^{AP}| \equiv |t_{CB}|$, and also that $\tilde{\Delta}_{CB,1}^{SO} = \tilde{\Delta}_{VB,1}^{SO} = \tilde{\Delta}_{VB,2}^{SO} \equiv \tilde{\Delta}_1^{SO}$ and $|\Delta_1^{SO}|, |\Delta_{CB,2}^{SO}| \ll |\Delta_{CB/VB}^{SO}|$. In the last line of Eq. (12), ε_{CB} and ε_{VB} are the monolayer K-point conduction- and valence-band-edge energies, whereas $v_{CB/VB,0}^{P/AP}$ and $v_{CB/VB,1}^{P/AP}$ take into account hybridization with remote bands. Through comparison with the DFT results, we also find that $v_{0,CB}^{P} = v_{0,CB}^{AP} = v_{0,VB}^{P} = v_{0,VB}^{AP} \equiv v_0$, see Fig. 8. Based on DFT computation, we find that all z-dependent functions that appear in Eq. (12) can be described using exponential functions, $A(d) = Ae^{-qz}$, with the parameter values listed in Table III.

C. Interlayer hybridization for conduction band states at the Q points

The conduction band of TMD crystals possesses additional minima at the six inequivalent Q points of the Brillouin zone, located approximately half way between the K and Γ points. For TMD monolayers, the global conduction band minimum is at the K point. However, for TMD homobilayers the larger interlayer hybridization between Q-point states may shift the global conduction band minima to the Q valleys. By contrast to the K and Γ valleys, hybridization of Q-valley states is anisotropic. In this section we introduce a model Hamiltonian describing interlayer hybridization of Q_1-valley states ($\mathbf{Q}_1 \approx \mathbf{K}/2$), and provide the rules for applying the model

TABLE III. Fitting parameters for the interlayer-distance-dependent functions in the Hamiltonian (11) for K-point state hybridization. Each function was fitted as $A(d) = Ae^{-q_A z}$.

	A	q, Å^{-1}
$|t_{CB}|$	3.7 meV	1.5
$|t_{VB}^{P}|$	17.2 meV	1.5
$|t_{VB}^{AP}|$	9.8 meV	1.5
$\tilde{\Delta}_1^{SO}$	-1.14 meV	2.5
$\tilde{\Delta}_{CB,2}^{SO}$	0.1 meV	1.3
v_0	11.0 meV	1.8
$v_{CB,1}^{P}$	1.5 meV	2.7
$v_{VB,1}^{P}$	3.0 meV	2.9
$v_{CB,1}^{AP}$	0.5 meV	2.7
$v_{VB,1}^{AP}$	1.2 meV	3.1
Δ_{CB}^{SO}	41.0 meV	N.A.
Δ_{VB}^{SO}	459.0 meV	N.A.
ε_{CB}	-3.491 eV	N.A.
ε_{VB}	-4.846 eV	N.A.

to the five remaining Q valleys: $-\mathbf{Q}_1$, $\pm\mathbf{Q}_2 = \pm C_3\mathbf{Q}_1$ and $\pm\mathbf{Q}_3 = \pm C_3^2\mathbf{Q}_1$. The effective model reads

$$H_Q^{P/AP} = \varepsilon_Q^{P/AP}\Lambda_0 - \frac{S_Q^{P/AP}}{2}\Lambda_z + T_Q^{P/AP}\Lambda_+ + T_Q^{P/AP*}\Lambda_-.$$
(13)

Here, the matrix elements are expressed as follows:

$$T_Q(\mathbf{r}_0) = |t_0| + |t_1|e^{-i\mathbf{G}_1\cdot\mathbf{r}_0+i\phi_1} + |t_2|e^{i\mathbf{G}_2\cdot\mathbf{r}_0+\phi_2}$$
$$+ |t_3|e^{i\mathbf{G}_3\cdot\mathbf{r}_0+i\phi_3} + |t_3|e^{-i\mathbf{G}_3\cdot\mathbf{r}_0-i\phi_3},$$
(14)

$$\varepsilon_Q(\mathbf{r}_0) = \varepsilon_Q + v_0$$
$$+ \sum_{j=1,2,3}\left[v_j^s\cos(\mathbf{G}_j\cdot\mathbf{r}_0) + v_j^a\sin(\mathbf{G}_j\cdot\mathbf{r}_0)\right],$$
(15)

where we suppressed the P/AP superscript in every term to shorten notations. The rest of the matrix elements are

$$S_Q^{P} = \Delta_a^Q\sum_{j=1,2,3}\sin(\mathbf{G}_j\cdot\mathbf{r}_0),$$
(16)

$$S_Q^{AP} = \Delta_{SO}^Q.$$
(17)

To fit the parameters of the Q-point model Eq. (13), which are gathered in Table IV, we used an additional set of configurations (lateral offsets) as in Ref. [33]. The matrix element $|t_0|$ gives the dominant contribution to resonant hybridization, whereas the $|t_{1,2,3}|$ terms are necessary to describe the stacking-dependent variation of the $T_Q(\mathbf{r}_0)$ matrix element. $\varepsilon_Q(\mathbf{r}_0)$ characterizes hybridization with remote bands having odd terms [$\propto\sin(\mathbf{G}_{1,2,3}\cdot\mathbf{r}_0)$] only for AP bilayers. We also mention that Q-point states are formed by a mixture of the orbital species forming the band edges at the K and Γ valleys [32]. Therefore, the amplitude of the S^P term, describing the potential jump for Q-point states due to interlayer charge transfer, slightly differs from that of the hybridization Hamiltonians for the K and Γ valleys. For the point $-\mathbf{Q}_1$,

related to $\mathbf{Q}_1$ by time reversal symmetry, the hybridization Hamiltonian is the complex conjugate of Eq. (13), whereas the Hamiltonians for the $\pm120°$-rotated Q points ($\mathbf{Q}_2$ and $\mathbf{Q}_3$, respectively) can be obtained by applying the corresponding $\pm120°$ rotation to the reciprocal vectors $\mathbf{G}_{1,2,3}$ in all the matrix elements.

V. BAND-EDGE MAPS FOR TWISTED AP BILAYERS

In this section we combine our results on atomic reconstruction in twisted AP bilayers with the interlayer hybridization models introduced in Sec. IV. This analysis is performed separately for Γ-point states in the valence band, K-point states in the conduction and valence bands, and Q-point conduction states. In particular, we identify where in the moiré supercell the minima for conduction band electrons and valence band holes would appear and produce confinement profiles of quantum dot potentials for each of these specific areas.

A. Modulation of the valence band edge at the Γ point

To apply the model Eq. (7) to a twisted bilayer, we relate the local stacking vector $\mathbf{r}_0$ at position $\mathbf{r}$ to the twist angle $\theta_{P/AP}$ as $\mathbf{r}_0(\mathbf{r}) = \theta_{P/AP}\hat{z}\times\mathbf{r} + \mathbf{u}^t - \mathbf{u}^b$, using also the local interlayer distance shift $z_{AP}(\mathbf{r})$ in the model parameters, and supplementing the diagonal matrix elements with the electron piezoelectric potential energy, $-e\varphi$, equal in the top and bottom layers due to inversion symmetry. As a result, the spatial modulation of the top valence band energy at the Γ point is expressed as

$$E_\Gamma^{AP}(\mathbf{r}) = -e\varphi(\mathbf{r}) + \varepsilon_\Gamma(\mathbf{r}) + \delta\varepsilon_\Gamma(\mathbf{r}) + |T_\Gamma(\mathbf{r}) + \delta T_\Gamma(\mathbf{r})|,$$
(18)

TABLE IV. Fitting parameters for the interlayer-distance-dependent functions in the Hamiltonian Eq. (13) for Q valley. Each function was fitted as Ae^{-qz}, while φ is the phase of corresponding parameter. $\Delta_{SO}^Q \approx 0.214$ eV.

	A, meV	q, Å^{-1}	φ
$|t_0^P|/|t_0^{AP}|$	168/179.5	0.69/0.66	N/A
$|t_1^P|/|t_1^{AP}|$	11.3/6.6	2.2/1.6	$0/-0.46\pi$
$|t_2^P|/|t_2^{AP}|$	11.3/6.6	2.2/1.6	$0/0.46\pi$
$|t_3^P|/|t_3^{AP}|$	2.4/2.4	1.98/1.98	$0/0.3\pi$
$v_1^{(s)P}/v_1^{(s)AP}$	$-3.8/-5$	2.9/2.45	N.A.
$v_2^{(s)P}/v_2^{(s)AP}$	$-3.8/-5$	2.9/2.45	N.A.
$v_3^{(s)P}/v_3^{(s)AP}$	$-1.8/1$	2.3/0.8	N.A.
$v_1^{(a)P}/v_1^{(a)AP}$	N.A./2.5	N.A./3.45	N.A.
$v_2^{(a)P}/v_2^{(a)AP}$	N.A./2.5	N.A./3.45	N.A.
$v_3^{(a)P}/v_3^{(s)AP}$	N.A./2.4	N.A./2.77	N.A.
v_0^P/v_0^{AP}	$-1.4/-3.3$	2.0/2.5	N.A.
$\varepsilon_Q^P/\varepsilon_Q^{AP}$	$-3.52/-3.41 \times 10^3$	N.A.	N.A.
Δ_a^Q	21.5	2.3	N.A.

where the notation

$$\varepsilon_\Gamma(\boldsymbol{r}) = \varepsilon_\Gamma[\boldsymbol{r}_0(\boldsymbol{r}), z_{AP}(\boldsymbol{r})],$$
$$\delta\varepsilon_\Gamma(\boldsymbol{r}) = \delta\varepsilon_\Gamma[\boldsymbol{r}_0(\boldsymbol{r}), z_{AP}(\boldsymbol{r})],$$
$$T_\Gamma(\boldsymbol{r}) = T_\Gamma[\boldsymbol{r}_0(\boldsymbol{r}), z_{AP}(\boldsymbol{r})], \quad (19)$$
$$\delta T_\Gamma(\boldsymbol{r}) = \delta T_\Gamma[\boldsymbol{r}_0(\boldsymbol{r}), z_{AP}(\boldsymbol{r})],$$

is used to describe the dependence of the matrix elements on local stacking and interlayer distance within the moiré supercell. Therefore, to determine the position of the Γ-point valence band edge in twisted bilayers at $0° < \theta_{AP} \leqslant 4°$ we take into account both in-plane reconstruction (inducing the piezopotential) and relaxation of interlayer distances (affecting the hybridization magnitude).

For marginal twist angles $\theta_{AP} \lesssim 1°$, the Γ-point valence band edge is located at three equivalent corners (labeled 2H$_c$ in Fig. 9) of 2H domains around XX′ areas, which is due to the superposition of the largest splitting in 2H domains with the highest piezopotential energy (see inset in Fig. 3). For twist angles $\theta_{AP} > 1°$ the piezopotential amplitude decays, and the valence band edge shifts toward the middle of the 2H domains (Fig. 9). Thus, at marginal twist angles the valence band edge at Γ forms triple quantum dots for holes around the XX′ corner of the 2H domains.

B. Modulation of the valence band edge at the *K* point

Applying the rules described in the previous section to Eq. (11), we obtain the following expression for the *K*-point valence-band-edge variation in the moiré superlattice:

$$E_{\tau\mathbf{K}}^{AP}(\boldsymbol{r}) = \varepsilon_{VB}^{AP}(\boldsymbol{r}) - e\varphi(\boldsymbol{r}) + \sqrt{\left|T_{VB,\tau}^{AP}(\boldsymbol{r})\right|^2 + \frac{(\Delta_{VB}^{SO})^2}{4}}, \quad (20)$$

where we have used the same shorthand notation for local matrix elements as in Eq. (19). Since interlayer coupling of *K*-point states is an order of magnitude weaker than that for Γ-point states, the piezopotential energy plays a key role in establishing the *K*-point valence band edge (Fig. 9). For small twist angles $\theta_{AP} \lesssim 1°$, the *K*-point valence band maximum represents attractive quantum dots for holes located at XX′ stacking regions, with a depth exceeding 100 meV at marginal twist angles (see inset in Fig. 9). By contrast, for larger twist angles $\theta_{AP} \gtrsim 1.5°$ the valence band edge shifts toward the 2H domains, following the minima of the piezopotential (Fig. 3).

For the whole range of twist angles, the energy of the valence band edge at *K* is higher than that at Γ. Therefore, for marginal twist angles ($\theta_{AP} \lesssim 1°$) the band edge will be dominated by hole states localized in QDs at XX′ areas. Due to the large intralayer SO splitting [40] of *K*-point states in WSe$_2$ monolayers (Table III), the quantized states will belong to the higher spin-split band at the $\tau\mathbf{K}$ valley [see Eq. (20)]. To compute the quantum dot states, we solve the Schrödinger equation

$$\left[\frac{\hat{\boldsymbol{p}}^2}{2m_{VB}} - E_{\tau\mathbf{K}}^{AP}(\boldsymbol{r})\right]\Psi = E\Psi, \quad (21)$$
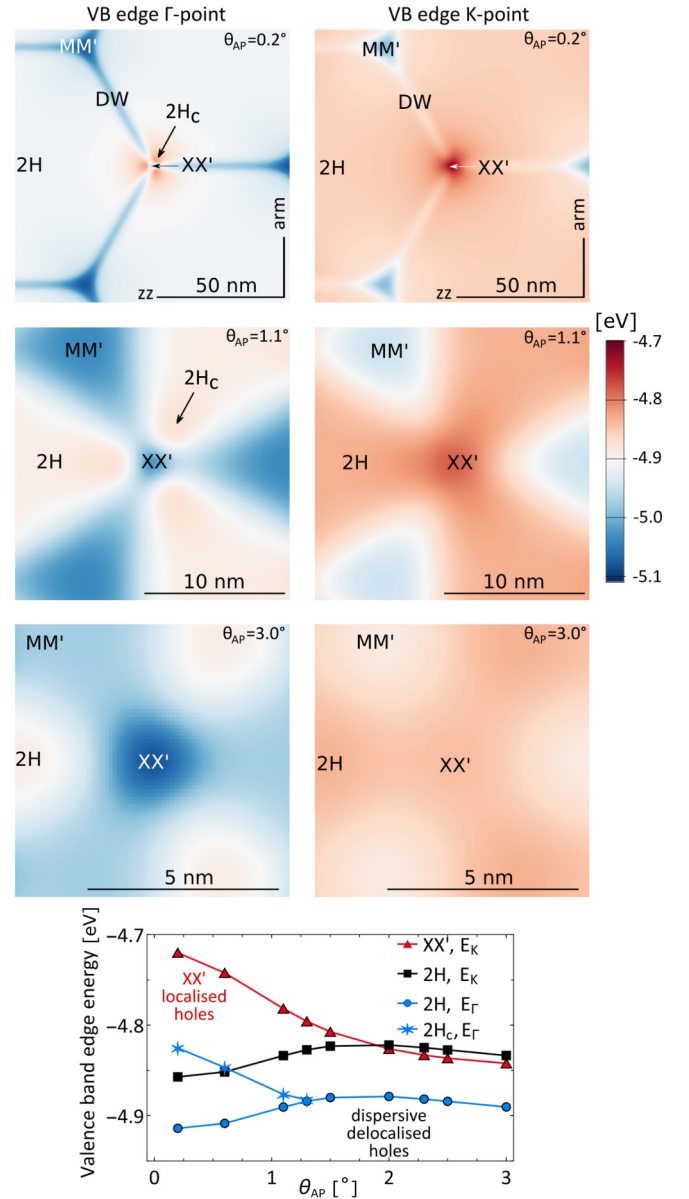
FIG. 9. Maps of the local Γ-point (left column) and *K*-point (right column) valence band (VB) edges across twisted AP-WSe$_2$ bilayers for the labeled twist angles. The vacuum level is set to 0 eV. At marginal twist angles $\theta_{AP} < 1°$ the Γ-point band edge is around the corners of 2H domains labeled by 2H$_c$. This is prescribed by the combined effects of the piezopotential, which is strongest at the XX′ domain corners (see Fig. 3), and the interlayer coupling, which is strongest in 2H domains. For $\theta_{AP} \gtrsim 1°$ the Γ-point band edge is more homogeneously distributed inside 2H domains because of the weaker contribution from the piezopotential. The *K*-point band-edge position is mainly determined by the piezopotential, as the interlayer coupling of the *K*-states is an order of magnitude smaller than that of the Γ states. Zigzag and armchair crystallographic directions in constituent layers marked as zz and arm, respectively, on the top panels, are the same for all maps. The bottom panel shows the twist-angle dependence of the Γ and *K* valence band edges in high symmetry regions of the moiré supercell.
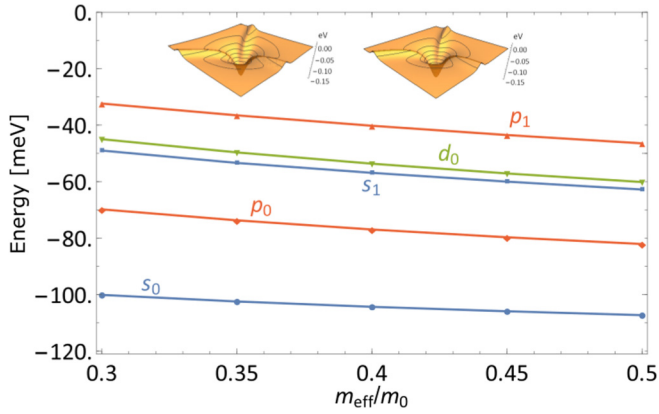
FIG. 10. Lowest energy levels of localized hole states in the quantum dot formed in XX′ areas of marginally twisted AP bilayers. The energies, counted from continuum in 2H domains, results from solution of Eq. (21) and are labeled by orbital momentum s, p, d . . . for $|l| = 0, 1, 2, \ldots$, with subscript indicating radial quantum number $n_r = 0, 1, 2, \ldots$. p and d states are double degenerate in the sign of orbital momentum. On insets we show that discrepancy between calculated (left) and fitted (right) quantum dot potentials does not exceed 5 meV in the whole vicinity of XX′ area.

where $m_{\text{VB}} > 0$ is the monolayer valence band effective mass at the K point, and $\hat{\boldsymbol{p}} = -i\hbar(\partial_x, \partial_y)$. We approximate the hole potential energy around the XX′ region as

$$
\begin{aligned}
E_{\tau\mathbf{K}}^{\text{AP}}(\boldsymbol{r}) &\approx -V(r) - V_3(r, \phi), \\
V(r) &= \frac{V_0}{1 + \frac{r^2}{\rho_0^2}}, \\
V_3(r, \phi) &= \frac{V_1 - V_2\sqrt{\beta^2 + \frac{r^2}{l^3}\left[\rho_1 - \frac{r\cos 3\phi}{\sqrt{1 + \frac{r^2}{\rho_1^2}}}\right]}}{\left(1 + \frac{r^2}{l^3}\left[\rho_1 - \frac{r\cos 3\phi}{\sqrt{1 + \frac{r^2}{\rho_1^2}}}\right]\right)^{3/2}},
\end{aligned} \tag{22}
$$

where V is the axial-symmetric part of the potential, and V_3 describes trigonal warping [41], $r = \sqrt{x^2 + y^2}$ is the in-plane distance measured from the middle of the XX′ area, and ϕ is the polar angle. From fitting, we find that $V_0 = -155$ meV, $\rho_0 = 4.3$ nm, $V_1 \approx 21$ meV, $V_2 = -21$ meV, $\beta = 0.015$, $\rho_1 = 0.79$ nm, and $l = 4$ nm. Although the particular parameter values for V and V_3 were fitted for $\theta_{\text{AP}} = 0.2°$, we believe that the final results can be applied to twist angles $0° < \theta_{\text{AP}} \leqslant 0.3°$, for which the potential amplitudes are essentially unchanged. In Eq. (22) we measure the potential energy relative to its value inside the 2H domains, and demonstrate the quality of our fitting in the insets of Fig. 10.

We solve Eq. (22) using perturbation theory over V_3, which is much smaller than the axially symmetric potential V. In the zeroth-order approximation, the wave functions are eigenfunctions of angular momentum $l = 0, \pm 1, \pm 2, \ldots$, i.e., $\psi = \chi_l(r)e^{il\phi}$. Then, we perturbatively take into account the weak coupling between the lowest energy states with $|l| = 1, 2$, given by the trigonal warping term V_3. In Fig. 10 we plot the energies of the lowest levels in a single quantum dot, labeling them according to the largest component of the orbital angular

momenta. We note that, together with the double degeneracy of states with opposite orbital angular momentum sign (for $l \neq 0$), each QD level has an additional twofold Kramers degeneracy with the state at the opposite valley.

Since the decay lengths (≈ 2 nm) of the lowest-energy states s_0 and p_0 are much smaller than the moiré superlattice period for the marginal twist angles, there is only a weak overlap between states in neighboring quantum dots (XX′ regions), giving a realization of the Hubbard model when interactions are considered [42]. Therefore, we anticipate a Mott insulating state in marginally twisted p-doped AP-WSe$_2$ bilayers, similar to those observed at larger twist angles in P-WSe$_2$ bilayers [5], and in twisted bilayer graphene [2,3,7,43].

C. Modulation of the conduction-band edge at the K point

Modulation of the K-point conduction-band edge is determined by the same Eq. (20), replacing VB → CB in the matrix elements of Eq. (11). Similarly to the valence-band-edge case, the conduction-band-edge variation across the moiré supercell is dominated by the piezopotential energy of electrons (Fig. 11).

Unlike holes, for K-point electrons the piezopotential energy minimum (as well as the band edge) appears inside MM′ areas for the range of twist angles $0° \leqslant \theta_{\text{AP}} \lesssim 3°$. Therefore, we expect the formation of localized electron states in MM′ regions, which are split from the continuum of conduction band states, with the energy distance between levels tuned by the twist angle magnitude (see bottom panel in Fig. 7).

D. Modulation of the conduction band edge at the Q_1 point

The conduction-band edge at the Q_1 point is described by the lower eigenvalue of the Hamiltonian Eq. (13), supplemented by the piezopotential, which is the same in both layers:

$$
E_Q^{\text{AP}}(\boldsymbol{r}) = -e\varphi(\boldsymbol{r}) + \varepsilon_Q^{\text{AP}}(\boldsymbol{r}) - \sqrt{\left|T_Q^{\text{AP}}(\boldsymbol{r})\right|^2 + \frac{\left(\Delta_{\text{SO}}^Q\right)^2}{4}}. \tag{23}
$$

At marginal twist angles, $\theta_{\text{AP}} < 1°$, the Q-point band edge is also dominated by the piezopotential modulation, which produces quantum dot potentials for electrons in MM′ corners of the hexagonal domain wall network (Fig. 11). Therefore, for Q valleys we also can expect the formation of localized electron states with a discrete spectrum in MM′ regions, similar to the K valley. However, unlike the K-valley levels, Q-valley levels with angular momenta of opposite sign are not degenerate due to the anisotropy of the effective-mass tensor [32]. For larger twist angles $\theta_{\text{AP}} \gtrsim 2.5°$ the band edge gradually shifts toward 2H regions. Here, we also mention that despite the explicit lack of C_3 symmetry in the model Eq. (13), this symmetry approximately persists for the band edge, mainly due to the zigzag orientation of the domain walls resulting from lattice reconstruction. Therefore, the conduction-band-edge modulation for the $\pm 120°$-rotated Q_2 and Q_3 valleys are the same as in Fig. 11.

VI. BAND-EDGE VARIATION IN TWISTED P BILAYERS

In this section we combine the details of atomic reconstruction in twisted P bilayers obtained in Sec. II, with the
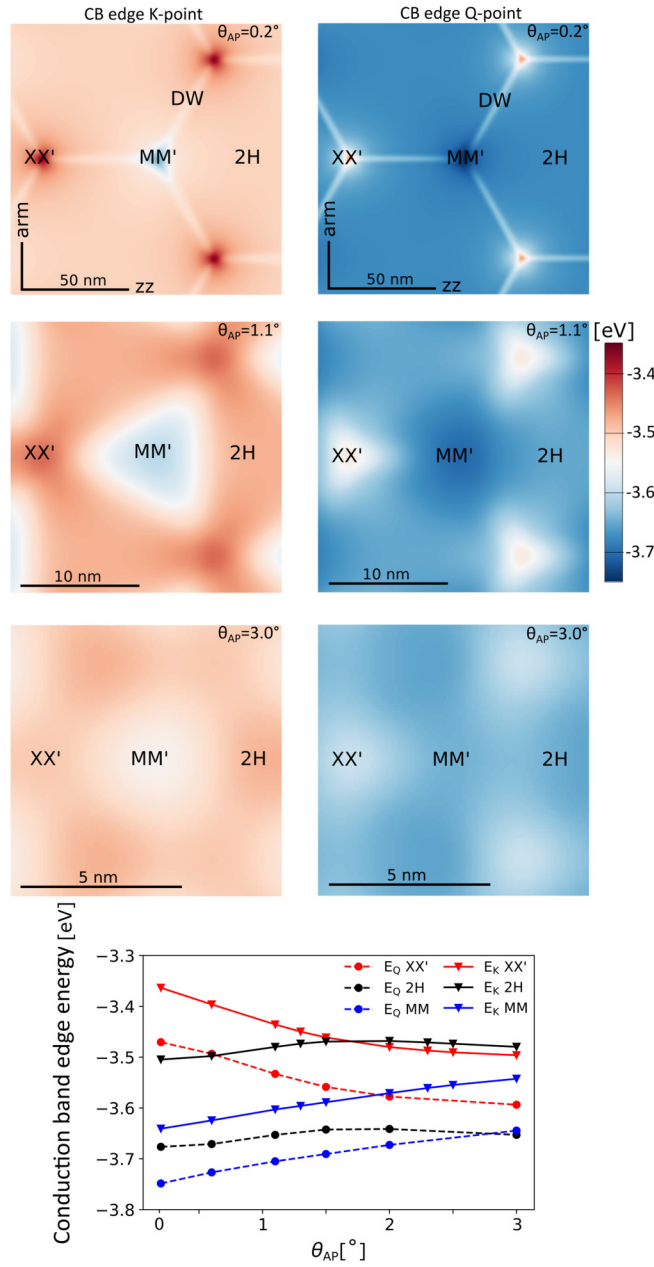
FIG. 11. Piezopotential-induced modulation of the K-point (left) and Q-point (right) conduction band edges, which creates quantum-dot-like potentials for electrons in MM$'$ areas of the supercell of twisted AP-WSe$_2$ bilayers. The zigzag (zz) and armchair (arm) crystallographic directions shown in the top panels are the same for all maps. The vacuum level is set to 0 eV. The bottom panel shows the twist-angle dependencies of the K-point conduction band edge in the labeled areas of the supercell.

hybridization analysis of Sec. IV. Here, we separate the analysis of valence band modulation at Γ and K from that of the K- and Q-point conduction band edges.

A. Valence-band-edge modulation at the Γ and K points

Unlike AP bilayers, in P bilayers the piezocharges induced by lattice reconstruction have opposite signs in the opposite layers, leading to a vanishing total piezopotential over the

bilayer, but a nonzero layer-asymmetric contribution $\varphi_t(\boldsymbol{r}) = -\varphi_b(\boldsymbol{r}) \equiv \Delta\varphi/2$. As a result, in the hybridization models Eqs. (7) and (11) the piezopotential contributes to the splitting of the coupled states rather than to an overall energy shift. Diagonalizing the Hamiltonian Eqs. (7) and (11) with the substitution of local matrix elements discussed in Sec. IV, we obtain expressions for the local valence-band-edge energies at the Γ and K points across the moiré superlattice:

$$E_\Gamma^P(\boldsymbol{r}) = \varepsilon_\Gamma(\boldsymbol{r}) + \delta\varepsilon_\Gamma(\boldsymbol{r}) + \sqrt{T_\Gamma^2(\boldsymbol{r}) + \frac{[\Delta^P(\boldsymbol{r}) + e\Delta\varphi(\boldsymbol{r})]^2}{4}},$$
(24)

$$E_{VB,\tau K}^P(\boldsymbol{r}) = \varepsilon_{VB}^P(\boldsymbol{r}) + \sqrt{\left|T_{VB,\tau}^P(\boldsymbol{r})\right|^2 + \frac{[\Delta^P(\boldsymbol{r}) + e\Delta\varphi(\boldsymbol{r})]^2}{4}},$$
(25)

where local matrix elements are defined as in Eqs. (18) and (20). For the full range of twist angles, the valence band edge at K lies more than 50 meV higher than that at the Γ point across a moiré supercell; see Fig. 12(a). This behavior of the valence band maximum for WSe$_2$ bilayers is peculiar, since for other semiconducting TMDs homobilayers (WS$_2$, MoS$_2$, and MoSe$_2$) interlayer hybridization of the monolayer Γ-point states, formed by p_z and d_{z^2} orbitals of chalcogens and metals, respectively, pushes the Γ-point valence band edge more than 100 meV higher in energy than the highest valence band state at the K point [44–46]. The real-space location of the K-point band edge in the moiré supercell depends on the twist angle because of different spatial variations of $T_{VB,\tau}^P$, Δ^P, and $e\Delta\varphi$ in Eq. (26) across the moiré supercell. The latter two possess opposite signs, leading to a decrease of the band-edge energy Eq. (25) in areas where both contributions exist. For marginal twist angles $\theta_P \lesssim 1°$, the competition between the piezo- an ferropotential leads to a reduction of the band-edge energy along domain walls, but pushing it up in MX$'$/XM$'$ domains where Δ^P is maximal and $e\Delta\varphi$ and $T_{VB,\tau}^P$ vanish. At the same time, the valence band energy inside MX$'$/XM$'$ domains appears only ≈ 5 meV higher than that in XX$'$ areas given merely by $T_{VB,\tau}^P$. This makes the valence band-edge landscape rather shallow in marginally twisted P-WSe$_2$ bilayers.

With the reduced domain sizes at larger twist angles $\theta_P \gtrsim 1°$, the piezopotential extends inside XM$'$ and MX$'$ domains, leading to a cancellation of the potential jump Δ^P that lowers the VB edge energy inside them, shifting it toward XX$'$ areas.

B. Modulation of the conduction band edge and vertical band gap at K

Similarly to the valence band, for the conduction band at K we can substitute the local lateral offset and interlayer distance into the Hamiltonian Eq. (11). Then, taking the piezopotential into account leads to the following expression for the K-point conduction band edge:

$$E_{CB,\tau K}^P(\boldsymbol{r}) = \varepsilon_{CB}^P(\boldsymbol{r}) - \sqrt{\left|T_{CB,\tau}^P(\boldsymbol{r})\right|^2 + \frac{[\Delta^P(\boldsymbol{r}) + e\Delta\varphi(\boldsymbol{r})]^2}{4}}.$$
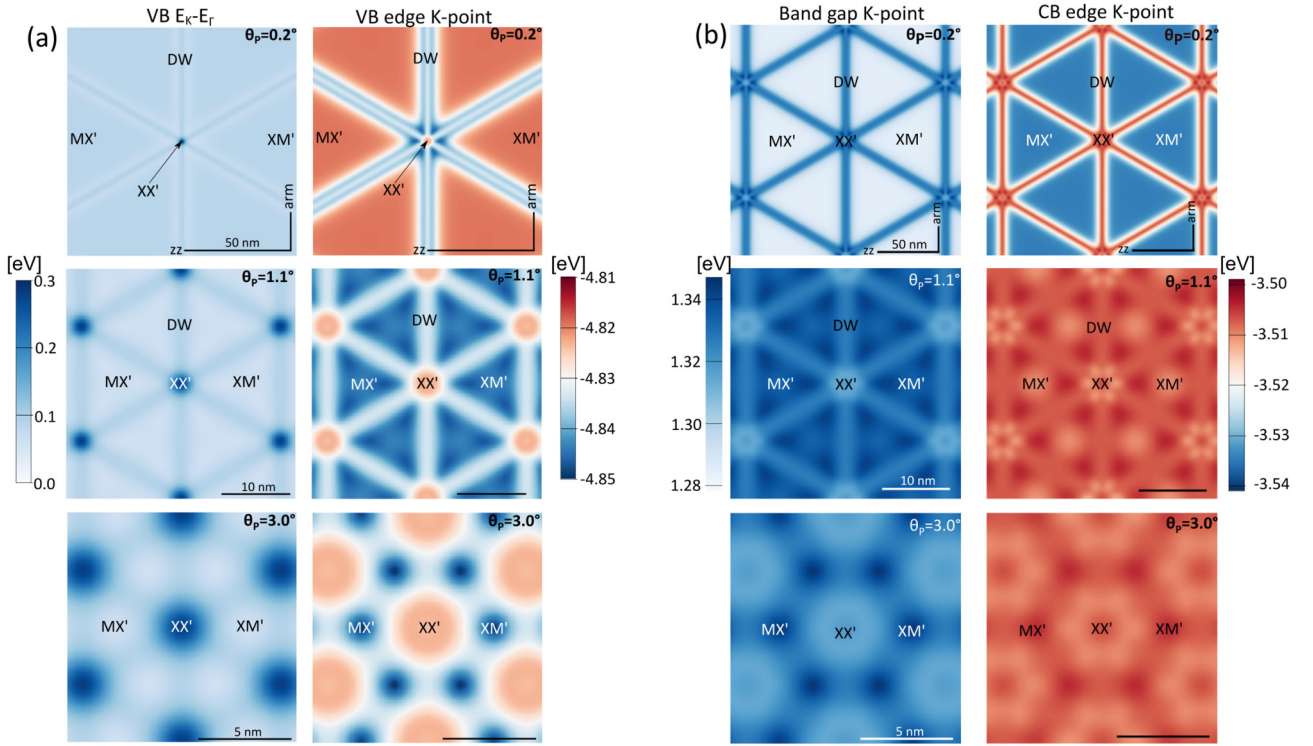(26)

FIG. 12. (a) Maps of the valence-band-edge difference $E_K^P - E_\Gamma^P$ (left column) and K-point valence band edge (right column), for twisted P-WSe$_2$ bilayers at the labeled twist angles. (b) Modulation of the direct band gap (left) and of the conduction band edge (right) at the K point, for twisted P-WSe$_2$ bilayers with the labeled twist angles. At $\theta_P \lesssim 1.0°$, the conduction band edge and the smallest band gap lie inside MX′ and XM′ domains, while at larger angles $\theta_P \gtrsim 1.0°$ the former possesses weak minima around XX′ areas in the shape of benzene molecules. All maps were calculated with the vacuum level set to 0 eV, and are displayed for the same orientations of zigzag (zz) and armchair (arm) crystallographic directions, shown in the upper panels.

For marginal twist angles $\theta_P \lesssim 1°$, the K-point conduction band edge lies in MX′ and XM′ domains [Fig. 12(b)], in a similar manner to the valence band edge [Fig. 12(a)], placing the direct band gap at the K point inside XM′/MX′ regions.

For larger twist angles, the conduction band edge shifts toward the corners of XM′ and MX′ domains, forming a weak localizing ($\lesssim 10$ meV) potential around XX′ areas with the shape of benzene molecules.

Thus, at marginal twist angles the optoelectronic properties of P-WSe$_2$ bilayers will be similar to the aligned WSe$_2$ bilayers corresponding to 3R-polytypes of bulk TMD crystals, while at larger angles the band-edge modulation across the supercell is vanishingly small.

C. Optical selection rules for ground-state bright τK-valley interlayer excitons in XM′ and MX′ domains

Here, we establish optical selection rules for ground states of the bright (K-K) interlayer excitons formed by the electrons and holes inside XM′ domains. The corresponding selection rules for MX′ domains can then be obtained by mirror reflection with respect to the xy plane. Using the hybridization model Eq. (12) for XM′-stacking [$\boldsymbol{r}_0 = (0, a/\sqrt{3})$], we obtain a vanishing resonant interlayer hybridization ($T_{CB,VB} = 0$), giving electron/hole states that are layer-polarized in the conduction/valence bands of the top/bottom layers, respectively, due to the ferroelectric potential. The momentum matrix element, which characterizes coupling of the K-K

interlayer excitons with light, transforms under C_3 rotations as [47]

$$\langle C_3 \psi_{VB,\tau K} | C_3 (p_x \pm i p_y) C_3^{-1} | C_3 \psi_{CB,\tau K} \rangle$$
$$= e^{i\frac{2\pi}{3}(\tau \mp 1)} \langle \psi_{VB,\tau K} | p_x \pm i p_y | \psi_{CB,\tau K} \rangle. \quad (27)$$

Here, $\psi_{VB,\tau K} = e^{i\tau K r} u_{VB,\tau K}(\boldsymbol{r})$ is the Bloch function of the bottom-layer valence state ($u_{VB,\tau K}(\boldsymbol{r})$ transforms as $(x - i\tau y)^2$ [32]), and $\psi_{CB,\tau K} = e^{i\tau K(r-r_0)} u_{CB,\tau K}(\boldsymbol{r} - \boldsymbol{r}_0)$ is the top-layer conduction-band Bloch function, shifted by the offset $\boldsymbol{r}_0 = (0, a/\sqrt{3})$ ($u_{CB,\tau K}(\boldsymbol{r} - \boldsymbol{r}_0)$ transforms as z^2). The matrix element of dipole transitions couples $p_x \pm i p_y$ with $A_x \mp iA_y$, where A_x and A_y are the components of the electromagnetic vector potential. Based on Eq. (27), this leads to circularly polarized luminescence with counter-clockwise polarization (σ_-) for +K-valley excitons, and clockwise polarization (σ_+) for −K-valley excitons.

D. Modulation of the conduction band edge at Q_1

The conduction band edge at the Q_1 point is described by the lower eigenvalue of the Hamiltonian Eq. (13), substituting the local lateral offset $\mathbf{r}_0(\mathbf{r})$ and supplemented with the piezopotential, which has opposite sign in the top and bottom layers:

$$E_Q^P(\boldsymbol{r}) = \varepsilon_Q^P(\boldsymbol{r}) - \sqrt{\left|T_Q^P(\boldsymbol{r})\right|^2 + \frac{\left[S_Q^P(\boldsymbol{r}) + e\Delta\varphi(\boldsymbol{r})\right]^2}{4}}. \quad (28)$$
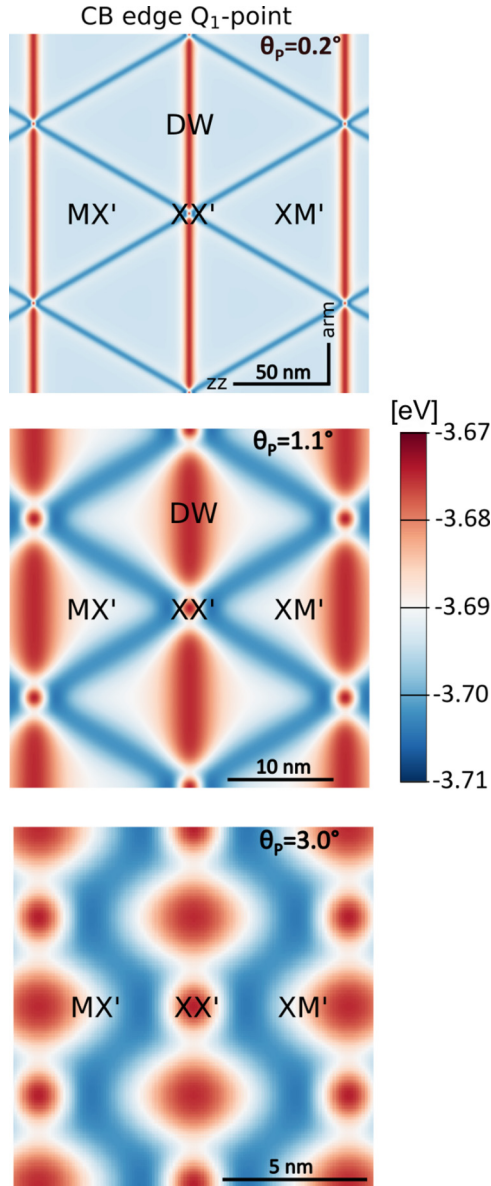
FIG. 13. Modulation of the conduction band edge at the $\pm \mathbf{Q}_1$ points, for twisted P-WSe$_2$ bilayers with the labeled twist angles. At $\theta_P \lesssim 2.0°$, the conduction band edge consists of one-dimensional channels of ≈ 10 meV depth along two of three DWs orientations, transforming to zigzagging landscape for higher twist angles. Conduction-band-edge variations for $\pm \mathbf{Q}_{2,3}$ can be obtained applying $\pm 120°$-rotation, respectively.

The conduction-band-edge maps for Q_1 states, shown in Fig. 13, are not symmetric under 120° rotations, because of the anisotropy of the resonant interlayer coupling term T_Q^P resulting from low-symmetry of the Q states. At small twist angles $\theta_P \lesssim 2.0°$, the anisotropic coupling, along with the piezopotential that is substantial in the vicinity of DWs, place the band edge in one-dimensional channels with ≈ 10 meV depth, forming along two of three domain wall orientations. Although for larger twist angles the domain wall structure disappears, the conduction band edge still occurs along channels with a zigzag shape. Band-edge landscapes for the $\mathbf{Q}_{2,3}$ points are obtained by $\pm 120°$-rotation of the maps in Fig. 13,

respectively, while those for $-\mathbf{Q}_{1,2,3}$ states are the same as for $\mathbf{Q}_{1,2,3}$.

VII. MOIRÉ SUPERLATTICE MINIBANDS FOR WAVE VECTORS NEAR THE Γ, K, AND Q VALLEYS

In-plane lattice reconstruction is weak for misalignment angles larger than $\theta_{P/AP}^*$, such that $\mathbf{u}^t$ and $\mathbf{u}^b$ can be neglected and the local stacking vector approximated by $\mathbf{r}_0(\mathbf{r}) \approx \theta_{P/AP} \hat{\mathbf{z}} \times \mathbf{r}$. This spatial modulation of the interlayer registry results in a moiré superlattice with periodicity a_M related to the lattice constant a as $a_M = a\,\theta_{P/AP}^{-1}$. In reciprocal space, the superlattice is described by a set of moiré Bragg vectors $\mathbf{g}_j \equiv \mathbf{G}_j^b - \mathbf{G}_j^t$, where $\mathbf{G}_j^b$ and $\mathbf{G}_j^t$ are reciprocal lattice vectors of the individual rotated layers, given by

$$\mathbf{G}_j^b = \mathcal{R}_{-\theta_{P/AP}/2}\mathbf{G}_j, \qquad \mathbf{G}_j^t = \mathcal{R}_{\theta_{P/AP}/2}\mathbf{G}_j, \qquad (29)$$

where $\mathcal{R}_\phi$ rotates by an angle ϕ about axis $\hat{\mathbf{z}}$, and $\mathbf{G}_j$ are the reciprocal lattice vectors before rotation.

Model for the mSL near the Γ point band edge. The local Hamiltonian for Γ-point valence electrons at position $\mathbf{r}$ is obtained from the registry-dependent model Eq. (8) with local $\mathbf{r}_0 \to \mathbf{r}_0(\mathbf{r})$, supplemented by the piezoelectric potentials $\varphi_b = \varphi_t \equiv \varphi$ for AP and $\varphi_b = -\varphi_t \equiv -\varphi$ for P bilayers. This gives the Hamiltonian [see Eq. (8)]

$$\mathcal{H}_{VB,\Gamma}^{P/AP}(\mathbf{r}) = \frac{\hbar^2(-i\nabla)^2}{2m_\Gamma}\Lambda_0 + H_\Gamma^{P/AP}[\mathbf{r}_0(\mathbf{r}), z(\mathbf{r})]$$
$$- \frac{e\varphi(\mathbf{r})}{2}[(1 \mp 1)\Lambda_0 + (1 \pm 1)\Lambda_z], \quad (30)$$

acting on plane-wave states of the form $\psi(\mathbf{r}) = (e^{i\mathbf{k}\cdot\mathbf{r}}, e^{i\mathbf{k}\cdot\mathbf{r}})^T$. Note that we have considered also the spatial dependence of the coefficients Eq. (9) coming from the interlayer distance modulation described by Eq. (2), in which we have used the first 10–20 stars of moiré harmonics characterized by Fourier coefficients presented in Appendix F. Similarly, we have written the piezopotential in terms of the Fourier expansion (see Appendix F)

$$\varphi(\mathbf{r}) = \sum_{j=1} \varphi_j \cos(\mathbf{g}_j \cdot \mathbf{r}). \qquad (31)$$

The superlattice Hamiltonian for Γ-point electrons takes on the form

$$\mathcal{H}_{VB,\Gamma}^{P/AP}(\mathbf{r}) = \left[\frac{\hbar^2 k^2}{2m_\Gamma} + \varepsilon_\Gamma^{P/AP}(\mathbf{r})\right]\Lambda_0 - \frac{S_\Gamma^{P/AP}(\mathbf{r})}{2}\Lambda_z$$
$$- \frac{e\varphi(\mathbf{r})}{2}[(1 \mp 1)\Lambda_0 + (1 \pm 1)\Lambda_z]$$
$$+ \operatorname{Re} T_\Gamma^{P/AP}(\mathbf{r})\Lambda_x - \operatorname{Im} T_\Gamma^{P/AP}(\mathbf{r})\Lambda_y, \quad (32)$$

where the spatial dependence comes through $\mathbf{r}_0(\mathbf{r})$ and $z(\mathbf{r})$, as in Eq. (19).

Model for the mSL near the K-point band edge. To describe K-point conduction and valence electrons one must consider that the top- and bottom layer K valleys are also
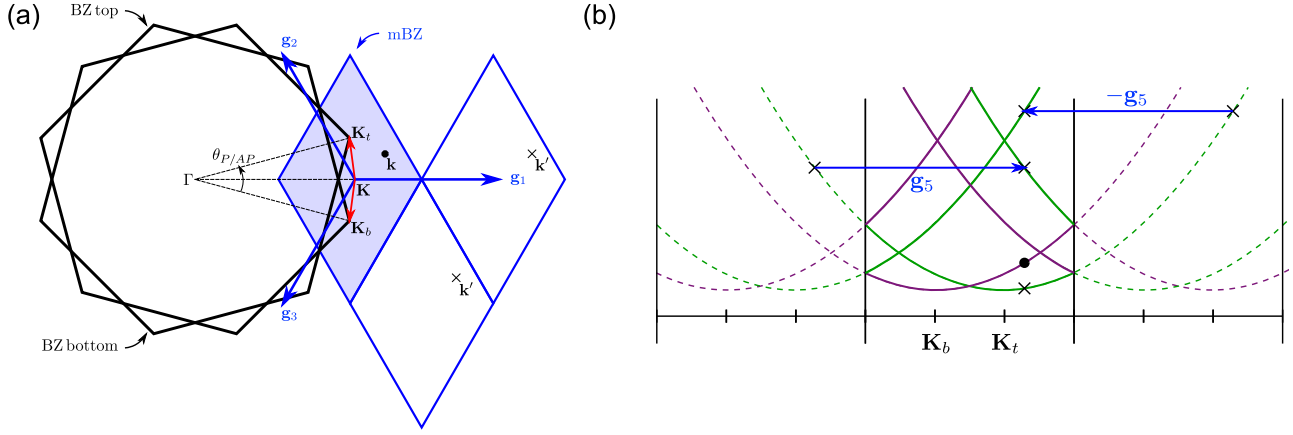
FIG. 14. Zone folding scheme for the moiré miniband calculations. (a) The top- and bottom-layer Brillouin zones appear rotated by angles $\pm\theta_{P/AP}/2$, such that their corners $\mathbf{K}_t$ and $\mathbf{K}_b$ are shifted from $\mathbf{K}$ by $\pm\Delta\mathbf{K}/2$ (red arrows), respectively. The wave vector $\mathbf{k}$ shown (●) is equivalent to the wave vectors $\mathbf{k}' = \mathbf{k} - \mathbf{g}_2$ and $\mathbf{k}' = \mathbf{k} + \mathbf{g}_1$ (×), in the sense that they are tunnel-coupled by the first term of Eq. (38). This defines the first mBZ, shaded blue in the figure. (b) Top- and bottom-layer electron dispersions along the $\overline{\mathbf{K}_b\,\mathbf{K}_t}$ axis in an extended mBZ scheme. Superlattice momentum states outside the first mBZ appear as "folded" minibands. The bottom-layer state marked with a ● symbol tunnel-couples to the top-layer states marked as ×, including those separated by second-star moiré vectors $\pm\mathbf{g}_5 = \pm(\mathbf{g}_2 - \mathbf{g}_3)$, by the second term in Eq. (38).

rotated as $\mathbf{K}_{t/b} = \mathcal{R}_{\pm\theta_{P/AP}/2}\mathbf{K}$, with $\mathbf{K}$ the valley vector before rotation, introducing a valley mismatch $\Delta\mathbf{K} = \mathbf{K}_t - \mathbf{K}_b$; see Fig. 14(a). This is included in the local Hamiltonian for $\tau\mathbf{K}$ valley electrons by applying a unitary transformation $\mathcal{U}_{\theta_{P/AP}}^\tau(\Delta\mathbf{K})$ that adjusts the wave vectors upon rotation of the reciprocal lattices. The superlattice Hamiltonian at valley $\tau\mathbf{K}$ for band $\alpha = $ CB, VB, for conduction- and valence band, respectively, is given by

$$\mathcal{H}_{\alpha,\tau\mathbf{K}}^{P/AP}(\mathbf{r}) = \mathcal{U}_{\theta_{P/AP}}^\tau(\Delta\mathbf{K})\left[H_{\alpha,\tau\mathbf{K}}^{P/AP}(\mathbf{r}) + \frac{\hbar^2}{2m_\alpha}\frac{(-i\boldsymbol{\nabla} - \tau\mathbf{K}_t)^2 + (-i\boldsymbol{\nabla} - \tau\mathbf{K}_b)^2}{2}\Lambda_0 + \frac{\hbar^2}{2m_\alpha}\frac{\mathbf{K}_t + \mathbf{K}_b + 2i\tau\boldsymbol{\nabla}}{2}\cdot\Delta\mathbf{K}\Lambda_z\right.$$
$$\left. - \frac{e\varphi(\mathbf{r})}{2}[(1\mp 1)\Lambda_0 + (1\pm 1)\Lambda_z]\right]\mathcal{U}_{\theta_{P/AP}}^{\tau-1}(\Delta\mathbf{K}),$$
$$\mathcal{U}_{\theta_{P/AP}}^\tau(\Delta\mathbf{K}) = \begin{pmatrix} e^{i\tau\Delta\mathbf{K}\cdot\mathbf{r}/2} & 0 \\ 0 & e^{-i\tau\Delta\mathbf{K}\cdot\mathbf{r}/2} \end{pmatrix}, \tag{33}$$

and takes the final form

$$\mathcal{H}_{\alpha,\tau\mathbf{K}}^{P/AP}(\mathbf{r}) = \frac{\hbar^2}{2m_\alpha}\left(\mathbf{k}\Lambda_0 - \frac{\Delta\mathbf{K}}{2}\Lambda_z\right)^2 + \varepsilon_\alpha^{P/AP}(\mathbf{r})\Lambda_0 - \frac{S_\alpha^{P/AP}(\mathbf{r})}{2}\Lambda_z - \frac{e\varphi(\mathbf{r})}{2}[(1\mp 1)\Lambda_0 + (1\pm 1)\Lambda_z]$$
$$+ \mathrm{Re}\big[e^{i\tau\Delta\mathbf{K}\cdot\mathbf{r}}T_{\alpha,\tau}^{P/AP}(\mathbf{r})\big]\Lambda_x - \mathrm{Im}\big[e^{i\tau\Delta\mathbf{K}\cdot\mathbf{r}}T_{\alpha,\tau}^{P/AP}(\mathbf{r})\big]\Lambda_y. \tag{34}$$

Model for the mSL near the Q_1-point band edge. The Q_1 valley case is analogous to that of the K valley. The top- and bottom-layer Q_1 valleys are rotated as $\mathbf{Q}_{1,t/b} = \mathcal{R}_{\pm\theta_{P/AP}/2}\mathbf{Q}_1$, with $\mathbf{Q}_1$ the valley vector before rotation. This results in a Q_1-valley mismatch $\Delta\mathbf{Q} = \mathbf{Q}_{1,t} - \mathbf{Q}_{1,b}$, as well as a relative rotation of the wave vectors, implemented by a unitary transformation $\mathcal{U}_{\theta_{P/AP}}(\Delta\mathbf{Q})$ that acts on the plane-wave states as

$$\mathcal{U}_{\theta_{P/AP}}(\Delta\mathbf{Q})\begin{pmatrix} e^{i(\mathbf{Q}_1 + \mathbf{k})\cdot\mathbf{r}} \\ e^{i(\mathbf{Q}_1 + \mathbf{k})\cdot\mathbf{r}} \end{pmatrix} = \begin{pmatrix} e^{i(\mathbf{Q}_1 + \frac{\Delta\mathbf{Q}}{2} + \mathcal{R}_{\theta_{P/AP}/2}\mathbf{k})\cdot\mathbf{r}} \\ e^{i(\mathbf{Q}_1 - \frac{\Delta\mathbf{Q}}{2} + \mathcal{R}_{-\theta_{P/AP}/2}\mathbf{k})\cdot\mathbf{r}} \end{pmatrix}. \tag{35}$$

Note that, unlike at the K valleys, the monolayer conduction band dispersions at Q_1 are anisotropic, with distinct masses m_x and m_y along and perpendicular to the $\overline{\Gamma K}$ line. Therefore, the wave vectors $\mathcal{R}_{\pm\theta_{P/AP}/2}\mathbf{k}$ in Eq. (35) will rotate the monolayer dispersions. The resulting Q_1-point Hamiltonian is

$$\mathcal{H}_Q^{P/AP}(\mathbf{r}) = \frac{\hbar^2}{2m_x}\left(k_x\Lambda_0 - \frac{\theta_{P/AP}}{2}k_y\Lambda_z\right)^2 + \frac{\hbar^2}{2m_y}\left(k_y\Lambda_0 + \left[\frac{\theta_{P/AP}}{2}k_x - \frac{|\Delta\mathbf{Q}|}{2}\right]\Lambda_z\right)^2 + \varepsilon_Q^{P/AP}(\mathbf{r})\Lambda_0 - \frac{S_Q^{P/AP}(\mathbf{r})}{2}\Lambda_z$$
$$- \frac{e\varphi(\mathbf{r})}{2}[(1\mp 1)\Lambda_0 + (1\pm 1)\Lambda_z] + \mathrm{Re}\big[e^{i\Delta\mathbf{Q}\cdot\mathbf{r}}T_Q^{P/AP}(\mathbf{r})\big]\Lambda_x - \mathrm{Im}\big[e^{i\Delta\mathbf{Q}\cdot\mathbf{r}}T_Q^{P/AP}(\mathbf{r})\big]\Lambda_y. \tag{36}$$

To show the spatial dependence of the matrix elements, we take the *K*-point Hamiltonian interlayer hybridization term as an example. From Eq. (12) and Eqs. (C21c) and (C23c) in Appendix C we have

$$
e^{i\tau\Delta\mathbf{K}\cdot\mathbf{r}}T_{\alpha,\tau}^{\mathrm{P/AP}} = e^{i\tau\Delta\mathbf{K}\cdot\mathbf{r}}t_{\alpha}^{\mathrm{P/AP}}e^{-q_{t_\alpha}^{\mathrm{P/AP}}z(\mathbf{r})}\sum_{\mu=0}^{2}e^{-i\tau C_3^{\mu}\Delta\mathbf{K}\cdot\mathbf{r}}e^{i\frac{4}{3}\tau\mu\chi_{\mathrm{P/AP}}(\lambda_\alpha+1)}
$$

$$
\approx e^{i\tau\Delta\mathbf{K}\cdot\mathbf{r}}\tilde{t}_{\alpha}^{\mathrm{P/AP}}\left[1 - q_{t_\alpha}^{\mathrm{P/AP}}\sum_{j=1}^{\mathcal{N}}z_j^s\cos(\mathbf{g}_j\cdot\mathbf{r}) - q_{t_\alpha}^{\mathrm{P/AP}}\sum_{j=1}^{\mathcal{N}}z_j^a\sin(\mathbf{g}_j\cdot\mathbf{r})\right]\sum_{\mu=0}^{2}e^{-i\tau C_3^{\mu}\Delta\mathbf{K}\cdot\mathbf{r}}e^{i\frac{4}{3}\tau\mu\chi_{\mathrm{P/AP}}(\lambda_\alpha+1)}
\tag{37}
$$

$$
\approx \tilde{t}_{\alpha}^{\mathrm{P/AP}}\big[1 + e^{i\tau\mathbf{g}_2\cdot\mathbf{r}}e^{i\frac{4}{3}\tau\chi_{\mathrm{P/AP}}(\lambda_\alpha+1)} + e^{-i\tau\mathbf{g}_1\cdot\mathbf{r}}e^{i\frac{8}{3}\tau\chi_{\mathrm{P/AP}}(\lambda_\alpha+1)}\big]
$$

$$
- \sum_{\nu=-1,+1}\sum_{j=1}^{\mathcal{N}}q_{t_\alpha}^{\mathrm{P/AP}}\frac{\tilde{t}_{\alpha}^{\mathrm{P/AP}}}{2}\big(z_j^s - i\nu z_j^a\big)\big[e^{i\nu\mathbf{g}_j\cdot\mathbf{r}} + e^{i(\tau\mathbf{g}_2+\nu\mathbf{g}_j)\cdot\mathbf{r}}e^{i\frac{4}{3}\tau\chi_{\mathrm{P/AP}}(\lambda_\alpha+1)} + e^{i(-\tau\mathbf{g}_1+\nu\mathbf{g}_j)\cdot\mathbf{r}}e^{i\frac{8}{3}\tau\chi_{\mathrm{P/AP}}(\lambda_\alpha+1)}\big],
$$

where we have introduced $\tilde{t}_{\alpha}^{\mathrm{P/AP}} \equiv \exp\left(-q_{t_\alpha}^{\mathrm{P/AP}}z_0\right)t_{\alpha}^{\mathrm{P/AP}}$, approximated the exponential dependence on interlayer distance modulation by its first-order expansion in the coefficients z_j for $j \geqslant 1$, and used the fact that $(1 - C_3)\Delta\mathbf{K} = \mathbf{g}_2$ and $(1 - C_3^2)\Delta\mathbf{K} = -\mathbf{g}_1$, with $C_3 = \mathcal{R}_{2\pi/3}$. The interlayer tunneling matrix element is then

$$
\int d^2r\,\psi_{\mathbf{k}'}^{\dagger}(\mathbf{r})e^{i\tau\Delta\mathbf{K}\cdot\mathbf{r}}T_{\alpha,\tau}^{\mathrm{P/AP}}(\mathbf{r})\psi_{\mathbf{k}}(\mathbf{r}) = \tilde{t}_{\alpha}^{\mathrm{P/AP}}\big[\delta_{\mathbf{k},\mathbf{k}'} + \delta_{\mathbf{k}-\mathbf{k}',-\tau\mathbf{g}_2}e^{i\frac{4}{3}\tau\chi_{\mathrm{P/AP}}(\lambda_\alpha+1)} + \delta_{\mathbf{k}'-\mathbf{k},\tau\mathbf{g}_1}e^{i\frac{8}{3}\tau\chi_{\mathrm{P/AP}}(\lambda_\alpha+1)}\big]
$$

$$
- \sum_{\nu=-1,+1}\sum_{j=1}^{\mathcal{N}}q_{t_\alpha}^{\mathrm{P/AP}}\frac{t_{\alpha}^{\mathrm{P/AP}}}{2}\big(z_j^s - i\nu z_j^a\big)\big[\delta_{\mathbf{k}-\mathbf{k}',-\nu\mathbf{g}_j} + \delta_{\mathbf{k}-\mathbf{k}',-\tau\mathbf{g}_2-\nu\mathbf{g}_j}e^{i\frac{4}{3}\tau\chi_{\mathrm{P/AP}}(\lambda_\alpha+1)} + \delta_{\mathbf{k}-\mathbf{k}',\tau\mathbf{g}_1-\nu\mathbf{g}_j}e^{i\frac{8}{3}\tau\chi_{\mathrm{P/AP}}(\lambda_\alpha+1)}\big].
\tag{38}
$$

We point out that Eq. (38) is a direct generalization of the hybridization model presented in Ref. [48], which considered a rigid rotation of the TMD layers, and neglected out-of-plane relaxation.

Like Eq. (38), all matrix elements of Eqs. (32) and (34) contain a new momentum conservation rule $\mathbf{k} = \mathbf{k}' + \mathbf{g}_j$, consequence of the moiré superlattice periodicity, whereby wave vectors are only conserved up to a moiré vector $\mathbf{g}_j$. This determines the moiré Brillouin zone (mBZ) shown in Fig. 14(a) as a blue-shaded rhombus, defined by the first-star moiré vectors $\mathbf{g}_j$. Wave vectors $\mathbf{k}'$ outside this region of reciprocal space are "folded" into the mBZ as $\mathbf{k}' = \mathbf{k} \pm \mathbf{g}_j$, and treated as part of distinct minibands that couple vertically at wave vector $\mathbf{k}$, according to the matrix elements in Eq. (34). For instance, Fig. 14(b) shows a bottom-layer state of wave vector $\mathbf{k}$ near the K valley, and three out of the multiple top-layer states to which it couples by interlayer tunneling through the second term of Eq. (38).

In the following sections we show the low-energy Γ-, K- and Q-point electronic spectra of twisted P and AP bilayers for twist angles $\theta_{\mathrm{P/AP}} > \theta_{\mathrm{P/AP}}^*$, computed by direct diagonalisation of Eqs. (32), (34), and (36). The plane-wave basis used for the numerical calculations is large enough to provide convergence for several of the lowest conduction (highest valence) minibands.

A. Miniband structures near the Γ point for twisted AP and P bilayers

Figures 15(a) and 15(b) show valence minibands for twisted AP and P bilayers, respectively, computed numerically by the zone folding method described in Sec. VII. Each miniband is spin-degenerate due to time reversal symmetry of the Γ point.

AP structures exhibit extremely flat minibands ($\lesssim 1$ meV bandwidth) for twist angles up to $4°$. To gain insight into the origin of those minibands, we plot the modulus squared of their wave functions averaged over the entire mBZ in the left panels of Fig. 15(a). These show an array of QD states localized at 2H-stacking sites in the moiré supercell, where the valence band maximum for Γ point states was predicted in Sec. V A. The highest miniband represents an array of trigonally warped *s*-like states [49] (see Fig. 9), giving a realization of the SU_2 Hubbard model for Γ-point holes. Similarly, the next highest states are a *p*-like doublet formed by the trigonally warped *p* orbitals shown in the bottom-left panel of Fig. 15(a) [50].

P-bilayer minibands are shown in Fig. 15(b) for $2°$, $3°$, and $4°$ twist angles. At $\theta_{\mathrm{P}} = 4°$ the top two minibands exhibit a graphene-like dispersion of ≈ 15 meV bandwidth with two Dirac cones at the inequivalent mBZ points $\kappa = \Delta\mathbf{K}/2$ and $\kappa' = -\Delta\mathbf{K}/2$. As the twist angle decreases, the bandwidth of this miniband pair drops considerably, reaching values of ~ 1 meV at $2°$, but the gapless Dirac dispersion persists.

The real-space distribution of the top two miniband wave functions is shown in the left panels of Fig. 15(b) to consist of arrays of trigonally warped *s*-like orbitals centered at MX′ and XM′ stacking regions of the moiré supercell. These correspond, respectively, to bottom- and top-layer Γ-point valence states localized by the effective moiré potential (see Sec. VI A). Together, the bottom- and top-layer states form a bipartite triangular (honeycomb) lattice [Fig. 15(b) inset] whose sites are coupled by interlayer tunneling, constituting a graphene analog with mesoscopic-scale intersite distances [51].

Overall, for both P and AP structures, the top valence states at the Γ point can be described by mesoscale lattice models involving arrays of *s*- or *p*-like orbitals. Then, Coulomb
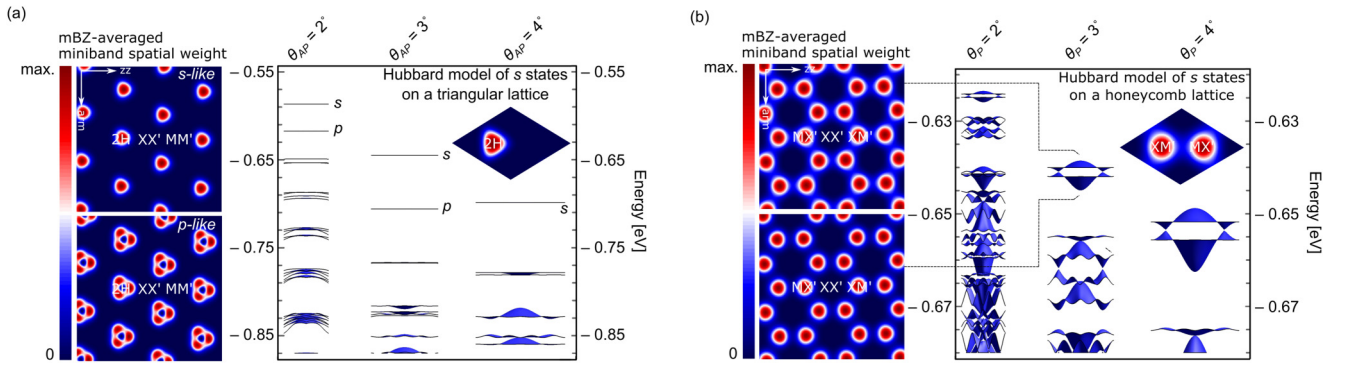
FIG. 15. Γ-point moiré valence miniband spectra of twisted AP (a) and P (b) WSe$_2$ bilayers, at large twist angles $\theta_{P/AP} = 2°$, $3°$, and $4°$. The left panels show the mBZ-averaged modulus squared of the wave function, representing the probability of finding a valence electron at a given position in the superlattice. AP bilayers exhibit flat minibands corresponding to a triangular lattice of quantum dots at 2H regions. The unit cell is shown in the inset. P bilayers exhibit graphene-like dispersions with two gapless Dirac cones inside the mBZ, and bandwidths ranging from ∼1 meV at $2°$ to ∼10 meV at $4°$. The graphene-like bands originate from a honeycomb lattice of states localized at MX′ and XM′ sites, coupled by interlayer tunneling. All energies are measured with respect to the monolayer WSe$_2$ VB edge.

interactions will be significant for these sites, giving rise to mesoscopic realizations of the Hubbard model on a triangular (AP structures) or a honeycomb lattice (P structures), potentially leading to strongly correlated ground states [6,52,53].

B. Miniband structures near the K point for twisted AP bilayers

Figure 16(a) shows both valence and conduction K-point minibands for twisted AP bilayers of WSe$_2$, where the moiré superlattice is dominated by the piezoelectric potential. By
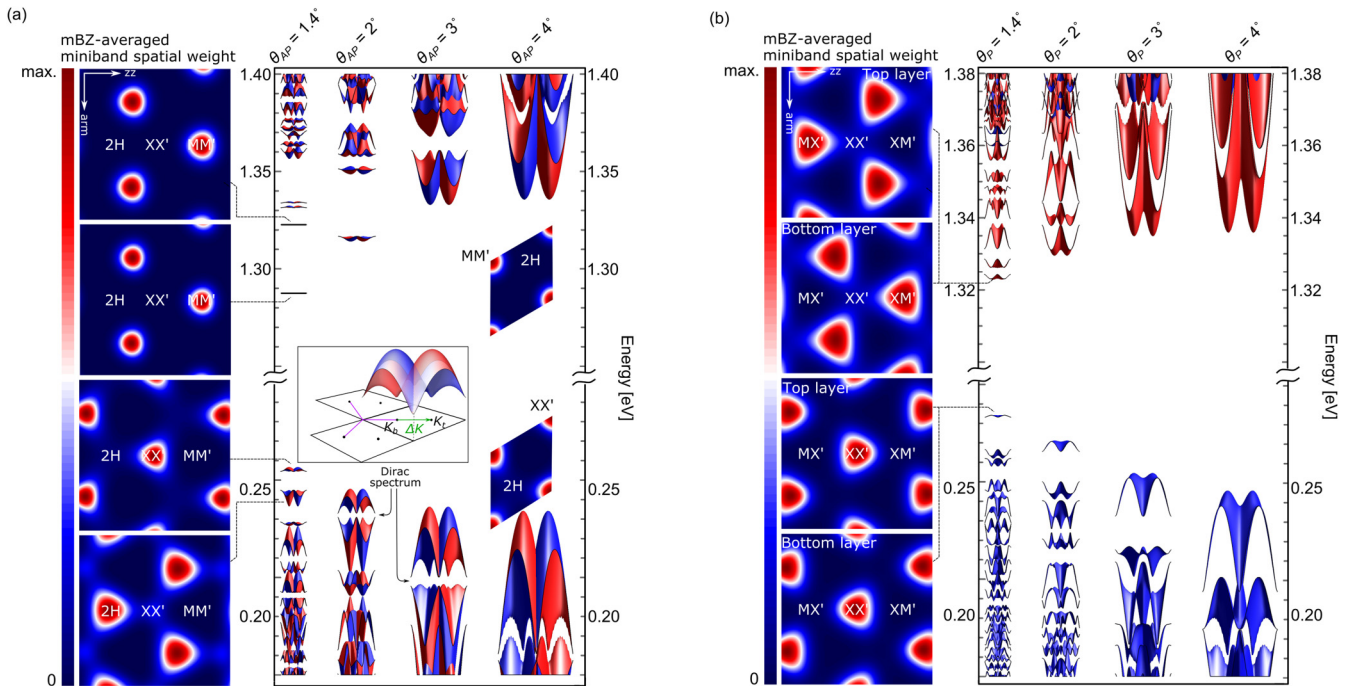
FIG. 16. K-point moiré miniband spectra of twisted AP (a) and P (b) WSe$_2$ bilayers, at large twist angles $\theta_{P/AP} = 1.4°$, $2°$, $3°$, and $4°$. Spin-up and spin-down minibands are shown in red and blue, respectively. (a) For twisted AP bilayers, the bottom (top) two flat conduction minibands appearing for $\theta_{AP} = 1.4°$ correspond to conduction (valence) states localized at MM′ (XX′) sites in the supercell, as shown in the top (bottom) left panels. The conduction and valence band edges can be effectively described by mesoscale triangular lattices with unit cells depicted in the top-right and bottom-right insets, respectively. The left inset shows part of the extended mBZ to illustrate the three minibands responsible for the Dirac-like dispersion observed at the mBZ corner for $\theta_{AP} > 2°$. (b) For twisted P bilayers with twist angles $\theta_P = 1.4°$ and $2°$, top- (bottom-) layer conduction states localize at MX′ (XM′) sites, as shown by the layer-resolved probability density maps in the left panels, forming two nearly decoupled triangular lattices. By contrast, valence states localize at XX′ regions, forming a single mesoscale triangular lattice. All energies are measured with respect to the monolayer WSe$_2$ VB edge, for direct comparison with the K-point miniband spectra of Fig. 15.

contrast to the Γ point, electronic states at the K point are spin-split by the SO interaction. Spin-up (-down) states are shown in red (blue) in Fig. 16. Band hybridization takes place exclusively between same spin bands in opposite layers, which in this configuration are separated by the SO splittings. For both the valence and conduction bands, the SO splittings are a whole order of magnitude larger than the corresponding tunneling energies (see Table III), resulting in weak interlayer hybridization. As a consequence, the interlayer distance modulation Eq. (4) is also negligible in this case, since it only enters the hybridization Hamiltonian.

1. Valence band

For $\theta_{AP} > 2°$, the top valence states are delocalized, forming two degenerate spin-polarized parabolic minibands with maxima at the mBZ wave vectors κ and κ', respectively. Note that this and the next highest miniband are separated by a gapped Dirac dispersion at the mBZ corner. This is caused by three degenerate bottom-layer plane-wave states, $|\kappa - \Delta \mathbf{K}\rangle$, $|\kappa - \Delta \mathbf{K} + \mathbf{g}_3\rangle$ and $|\kappa - \Delta \mathbf{K} - \mathbf{g}_1\rangle$, with $\kappa - \Delta \mathbf{K}$ the mBZ corner, that fold upon each other and then get split by the first harmonic of the moiré perturbation in Eq. (34).

In the lowest harmonics approximation, the resonant mixing of those three states and the folded plane-wave states with close wave numbers $\mathbf{k} = \kappa - \Delta \mathbf{K} + \mathbf{q}$ ($|\kappa - \Delta \mathbf{K} + \mathbf{q}\rangle$, $|\kappa - \Delta \mathbf{K} + \mathbf{g}_3 + \mathbf{q}\rangle$ and $|\kappa - \Delta \mathbf{K} - \mathbf{g}_1 + \mathbf{q}\rangle$) is described (up to an overall energy shift) by the Hamiltonian

$$H_{corner}^{AP}(\mathbf{q}) = \begin{pmatrix} \delta_1(\mathbf{q}) & -e\varphi_1 & -e\varphi_1^* \\ -e\varphi_1^* & \delta_{2,+}(\mathbf{q}) & -e\varphi_1 \\ -e\varphi_1 & -e\varphi_1^* & \delta_{2,-}(\mathbf{q}) \end{pmatrix},$$

$$\delta_1 = 2\frac{\hbar^2|\Delta \mathbf{K}|}{m_{VB,K}} q_x, \quad \delta_{2,\pm} = -\frac{\hbar^2|\Delta \mathbf{K}|}{m_{VB,K}}(q_x \pm \sqrt{3}q_y).$$
$$(39)$$

Here, $m_{VB,K}$ is the valence-band effective mass, φ_1 is the amplitude of the first piezopotential moiré harmonic (see Appendix F), and we point out that $\text{Re}\varphi_1 > 0$, $\text{Im}\varphi_1 > 0$.

Diagonalising the matrix in Eq. (39) at $\mathbf{q} = \mathbf{0}$ gives the energy levels $\varepsilon_0 = -2e\text{Re}\varphi_1$ and $\varepsilon_\pm = e\text{Re}\varphi_1 \mp e\sqrt{3}\text{Im}\varphi_1$, with $\varepsilon_\pm > \varepsilon_0$, and the eigenvector matrix U. Shifting the energy reference to $e\text{Re}\varphi_1$, applying the similarity transformation $\tilde{H}_{corner}^{AP} = U^{-1}H_{corner}^{AP}(\mathbf{q})U$ and projecting out the level ε_0, we obtain the effective Hamiltonian

$$\tilde{H}_{corner}^{AP}(\mathbf{q}) \approx \begin{pmatrix} \sqrt{3}\text{Im}\varphi_1 & \hbar v_D q_- \\ \hbar v_D q_+ & -\sqrt{3}\text{Im}\varphi_1 \end{pmatrix},$$

$$q_\pm = e^{\pm i\frac{2\pi}{3}}(q_x \pm iq_y), \quad v_D = \frac{\hbar|\Delta \mathbf{K}|}{m_{VB,K}}. \quad (40)$$

Here, we used an expansion up to linear order in $\mathbf{q}$ to highlight the Dirac-like features identified in Fig. 16(a), with v_D the effective Fermi velocity, and $2\sqrt{3}\text{Im}\varphi_1$ the "Dirac mass."

At angles $\theta_{AP}^* < \theta_{AP} < 2°$, the valence band edge consists of a flat (2 meV bandwidth at $\theta_{AP} = 1.4°$), spin-degenerate miniband. The mBZ-averaged probability densities shown in the bottom-left panels of Fig. 16(a) indicate that this miniband is formed by an array of weakly coupled states localized at superlattice sites where the piezopotential is maximum (XX' areas). These are the s_0 QD states discussed in Sec. V B,

whereas QD orbitals delocalize already at $\theta = 1.4°$. Accounting for spin and valley degeneracies, the QD states forming the top valence miniband give a realization of the SU_4 Hubbard model on a triangular lattice [54].

2. Conduction band

Remarkably, the conduction band edge consists of a spin-degenerate doublet of extremely flat (<0.1 meV bandwidth at $\theta_{AP} = 1.4°$) minibands, formed by s-type QD states localized at MM' areas of the superlattice, where the piezopotential is minimum [top-left panels of Fig. 16(a)]. As a result, for twist angles $\theta_{AP} < 2°$, the conduction-band-edge states are well described by a periodic array QD states with the supercell shown in the top-right inset of Fig. 11(b), also giving a realization of the SU_4 Hubbard model on a triangular lattice.

C. Miniband structures near the K point for twisted P bilayers

In contrast to the K-point states in AP structures, in P bilayers hybridization is resonant, hence strong. Another difference from AP structures is that, as discussed in Sec. VI, the valence band edge is dominated by interlayer hybridization at XX' regions, whereas for the conduction band a weaker interlayer hopping (see Table III) shifts the band edge toward MX' and XM' regions for small twist angles. Figure 16(b) shows the miniband spectra of twisted P bilayers at twist angles $\theta_P = 1.4°$, $2°$, $3°$, and $4°$.

1. Valence band

For $\theta_P > 2°$ the top valence minibands have relatively large bandwidths (~ 50 meV for $\theta = 4°$), corresponding to delocalized carriers. However, narrow minibands appear for $\theta_P = 1.4°$ and $2°$, corresponding to valence electrons localized at XX' regions of the supercell. This is highlighted in the bottom-left panels of Fig. 16(b), where we plot the layer-resolved mBZ-averaged modulus squared of the top miniband wave function. Note that, due to resonant hybridization, the states are evenly spread between the two layers.

2. Conduction band

Similarly to the valence band case, K-point conduction electrons are delocalized for $\theta > 2°$, whereas for $\theta_P = 1.4°$, $2°$ the states become localized. In the conduction band case, however, electrons are localized by the combined piezo- and ferroelectric potential at XM' and MX' sites, forming two separate mesoscale triangular lattices, shown in the top-left panels of Fig. 16(b). Given the weak interlayer hybridization between conduction bands (see Table III), these two lattices couple only weakly, and a graphene-like spectrum does not develop.

D. Miniband structures near the Q point for twisted AP and P bilayers

Figures 17(a) and 17(b) show the Q_1-point conduction minibands of twisted AP and P bilayers, respectively, for large twist angles $\theta_{P/AP} = 1.4°$, $2°$, $3°$, and $4°$.
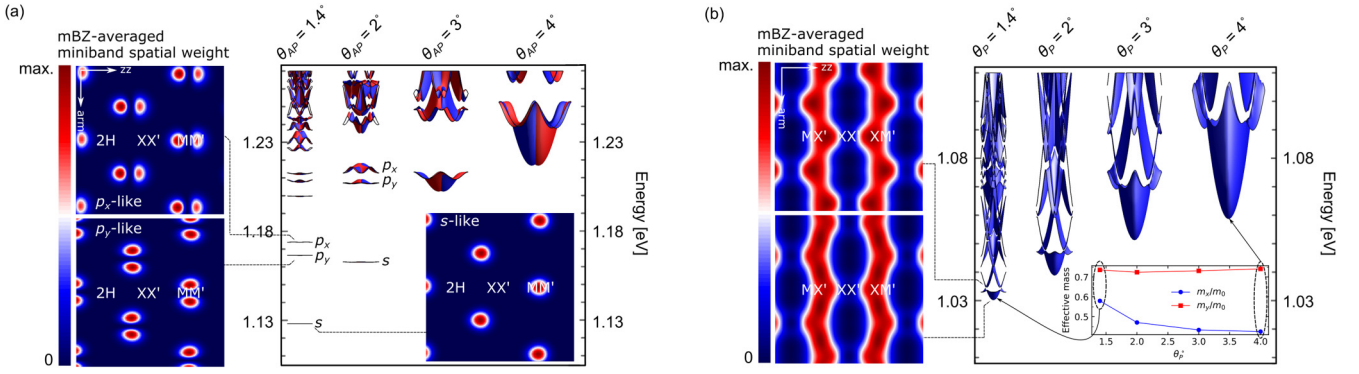
FIG. 17. Q-point moiré conduction miniband spectra of twisted AP (a) and P (b) WSe$_2$ bilayers, at large twist angles $\theta_{P/AP} = 2°$, $3°$, and $4°$. For P bilayers, the in-plane relaxation vectors $\mathbf{u}^t(\mathbf{r})$ and $\mathbf{u}^b(\mathbf{r})$ are considered to first order in the minibands calculation, as discussed in the main text. The inset in (b) shows the effective masses (top panel) and the ratio of the root-mean-squared group velocities (bottom panel) in the x (zigzag) and y (armchair) directions of the lowest miniband, for each of the twist angles considered. The left panels in (a) and (b) and the inset of (a) show the mBZ-averaged modulus squared of the wave function, representing the probability of finding a valence electron at a given position in the superlattice. All energies are measured with respect to the monolayer WSe$_2$ VB edge.

AP structures display spin-degenerate, flat minibands for twist angles $\theta_{AP}^* < \theta_{AP} \lesssim 2°$ [Fig. 17(a)], corresponding to arrays of localized states at MM′ regions of the superlattice. Q_1 point electrons are localized by the piezopotential and interlayer hybridization, which combine to produce deep potential wells at these sites. The inset and two left panels of Fig. 17(a) show the mBZ-averaged moduli squared of the three lowest miniband wave functions for $\theta_{AP} = 1.4°$. The lowest of these is an s-type state with slight trigonal warping, followed by a p_y-like state, and then by a p_x-like state at higher energy. The splitting of the two p states is caused by the mass anisotropy of the monolayer states, and their order is a consequence of the fact that $m_y > m_x$.

In addition to spin degeneracy, each of these localized states is also degenerate with the inequivalent $-Q_1$ and $\pm Q_2$

and $\pm Q_3$ valleys, giving a total degeneracy factor of 12. Therefore, in the presence of interactions, we predict that n-doped twisted WSe$_2$ constitutes a realization of the SU$_N$ Hubbard model with large-N for the smallest twist angles [55].

In the case of P structures with twist angles $\theta_P < 2°$, we find that the Q_1-point minibands are more sensitive to neglecting in-plane relaxation of the lattice. Therefore, we expanded the relaxation field in moiré harmonics as

$$\mathbf{u}^t(\mathbf{r}) - \mathbf{u}^b(\mathbf{r}) = \sum_j \mathbf{u}_j \sin(\mathbf{g}_j \cdot \mathbf{r}). \quad (41)$$

The expansion coefficients $\mathbf{u}_j$ are reported in Appendix F. Then, with a procedure analogous to that leading to Eq. (37), we approximate the Q_1-point interlayer hybridization term as ($\mathbf{V}_0 = \mathbf{0}$, $\mathbf{V}_1 = -\mathbf{G}_1$, $\mathbf{V}_2 = \mathbf{G}_2$, $\mathbf{V}_3 = \mathbf{G}_3$, $\mathbf{V}_4 = -\mathbf{G}_3$)

$$e^{i\Delta\mathbf{Q}\cdot\mathbf{r}} T_Q^P(\mathbf{r}) = e^{i\Delta\mathbf{Q}\cdot\mathbf{r}} \sum_{\ell=0}^4 t_{Q,\ell}^P e^{-q_{t_{Q,\ell}} z(\mathbf{r})} e^{i\mathbf{V}_\ell \cdot [\theta_P \hat{\mathbf{z}} \times \mathbf{r} + \mathbf{u}^t(\mathbf{r}) - \mathbf{u}^b(\mathbf{r})]}$$

$$= e^{i\Delta\mathbf{Q}\cdot\mathbf{r}} \sum_{\ell=0}^4 \tilde{t}_{Q,\ell}^P e^{-q_{t_{Q,\ell}} \sum_{j=1} z_j^s \cos(\mathbf{g}_j \cdot \mathbf{r})} e^{i\mathbf{v}_\ell \cdot \mathbf{r}} e^{i\sum_j \mathbf{V}_\ell \cdot \mathbf{u}_j \sin(\mathbf{g}_j \cdot \mathbf{r})}$$

$$\approx e^{i\Delta\mathbf{Q}\cdot\mathbf{r}} \sum_{\ell=0}^4 \left[\tilde{t}_{Q,\ell} e^{i\mathbf{v}_\ell \cdot \mathbf{r}} + \sum_{j=1} \frac{\tilde{t}_{Q,\ell} \mathbf{V}_\ell \cdot \mathbf{u}_j}{2} \left(e^{i(C_3^\mu \mathbf{g}_j + \mathbf{v}_\ell)\cdot\mathbf{r}} - e^{-i(C_3^\mu \mathbf{g}_j - \mathbf{v}_\ell)\cdot\mathbf{r}} \right) - \frac{q_{t_{Q,\ell}} \tilde{t}_{Q,\ell}}{2} \sum_j z_j^s \left(e^{i(\mathbf{g}_j + \mathbf{v}_\ell)\cdot\mathbf{r}} + e^{-i(\mathbf{g}_j - \mathbf{v}_\ell)\cdot\mathbf{r}} \right) \right], \quad (42)$$

where $\tilde{t}_{Q,\ell} \equiv e^{-q_{t_{Q,\ell}} z_0} t_{Q,\ell}$; the moiré vectors $\mathbf{v}_0 = \mathbf{0}$, $\mathbf{v}_1 = -\mathbf{g}_1$, $\mathbf{v}_2 = \mathbf{g}_2$, $\mathbf{v}_3 = \mathbf{g}_3$ and $\mathbf{v}_4 = -\mathbf{g}_3$ appear from the approximation $\mathbf{G}_\ell \cdot (\theta\hat{\mathbf{z}} \times \mathbf{r}) \approx \mathbf{g}_\ell \cdot \mathbf{r}$; and we have used the fact that, for P bilayers, all coefficients z_j^a in Eq. (4) vanish (see Appendix F). The matrix elements are then obtained by integrating Eq. (42) between two plane-wave states, as in Eq. (38) above. The minibands shown in Fig. 17(b) were computed based on these matrix elements, and their analogs for the intralayer term $\varepsilon_Q^P(\mathbf{r})$.

The P bilayer minibands exhibit dispersive bands for all twist angles considered, as shown in Fig. 17(b). Miniband formation is dominated by the modulation of interlayer hybridization across the lattice, caused by the variation of the interlayer distance and the in-plan relaxation field, and only weakly affected by the piezo- and ferroelectric potentials. The anisotropic features of the electron states are more clearly appreciated in the mBZ-averaged moduli squared of the wave functions, in the left panels of Fig. 17(b).

Mirroring the band-edge landscapes of Fig. 13, electrons in the bottom two minibands for $\theta_P = 1.4°$ are confined into channels that run roughly along the armchair direction, passing through MX′ and XM′ regions of the moiré superlattice, and avoiding XX′ areas where interlayer hybridization is weak.

For all twist angles considered, we quantify the lowest miniband anisotropy by computing the effective masses along the x (zigzag) and y (armchair) directions, shown in the inset of Fig. 17(b). The large monolayer mass anisotropy is recovered for large twist angles $\theta_P = 4°$, whereas in the small twist angles regime anisotropy is somewhat reduced by the interlayer hybridization effect. In the presence of interactions, the anisotropic states of valley Q_1 discussed in Fig. 17 must be considered simultaneously with those of valleys Q_2 and Q_3, with which it is connected by C_3 rotations, and their corresponding time reversal partners $-Q_1$, $-Q_2$, and $-Q_3$.

VIII. TUNING ALIGNED BILAYERS BY STRAIN, PRESSURE, ELECTRIC FIELD, AND ENCAPSULATION

The TMDs feature in their valence/conduction bands competing local maxima/minima, known as "valleys." These are the Γ and K/K' valleys in the valence band, and the Q and K/K' valleys in the conduction band. Depending on the member of the TMD family involved, on the number of layers, and on external factors, which of these valleys form the band edges in an ultrathin TMD film can be tuned.

From our discussions above, and from the band energies set out in Table V, we note that the energy differences between the local valence band maxima at Γ and K are small, with the band edge of 2H (MX′/XM′) bilayer WSe$_2$ at K only around 40 meV(80 meV) above that at Γ. The conduction band also features two competing minima in the Brillouin zone, with the valleys at Q and K $\sim$ 130 meV apart in energy.

This opens up the possibility of controlling which valleys form the conduction and valence band edges using external parameters, such as displacement fields from gating and modification of the lattice parameters through strain [56–63] and pressure (the latter of which may be induced by electrostatic attraction between top and back gates).

A. Modulation of band edges by pressure and strain

To investigate the effects of tuning via external parameters, we begin by exploiting the models presented above. We use their description of the interlayer distance dependence of valence band hybridization to describe the change in the location of the valence band maximum (VBM) from Γ to K as the interlayer distance reduces under pressure. To do this, we make two approximations. First, we note that the variation in the K-point energy with interlayer distance is much smaller than that at Γ, so we approximate the change in Γ-K splitting by the change in the Γ-point energy alone. Second, we keep only the dominant contributions to the interlayer hybridization model, H_Γ^{AP} from Eq. (8). With these two approximations, the variation in the Γ-K splitting can be written as

$$\frac{dE_{\Gamma-K}}{dz} \simeq \frac{dv_{\Gamma,0}^{AP}(z)}{dz} + \frac{1}{2}\left[\frac{dt_0^{AP}(z)}{dz} - \frac{3}{2}\frac{dt_1^{AP}(z)}{dz}\right], \quad (43)$$

TABLE V. Wave function projection onto spherical harmonics in band-edge states (Q_1 approximated as being at $K/2$) of aligned 2L-WSe$_2$ in 2H and MX′ stacking (M$_i$ and X$_i$ are the total metal and chalcogen contributions on layer i), the expectation value of the electric dipole moment in each wave function calculated from the orbital projections (d_z), and the band energy (0 eV set to mean of vacuum levels). For 2H stacking, the band energies appear in spin-degenerate pairs due to inversion symmetry. At Γ, their wave functions are spread symmetrically over the layers. Elsewhere in the Brillouin zone within each degenerate pair, bands of opposing spin are polarized on opposing layers, with the polarization quantified by the dipole moment d_z. The spin-degeneracy of the bands in the 2H case is absent for MX′ stacking due to the inversion asymmetry of P bilayers.

			2H-WSe$_2$			
Band	M$_1$	X$_1$	M$_2$	X$_2$	$d_z(e \cdot \text{Å})$	Energy (eV)
VB, Γ	0.355	0.127	0.355	0.127	0.000	−4.908
VB-1, Γ	0.355	0.127	0.355	0.127	0.000	−4.908
VB-2, Γ	0.395	0.104	0.395	0.104	0.000	−5.555
VB-3, Γ	0.395	0.104	0.395	0.104	0.000	−5.555
VB, K	0.800	0.175	0.019	0.007	−3.070	−4.858
VB-1, K	0.019	0.019	0.800	0.175	3.070	−4.858
VB-2, K	0.820	0.165	0.016	0.002	−3.130	−5.332
VB-3, K	0.016	0.002	0.820	0.165	3.130	−5.332
CB, K	0.931	0.068	0.002	0.000	−3.229	−3.504
CB+1, K	0.002	0.000	0.931	0.068	3.229	−3.504
CB+2, K	0.941	0.060	0.000	0.000	−3.242	−3.460
CB+3, K	0.000	0.000	0.941	0.060	3.242	−3.460
CB, Q	0.230	0.088	0.461	0.221	1.194	−3.634
CB+1, Q	0.461	0.221	0.230	0.088	−1.194	−3.634
CB+2, Q	0.244	0.102	0.467	0.176	1.044	−3.160
CB+3, Q	0.467	0.176	0.244	0.102	−1.044	−3.160

			MX′-WSe$_2$			
Band	M$_1$	X$_1$	M$_2$	X$_2$	$d_z(e \cdot \text{Å})$	Energy (eV)
VB, Γ	0.384	0.151	0.329	0.137	−0.215	−4.910
VB-1, Γ	0.384	0.151	0.329	0.137	−0.215	−4.910
VB-2, Γ	0.367	0.100	0.423	0.111	0.202	−5.501
VB-3, Γ	0.367	0.100	0.423	0.111	0.202	−5.501
VB, K	0.810	0.180	0.006	0.004	−3.186	−4.820
VB-1, K	0.001	0.001	0.818	0.178	3.227	−4.888
VB-2, K	0.822	0.170	0.004	0.002	−3.209	−5.279
VB-3, K	0.002	0.001	0.828	0.169	3.223	−5.346
CB, K	0.002	0.000	0.931	0.067	3.232	−3.530
CB+1, K	0.001	0.000	0.940	0.059	3.240	−3.489
CB+2, K	0.932	0.066	0.002	0.000	−3.234	−3.474
CB+3, K	0.939	0.059	0.002	0.000	−3.232	−3.433
CB, Q	0.249	0.125	0.418	0.208	0.816	−3.647
CB+1, Q	0.301	0.121	0.412	0.167	0.500	−3.512
CB+2, Q	0.429	0.158	0.263	0.116	−0.824	−3.323
CB+3, Q	0.409	0.157	0.318	0.118	−0.431	−3.098

with the functions $v_{\Gamma,0}^{AP}(z)$, $t_0^{AP}(z)$, and $t_1^{AP}(z)$ defined and parametrized in Table II. For 2H stacking we use $z = -0.23$ Å, which gives $\frac{dE_{\Gamma-K}}{dz} \simeq -470$ meV/Å. To convert this into a pressure sensitivity, we estimate from Eq. (1) that a 1% change in d for 2H stacking can be acheived with a pressure of 4.29 kbar corresponding to a sensitivity to pressure of $\sim$7 meV/kbar.
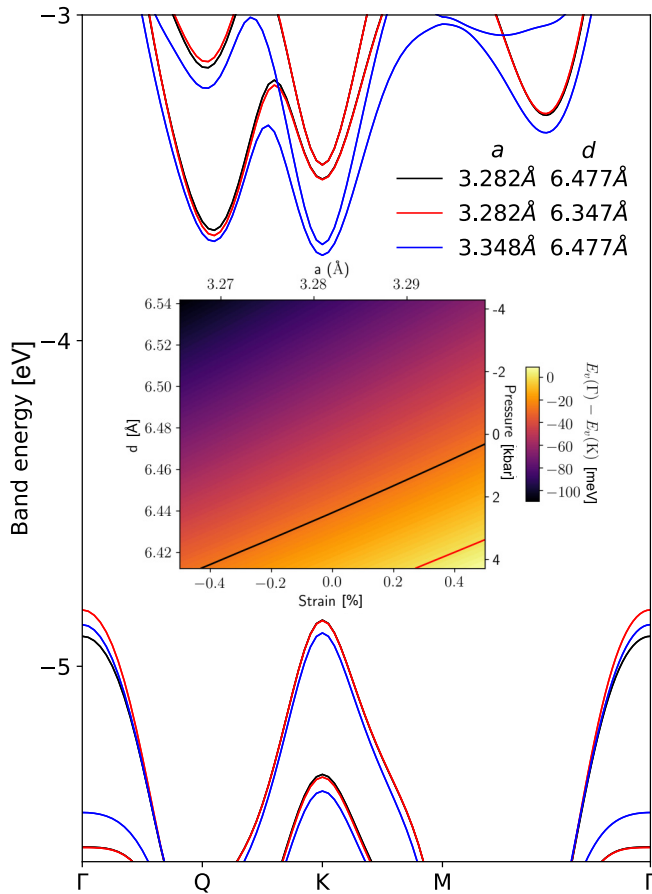
FIG. 18. Band structure of 2H-stacked 2L-WSe$_2$ for 0 strain and pressure (black lines), 8.6 kbar uniaxial pressure (red lines), and 2% biaxial tensile strain (blue lines). Bands are aligned relative to vacuum. Inset: map of difference between Γ- and K-point valence-band-edge energies under strain and pressure. The red line shows the boundary across which the band edge moves from K to Γ, while the black line separates the regions in which the lowest energy exciton involves a hole at K or at Γ.

We compare the results from those using Eq. (43) with results directly calculated from DFT. Bands for bilayers of 2L-WSe$_2$ in 2H stacking calculated using DFT are exemplified in Fig. 18, for structural parameters of the monolayer taken from experiments [34]. We also show the band dispersions computed for a slightly smaller interlayer separation (corresponding to a pressurized material). As found through the modeling above, a reduction in interlayer distance through pressure increases the interlayer hybridization and band splitting at the Γ point, reducing the difference between the valence band edge at K and the local maximum at Γ. The change in Γ-K splitting with pressure found directly from DFT is approximately 9 meV/kbar, close to that found from the model keeping only the most dominant terms.

In Fig. 18, we also show DFT results using a slightly inflated lateral lattice constant (mimicking biaxial strain). These show that strain may also be used to tune the location of the VBM in the BZ between the K point and the Γ point. Quantitatively, the Γ-K valence band splitting in 2H bilayer WSe$_2$ varies, to linear order at a rate of $\sim$40 meV/strain(%),

from which we can predict that the crossover from the VBM being located at K to being at Γ would take place at $\sim$1% strain.

The conduction band edge of WSe$_2$ bilayers exhibits some tunability as well. In the equilibrium structure, the conduction band minimum (CBM) is at the Q point, and there is a local minimum at K. The splitting between the K- and Q-point CB minima ($\sim$130 meV) is much greater than that between K and Γ in the VB, and the sensitivity of the energy splitting between the Q and K valleys to interlayer distance is weak, so changing the inter-layer spacing d over the ranges considered here does not affect the position of the CBM. However, there is a strong sensitivity of the CB K-point energy to strain, with the K-Q splitting tunable by 100 meV/% strain, such that >1.5% strain can push the K valley below the Q valley. This effect has been demonstrated experimentally in the onset of much stronger photoluminescence in strained bilayer WSe$_2$ [64] as the CBM moves to K. The tunability of the conduction band may be able to influence superconductivity which can be engineered in n-doped 2D crystals [65]. Changing the position of the CBM will impact the density of states, in part due to the change in effective masses, but also because one valley has a sixfold degeneracy in the Brillouin zone (Q) while the other is only twofold degenerate (K).

We also use the DFT results to estimate the effective mass of the valence band holes in bilayer WSe$_2$ and find very different $m_{VB}(\Gamma) = -1.14 \; m_e$ and $m_{VB}(K) = -0.37 \; m_e$ masses (as well as conduction band masses of $m_{CB}(K) = 0.41 \; m_e$, $m_{CB}^{xx}(Q) = 0.45 \; m_e$, and $m_{CB}^{yy}(Q) = 0.62 \; m_e$). Then, we feed these values into an analytical interpolation formula based on diffusion Monte Carlo calculations [66] for 2D materials with the Keldysh interaction and evaluate the exciton binding energies, where we use the value of the screening length $r_* = 45.11$ Å from GW calculations [67] for monolayer WSe$_2$ which doubles for the bilayer, resulting in $r_* = 90.22$ Å.

With the help of the code provided in the Supplemental Material of Ref. [66], we find that the binding energy for excitons comprising an electron at Q with a hole at K or Γ for 2L-WSe$_2$ encapsulated in hexagonal boron nitride ($\varepsilon_{hBN} = 3.73$ [68]) $E_b^{VB(\Gamma)\to CB(Q)} = 162$ meV and $E_b^{VB(K)\to CB(Q)} = 135$ meV, respectively. The 27 meV difference between the two exciton binding energies promotes Γ-point hole excitons, which moves the boundary between regions in which the lowest energy exciton involves a hole at K or Γ. For completeness, we also estimate exciton binding energies for suspended bilayers, for which we obtain $E_b^{VB(\Gamma)\to CB(Q)} = 334$ meV and $E_b^{VB(K)\to CB(Q)} = 299$ meV. In the conduction band, the difference between the exciton binding experienced by an electron at K compared with one at Q is smaller, by $\sim$6 meV. Given the $\sim$100 meV/% dependence of the K-Q splitting on strain, the effect of the difference in exciton binding on the K-Q band-edge crossover is a small one.

In MX′/XM′ P-stacked 2L-WSe$_2$, the small splitting in the band edges at the K point described above increases the energy difference between the VBM itself and the local VBM at Γ, and reduces that between the conduction band edges at Q and K. Since the behavior of the band-edge energies under pressure and strain, as shown in Fig. 19, remains very similar to that of the 2H-stacked bilayer, this results in a larger pressure and/or strain being needed to realize a transition of
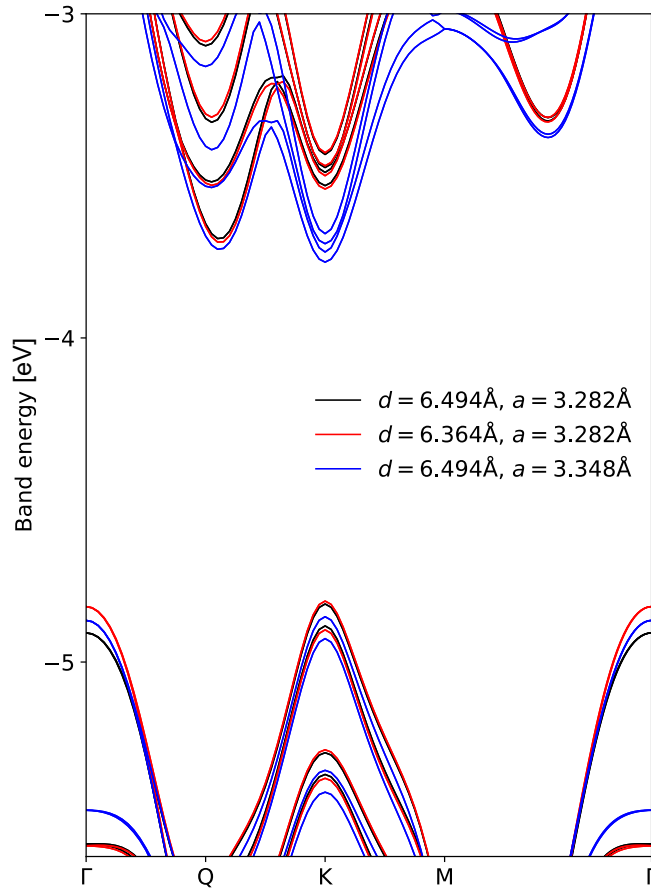
FIG. 19. Band structure of MX′/XM′-stacked 2L-WSe$_2$ for 0 strain and pressure (black lines), 8.6 kbar uniaxial pressure (red lines), and 2% biaxial tensile strain (blue lines). Bands are aligned relative to mean of vacuum levels on either side of bilayer.

the VBM to the Γ point, while the crossover for the CBM from Q to K can be expected to happen at a smaller strain. The exciton binding energies can be obtained for 3R stacking in the same way as set out for 2H stacking above. With the exception of the valence band effective mass at Γ (which increases from 1.15 m_e in 2H stacking to 1.26 m_e in MX′/XM′ stacking) all band-edge effective masses change by no more than 3% between the two types of stacking, which leads to no more than 4 meV change in the values of exciton binding energies in MX′/XM′ stacking as compared to 2H.

B. Modulation of band edges by electric displacement field

A vertical electric field can also be used to tune the band-edge alignment in the bilayer, because it splits the non-hybridized K-point band edges but does not change much the energy of the strongly hybridized layer-symmetric and -antisymmetric states at Γ, and has an opposite effect to pressure and strain, further promoting the VBM at the K point. In Table V we give the electric dipole moment, d_z, of each wave function as obtained from the orbital projections. Note that in the case of 2H stacking, the inversion symmetry results in spin degenerate states where each spin component on its own has a dipole moment (except at the Γ point), where each component can be localized on a separate layer. Within each

degenerate pair, the bands have the same magnitude of d_z but with opposing signs, thus giving a band splitting away from Γ of magnitude $2|E_z d_z|$, where E_z is the perpendicular electric field across the WSe$_2$ bilayer. Since the Γ-point VB energy is not affected at linear order by an electric field, this has the effect of increasing the difference in energy between the K-point VBM and the VB at Γ by an amount $|E_z d_z|$. For 2H WSe$_2$, an electric field $|E_z| = 0.1$ V/nm would be expected to increase the energy of the top valence band at K relative to that at Γ by ~30 meV.

For MX′/XM′ stacking, as noted in the case of bilayer MoSe$_2$ [17] the energy splitting between the layer-polarized states discussed above will either increase or decrease, depending on the direction of the applied electric field relative to the orientation of the domain (that is, MX′ or XM′). Where the applied field points in a direction opposite to the intrinsic field due to charge transfer, it will decrease the splitting of the top two valence bands at K (so decreasing the difference between the VBM at K and the VB at Γ) through the addition of $E_z d_z$ to the energies of VB and VB-1 (see Table V). This will lead to the two layer-polarized bands approaching each other when $E_z \sim +0.1$ V/nm, beyond which their splitting will increase once more.

In terms of the conduction band, the splitting at zero field between the Q- and K-point minima (130 and 117 meV for 2H and MX′/XM′ stacking, respectively) means that a much larger electric field would be required to move the band edge from the Q to the K point. Furthermore, the Q-point conduction band also has a finite dipole moment, so it also shifts at linear order under an applied field, albeit at a slower rate. Taken together, this means that an applied field $E_z \sim 0.7$ V/nm would be required to bring the Q- and K-point minima to a similar energy.

C. Encapsulation effect on the band-edge alignment

So far, except for strong perturbations from external influences such as strain and pressure, and independently of twist angle in twisted bilayers, the band edges in our modeling have been found to be at the K and Q points for the valence and conduction bands, respectively, of WSe$_2$ bilayers. Even so, we have considered maps and minibands associated with the valence Γ-point and conduction K-point states in this study. This is because, while the DFT results from which parameters for the models were obtained considered WSe$_2$ suspended in vacuum, real experimental devices will often be constructed featuring WSe$_2$ in contact with other 2D (or bulk) materials, which could affect the relative energies of the band-edge states and other local maxima/minima.

The construction of 2D material heterostructures can be associated with hybridization between the bands of the material of interest with those of the encapsulating material, in particular where orbitals (such as s and p_z) are concerned, where the wave functions extend from the 2D material surface and overlap at the interface between the encapsulated and encapsulating materials. Encapsulation of 2D materials by hexagonal boron nitride (hBN) is a common step undertaken in the fabrication of high-quality 2D material-based devices [69–72]. hBN is chosen as an encapsulating material for reasons including its stability in air, as an atomically flat
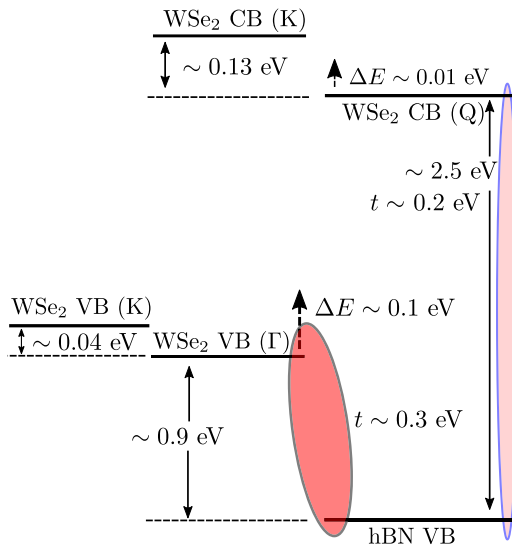
FIG. 20. Schematic band diagram of WSe$_2$ encapsulated by hBN, showing how hybridization between the hBN and the Γ-point valence band of WSe$_2$ could potentially push the Γ-point valence band above the maximum at K, while such effects on the Q-point conduction band are likely to be too small to change the band-edge location.

interface, and since its large band gap allows a type II band alignment with many materials of interest. Care must still be taken, however, to understand whether any of the hBN and 2D material bands may be aligned closely enough for the effects of interlayer hybridization between them to become significant. In Fig. 20 we sketch the band alignment of thick hBN and 2H-bilayer WSe$_2$, approximated from the band alignment of graphene and hBN [73], that of graphene and WSe$_2$ [74], and a scanning tunneling spectroscopy measurement of the quasiparticle band gap [75]. The valence band of hBN lies only a small difference in energy ($\sim$0.9 eV) below that of WSe$_2$, and could hybridize strongly with the Γ point valence band, while we expect effects on the K point to be weak as the K-point states are localized on the inside of the WSe$_2$ layers. Using the resonant Γ-point valence band interlayer tunneling strength for WSe$_2$ as an order-of-magnitude estimate of the likely strength of tunneling resulting from hybridization between the Γ point states of WSe$_2$ and hBN, we can estimate the magnitude of the resulting upwards shift in energy of the WSe$_2$ Γ-point valence band states. This is found to be $\sim$100 meV, which would be enough to change the order of the valence band valleys, shifting the valence band maximum to the Γ point. A similar but much smaller effect (we estimate the energy shift to be $\sim$10 meV) could also be expected for the Q point in the conduction band, which would reduce the splitting slightly between the Q and K/K' valleys [76]. Such effects of interlayer hybridization should also be considered in other heterostructures, such as WSe$_2$-InSe [77].

IX. DISCUSSION

In this work, we have developed hybrid $\mathbf{k} \cdot \mathbf{p}$ tight-binding models to study the variation of conduction and valence band-edge energies and moiré miniband structures in twisted P- and AP-WSe$_2$ bilayers caused by a number of factors: lattice

reconstruction, piezoelectric charges, interlayer hybridization and interlayer charge transfer.

In marginally twisted AP-WSe$_2$ bilayers ($\theta_{AP} \lesssim 1.0°$) the conduction and valence band edges form arrays of quantum dots for K- and $-K$-valley electrons and holes, respectively, formed by reconstruction-induced piezopotentials. Each quantum dot hosts localized states labeled by orbital momentum, that develop into flat moiré minibands upon account of the weak coupling between neighboring quantum dots, giving way to ordinary parabolic bands at larger twist angles ($1.0° \lesssim \theta_{AP} \lesssim 2°$).

Here, we note that prevalence of a K-point band edge over Γ-valley states results from DFT calculations carried out for suspended samples. However, hBN encapsulation of the WSe$_2$ bilayers may influence the order of the Γ- and K-point state energies in the valence band. This is because Γ-valley states, formed by metal d_{z^2} and chalcogen p_z orbitals, will experience stronger hybridization (repulsion) with hBN states, as compared to K-valley states, which consist of metal $d_{(x\pm iy)^2}$ orbitals.

For marginally twisted P-WSe$_2$ bilayers we found that the K-point conduction and valence band edges and the Γ-point valence band edge lie in triangular domains with MX$'$ and XM$'$ registries, at extrema of the total piezo- and ferroelectric potentials, with the global valence band maximum located at the K point. These large domains are physical realizations of WSe$_2$ bilayers belonging to the 3R polytype that lack inversion symmetry, giving rise to weak ferroelectricity [23].

As the MX$'$ and XM$'$ domains contract for increasing twist angles, the band-edge states become laterally confined, forming a hexagonal lattice of localized states. The two sublattices, located at opposite layers, hybridize through interlayer tunneling and form two distinct gapped graphene-like superlattices: one for the valence- and another for the conduction band edge.

Moreover, we have demonstrated the opportunity to control the indirect-to-direct band gap transition in 2H- and MX$'$/XM$'$-stacked WSe$_2$ bilayers via external stimuli such as uniform strain, pressure and out-of-plane electric field.

APPENDIX A: GENERAL APPROACH FOR DESCRIBING HYBRIDIZATION IN WSe$_2$ BILAYERS

To derive an effective Hamiltonian describing interlayer hybridization in twisted TMD homobilayers we first consider coupling between states of two aligned monolayers having a lateral shift $\boldsymbol{r}_0$ between their lattices (i.e., $\boldsymbol{R}_i^t = \boldsymbol{r}_0 + \boldsymbol{R}_i^b$, with

i the unit cell index of a single monolayer) and assume that the bilayer crystal potential can be represented as a sum of those of constituent monolayers, $V_t(\mathbf{r}, z) + V_b(\mathbf{r}, z)$ (hereafter, indices t and b label the top and bottom layers). In such a system, the electronic states satisfy the following equation:

$$\left[\frac{\hat{\mathbf{p}}^2}{2m_0} + \left(V_t(\mathbf{r}, z) + \frac{E_0}{2} \right) + \left(V_b(\mathbf{r}, z) + \frac{E_0}{2} \right) \right] \Psi = E\Psi,$$

(A1)

where $\hat{\mathbf{p}} = -i\hbar(\nabla_{\mathbf{r}}, \partial_z)$ is the 3D momentum operator (z-axis is along normal to layers), m_0 is the free electron mass, and $E_0/2$ is a reference point for the potentials that we explicitly take into account to preserve gauge invariance of the equations derived below. As hybridization of states in different parts of the Brillouin zone (valleys centered at the Γ or $\mathcal{K}$ points) can be described independently, for each of the valleys we will use basis of Kohn-Luttinger functions [79] to expand an arbitrary state Ψ:

$$\Psi = \sum_{n_t, \mathbf{k}} C_{\mathbf{k}, n_t} |\mathbf{k}, n_t\rangle + \sum_{n_b, \mathbf{k}} C_{\mathbf{k}, n_b} |\mathbf{k}, n_b\rangle. \quad (A2)$$

Here, $|\mathbf{k}, n_{t/b}\rangle = e^{i\mathbf{k}\mathbf{r}} \psi_{\mathcal{K}, n_{t,b}}(\mathbf{r})$ and $\psi_{\mathcal{K}, n_{t/b}}$ are Bloch eigenfunctions of the $n_{t/b}$-th band at the $\mathcal{K}$ point of the TMD monolayer Brillouin zone (below we consider $\mathcal{K} = \Gamma$ in Appendix B and $\mathcal{K} = K$ in Appendix C), and $\mathbf{k}$ is the 2D wave vector measured from the given $\mathcal{K}$ point. The basis choice of Eq. (A2) implies that the top layer crystal potential can be treated as a perturbation for bottom-layer states, and vice versa.

Substituting the wave function Eq. (A2) into Eq. (A1) we obtain a matrix equation for the column vector of expansion coefficients C:

$$\hat{H}_0 C = (E - E_0)(\hat{1} + \hat{T})C. \quad (A3)$$

Here, $\hat{1}$ is the unit matrix, and $\hat{T}$ is a matrix whose elements are given by the overlap intergrals between basis functions Eq. (A2) of different layers, which are nonorthogonal. Note that, by definition, all diagonal elements of $\hat{T}$ are equal to zero. The intralayer matrix elements of $\hat{H}_0$ read

$$\langle \mathbf{k}, n_{t/b} | H_0 | \mathbf{k}', n'_{t/b} \rangle$$

$$\equiv \langle \mathbf{k}, n_{t/b} | \frac{\hat{\mathbf{p}}^2}{2m_0} + V_t + V_b | \mathbf{k}', n'_{t/b} \rangle$$

$$= \varepsilon_{n_{t/b}}(\mathbf{k}) \delta_{\mathbf{k}, \mathbf{k}'} \delta_{n_{t/b}, n'_{t/b}} + \langle \mathbf{k}, n_{t/b} | V_{b/t} | \mathbf{k}', n'_{t/b} \rangle$$

$$\cong \varepsilon_{n_{t/b}}(\mathbf{k}) \delta_{\mathbf{k}, \mathbf{k}'} \delta_{n_{t/b}, n'_{t/b}} + \langle \mathbf{k}, n_{t/b} | V_{b/t} | \mathbf{k}', n_{t/b} \rangle, \quad (A4)$$

where $\varepsilon_{n_{t/b}}(\mathbf{k})$ is the $n_{t/b}$-th band state energy in the top/bottom monolayer, measured from the vacuum level for $V_{t/b}$, i.e., $E_0/2$. For the interlayer matrix elements of $\hat{H}_0$ we have

$$\langle \mathbf{k}, n_t | H_0 | \mathbf{k}', n_b \rangle$$

$$= \langle \mathbf{k}, n_t | \frac{\hat{\mathbf{p}}^2}{2m_0} + V_t + \frac{\hat{\mathbf{p}}^2}{2m_0} + V_b - \frac{\hat{\mathbf{p}}^2}{2m_0} | \mathbf{k}', n_b \rangle$$

$$= \delta_{\mathbf{k}, \mathbf{k}'} [\varepsilon_{n_b}(\mathbf{k}) + \varepsilon_{n_t}(\mathbf{k})] \langle \mathbf{k}, n_t | \hat{T} | \mathbf{k}, n_b \rangle$$

$$\quad - \delta_{\mathbf{k}, \mathbf{k}'} \langle \mathbf{k}, n_t | \frac{\hat{\mathbf{p}}^2}{2m_0} | \mathbf{k}, n_b \rangle. \quad (A5)$$

Note that conservation of crystal momentum in Eqs. (A4) and (A5) results from the alignment of constituent monolayers. The transformation $\widetilde{C} = \sqrt{\hat{1} + \hat{T}} C$ eliminates off diagonal elements in the normalization condition for the column vector $\widetilde{C}$ (i.e., $\widetilde{C}^\dagger \widetilde{C} = 1$), and allows us to rewrite Eq. (A3) in standard form with a new Hamiltonian matrix:

$$\frac{1}{\sqrt{\hat{1} + \hat{T}}} \hat{H}_0 \frac{1}{\sqrt{\hat{1} + \hat{T}}} \widetilde{C} = (E - E_0)\widetilde{C}. \quad (A6)$$

Below, we exclude the reference energy of the crystal potentials in Eq. (A6) by the energy shift $E - E_0 \rightarrow E$. Since the matrix elements of $\hat{T}$ are much smaller than unity, we expand $1/\sqrt{\hat{1} + \hat{T}}$ in the previous equation up to second order in $\hat{T}$, and obtain the following equation:

$$\sum_{\mathbf{k}'} \langle \mathbf{k}, n_{t/b} | \hat{H}_0 - \frac{1}{2} \{ \hat{T}, \hat{H}_0 \} | \mathbf{k}', n_{t/b} \rangle \widetilde{C}_{\mathbf{k}', n_{t/b}}$$

$$+ \sum_{\mathbf{k}', n_{b/t}} \langle \mathbf{k}, n_{t/b} | \hat{H}_0 - \frac{1}{2} \{ \hat{T}, \hat{H}_0 \} | \mathbf{k}', n_{b/t} \rangle \widetilde{C}_{\mathbf{k}', n_{b/t}}$$

$$+ \sum_{\mathbf{k}'} \langle \mathbf{k}, n_{t/b} | \frac{3}{8} \{ \hat{T}^2, \hat{H}_0 \} + \frac{1}{4} \hat{T} \hat{H}_0 \hat{T} | \mathbf{k}', n_{t/b} \rangle \widetilde{C}_{\mathbf{k}', n_{t/b}}$$

$$= E \widetilde{C}_{\mathbf{k}, n_{t/b}}, \quad (A7)$$

where $\{\hat{A}, \hat{B}\} = \hat{A}\hat{B} + \hat{B}\hat{A}$ is the anticommutator of operators $\hat{A}$ and $\hat{B}$. Equation (A7) is the final result of this section, which we will exploit in the following sections to derive effective Hamiltonians describing hybridization of top valence band states in Γ, as well as top valence and bottom conduction states at the K points of two aligned monolayers.

APPENDIX B: HYBRIDIZATION OF TOP VALENCE BAND STATES IN Γ POINT

Let us consider the top valence band states at the Γ point of TMD monolayers, with energy $\varepsilon_{A'}$ and formed mostly by d_{z^2} orbitals of metals [32]. As this state transforms according to the one-dimensional A' representation of group D_{3h} (see Table VI), the minimal model that describes the splitting of the states in bilayers comprises only terms with $\widetilde{C}_{A'_{t/b}}$ in Eq. (A7), which would lead to a 2×2 effective Hamiltonian. However, interlayer coupling affects not only the splitting of the A'-states, but also changes the average energy of the split states, due to their hybridization with other bands. To take into account the latter effect, we add to our model one more band in each layer, which is the closest in energy to the top

TABLE VI. Character table for the relevant representations of point group D_{3h}.

	E	$2C_3$	$3C_2$	σ_h	$2S_3$	$3\sigma_v$
A'	1	1	1	1	1	1
A''	1	1	-1	1	1	-1

valence band in monolayers and composed of selenium p_z orbitals. These bands transform according to representation A'', and have energy $\varepsilon_{A''}$. Therefore, in a minimal effective Hamiltonian describing hybridization of the top valence band states in Γ point we leave only the two bands in each layer, so that system of Eqs. (A7) is reduced to

$$
\begin{pmatrix}
\varepsilon_{A'} + \Phi^{A'_t}(\boldsymbol{r}_0) - E & T^{A'_t,A'_b}(\boldsymbol{r}_0) & 0 & T^{A'_t,A''_b}(\boldsymbol{r}_0) \\
T^{A'_t,A'_b}(\boldsymbol{r}_0) & \varepsilon_{A'} + \Phi^{A'_b}(\boldsymbol{r}_0) - E & T^{A'_b,A''_t}(-\boldsymbol{r}_0) & 0 \\
0 & T^{A'_b,A''_t}(-\boldsymbol{r}_0) & \varepsilon_{A''} + \Phi^{A''_t}(\boldsymbol{r}_0) - E & T^{A''_t,A''_b}(\boldsymbol{r}_0) \\
T^{A'_t,A''_b}(\boldsymbol{r}_0) & 0 & T^{A''_t,A''_b}(\boldsymbol{r}_0) & \varepsilon_{A''} + \Phi^{A''_b}(\boldsymbol{r}_0) - E
\end{pmatrix}
\begin{pmatrix}
\widetilde{C}_{A'_t} \\
\widetilde{C}_{A'_b} \\
\widetilde{C}_{A''_t} \\
\widetilde{C}_{A''_b}
\end{pmatrix} = 0,
\tag{B1}
$$

where $T^{A'_t,A'_b}(\boldsymbol{r}_0)$, $T^{A''_t,A''_b}(\boldsymbol{r}_0)$, $T^{A'_t,A''_b}(\boldsymbol{r}_0)$, and $\Phi^{A'_{t/b}}(\boldsymbol{r}_0)$, $\Phi^{A''_{t/b}}(\boldsymbol{r}_0)$ are the overlap integrals characterizing the first- and second-order scattering processes, respectively, between corresponding Bloch amplitudes $u_{\Gamma,A'_{t/b}}(\boldsymbol{r}, z)$, $u_{\Gamma,A''_{t/b}}(\boldsymbol{r}, z)$, implicitly depending on interlayer distance d. To find explicit $\boldsymbol{r}_0$-dependencies for terms in Eq. (B1), we approximate the Bloch amplitudes by the lowest harmonics in their Fourier series in monolayer reciprocal vectors $\boldsymbol{G}_j$ (same for two aligned layers):

$$
u_{A'_t/A''_t}(\boldsymbol{r}, z) \approx u^{(0)}_{A'_t/A''_t}(z) + \sum_{j=1,2,3} \left[u^{(1)}_{A'_t/A''_t}(z) e^{i\boldsymbol{G}_j \cdot (\boldsymbol{r}-\boldsymbol{r}_0)} + \text{c.c.} \right],
\tag{B2}
$$

$$
u_{A'_b/A''_b}(\boldsymbol{r}, z) \approx u^{(0)}_{A'_b/A''_b}(z) + \sum_{j=1,2,3} \left[u^{(1)}_{A'_b/A''_b}(z) e^{i\boldsymbol{G}_j \cdot \boldsymbol{r}} + \text{c.c.} \right].
\tag{B3}
$$

In this approximation, the resonant tunneling between A' or A'' bands reads

$$
T^{A_t,A_b}(\boldsymbol{r}_0) = t^{(0)}_{A_t A_b} \varepsilon_A - \frac{\hbar^2 (k_{z0}^2)_{A_t A_b}}{2m_0} + 2\left| t^{(1)}_{A_t A_b} \right| \left(\varepsilon_A - \frac{\hbar^2 G^2}{2m_0} \right) \sum_{j=1,2,3} \cos(\boldsymbol{G}_j \cdot \boldsymbol{r}_0 + \varphi_{A_t A_b}) - 2\frac{\hbar^2 \left| (k_{z1}^2)_{A_t A_b} \right|}{2m_0}
$$
$$
\times \sum_{j=1,2,3} \cos(\boldsymbol{G}_j \cdot \boldsymbol{r}_0 + \widetilde{\varphi}_{A_t A_b}),
\tag{B4}
$$

where

$$
t^{(0)}_{A_t,A_b} = \int dz\, u^{(0)}_{A_t} u^{(0)}_{A_b}, \quad \left\| t^{(1)}_{A_t,A_b} \right| e^{i\varphi_{A_t A_b}} = \int dz\, u^{(1)*}_{A_t} u^{(1)}_{A_b},
\tag{B5}
$$

$$
(k_{z0}^2)_{A_t,A_b} = \int dz \left(\partial_z u^{(0)}_{A_t} \right) \left(\partial_z u^{(0)}_{A_b} \right),
\tag{B6}
$$

$$
\left| (k_{z1}^2)_{A_t,A_b} \right| e^{i\widetilde{\varphi}_{A_t A_b}} = \int dz \left(\partial_z u^{(1)*}_{A_t} \right) \left(\partial_z u^{(1)}_{A_b} \right),
\tag{B7}
$$

are overlap integrals implicitly depending on interlayer distance (A labels either A' or A'' band). In Eqs. (B2) and (B3) we use the fact that states with zero crystal momentum (Γ-point states) can be represented by a real-valued wave function leading to real values for $t^{(0)}_{A_t A_b}$ and $(k_{z0}^2)_{A_t,A_b}$. For P bilayers, Eq. (B4) can be simplified due to σ_h mirror symmetry in each monolayer. Indeed, as states in monolayers are either even or odd with respect to σ_h, one has relation $\int dz u^{(1)*}_{A'_t}(z) u^{(1)}_{A'_b}(z) = \int dz u^{(1)*}_{A'_t}(-z) u^{(1)}_{A'_b}(-z) = \int dz u^{(1)*}_{A'_b}(z) u^{(1)}_{A'_t}(z)$, leading to $\varphi_{A_t A_b} = 0$. Similarly, $\widetilde{\varphi}_{A_t A_b} = 0$. Thus, for P orientation, the matrix elements describing resonant tunneling in Eq. (B1) are even functions of $\boldsymbol{r}_0$, $T^{A'_t,A'_b}(\boldsymbol{r}_0) = T^{A'_t,A'_b}(-\boldsymbol{r}_0)$. By contrast, for AP-WSe$_2$ bilayers the phases of $u^{(1)}_{A'_t}(z)$ and $u^{(1)}_{A'_b}(z)$ are not equal to each other, allowing nonzero $\varphi_{A_t A_b}$ and $\widetilde{\varphi}_{A_t A_b}$ in Eq. (B4).

The off-resonant interlayer coupling term is expressed as follows:

$$
T^{A'_t,A''_b}(\boldsymbol{r}_0) = t^{(0)}_{A'_t A''_b} \frac{\varepsilon_{A'} + \varepsilon_{A''}}{2} - \frac{\hbar^2 (k_{z0}^2)_{A'_t A''_b}}{2m_0} + 2\left| t^{(1)}_{A'_t A''_b} \right| \left(\frac{\varepsilon_{A'} + \varepsilon_{A''}}{2} - \frac{\hbar^2 G^2}{2m_0} \right) \sum_{j=1,2,3} \cos\left(\boldsymbol{G}_j \cdot \boldsymbol{r}_0 + \varphi_{A'_t A''_b} \right)
$$
$$
- 2\frac{\hbar^2 \left| (k_{z1}^2)_{A'_t A''_b} \right|}{2m_0} \sum_{j=1,2,3} \cos\left(\boldsymbol{G}_j \cdot \boldsymbol{r}_0 + \widetilde{\varphi}_{A'_t A''_b} \right),
\tag{B8}
$$

where

$$
t^{(0)}_{A'_t,A''_b} = \int dz\, u^{(0)}_{A'_t} u^{(0)}_{A''_b}, \quad \left\| t^{(1)}_{A'_t A''_b} \right| e^{i\varphi_{A'_t A''_b}} = \int dz\, u^{(1)*}_{A'_t} u^{(1)}_{A''_b},
\tag{B9}
$$

$$
(k_{z0}^2)_{A'_t,A''_b} = \int dz \left(\partial_z u^{(0)}_{A'_t} \right) \left(\partial_z u^{(0)}_{A''_b} \right), \quad \left\| (k_{z1}^2)_{A'_t,A''_b} \right| e^{i\widetilde{\varphi}_{A'_t A''_b}} = \int dz \left(\partial_z u^{(1)*}_{A'_t} \right) \left(\partial_z u^{(1)}_{A''_b} \right)
\tag{B10}
$$

are interband-interlayer overlap integrals. For P bilayers, σ_h symmetry relates the off-resonant interlayer matrix elements

$$T^{A'_t,A''_b}(\boldsymbol{r}_0) = -T^{A'_b,A''_t}(-\boldsymbol{r}_0). \tag{B11}$$

The second-order contribution to the diagonal elements of Eq. (B1) for A' states is expressed as

$$
\begin{aligned}
\Phi^{A'_t}(\boldsymbol{r}_0) = &-\varepsilon_{A'}\left[t^{(0)}_{A'_t A'_b} + 2\big|t^{(1)}_{A'_t A'_b}\big| \sum_{j=1}^{3}\cos\left(\boldsymbol{G}_j\cdot\boldsymbol{r}_0 + \varphi_{A'_t A'_b}\right)\right]^2 + \widetilde{V}^{(0)}_b + 4\big|\widetilde{V}^{(1)}_b\big|\sum_{j=1}^{3}\cos\left(\boldsymbol{G}_j\cdot\boldsymbol{r}_0 + \varphi_{V_b}\right) \\
&+\left[t^{(0)}_{A'_t A'_b} + 2\big|t^{(1)}_{A'_t A'_b}\big|\sum_{j=1}^{3}\cos\left(\boldsymbol{G}_j\cdot\boldsymbol{r}_0 + \varphi_{A'_t A'_b}\right)\right]\left[\frac{\hbar^2\big(k^2_{z0}\big)_{A'_t,A'_b}}{2m_0} + 2\frac{\hbar^2\big|\big(k^2_{z1}\big)_{A'_t,A'_b}\big|}{2m_0}\sum_{j=1}^{3}\cos\left(\boldsymbol{G}_j\cdot\boldsymbol{r}_0 + \widetilde{\varphi}_{A'_t A'_b}\right)\right] \\
&-\frac{1}{4}(\varepsilon_{A'} + 3\varepsilon_{A''})\left[t^{(0)}_{A'_t A''_b} + 2\big|t^{(1)}_{A'_t A''_b}\big|\sum_{j=1}^{3}\cos\left(\boldsymbol{G}_j\cdot\boldsymbol{r}_0 + \varphi_{A'_t A''_b}\right)\right]^2 + \left[t^{(0)}_{A'_t A''_b} + 2\big|t^{(1)}_{A'_t A''_b}\big|\sum_{j=1}^{3}\cos\left(\boldsymbol{G}_j\cdot\boldsymbol{r}_0 + \varphi_{A'_t A''_b}\right)\right] \\
&\times\left[\frac{\hbar^2\big(k^2_{z0}\big)_{A'_t,A''_b}}{2m_0} + 2\frac{\hbar^2\big|\big(k^2_{z1}\big)_{A'_t,A''_b}\big|}{2m_0}\sum_{j=1}^{3}\cos\left(\boldsymbol{G}_j\cdot\boldsymbol{r}_0 + \widetilde{\varphi}_{A'_t A''_b}\right)\right], \tag{B12}
\end{aligned}
$$

$$
\begin{aligned}
\Phi^{A'_b}(\boldsymbol{r}_0) = &-\varepsilon_{A'}\left[t^{(0)}_{A'_t A'_b} + 2\big|t^{(1)}_{A'_t A'_b}\big|\sum_{j=1}^{3}\cos\left(\boldsymbol{G}_j\cdot\boldsymbol{r}_0 + \varphi_{A'_t A'_b}\right)\right]^2 + \widetilde{V}^{(0)}_t + 4\big|\widetilde{V}^{(1)}_t\big|\sum_{j=1,2,3}\cos\left(\boldsymbol{G}_j\cdot\boldsymbol{r}_0 - \varphi_{V_t}\right) \\
&+\left[t^{(0)}_{A'_t A'_b} + 2\big|t^{(1)}_{A'_t A'_b}\big|\sum_{j=1}^{3}\cos\left(\boldsymbol{G}_j\cdot\boldsymbol{r}_0 + \varphi_{A'_t A'_b}\right)\right]\left[\frac{\hbar^2\big(k^2_{z0}\big)_{A'_t,A'_b}}{2m_0} + 2\frac{\hbar^2\big|\big(k^2_{z1}\big)_{A'_t,A'_b}\big|}{2m_0}\sum_{j=1,2,3}\cos\left(\boldsymbol{G}_j\cdot\boldsymbol{r}_0 + \widetilde{\varphi}_{A'_t A'_b}\right)\right] \\
&-\frac{1}{4}(\varepsilon_{A'} + 3\varepsilon_{A''})\left[t^{(0)}_{A'_t A''_b} + 2\big|t^{(1)}_{A'_t A''_b}\big|\sum_{j=1,2,3}\cos\left(\boldsymbol{G}_j\cdot\boldsymbol{r}_0 - \varphi_{A'_t A''_b}\right)\right]^2 + \left[t^{(0)}_{A'_t A''_b} + 2\big|t^{(1)}_{A'_t A''_b}\big|\sum_{j=1}^{3}\cos\left(\boldsymbol{G}_j\cdot\boldsymbol{r}_0 - \varphi_{A'_t A''_b}\right)\right] \\
&\times\left[\frac{\hbar^2\big(k^2_{z0}\big)_{A'_t,A''_b}}{2m_0} + 2\frac{\hbar^2\big|\big(k^2_{z1}\big)_{A'_t,A''_b}\big|}{2m_0}\sum_{j=1,2,3}\cos\left(\boldsymbol{G}_j\cdot\boldsymbol{r}_0 - \widetilde{\varphi}_{A'_t A''_b}\right)\right], \tag{B13}
\end{aligned}
$$

where $\widetilde{V}^{(0)}_{t/b} = \int V^{(0)}_{t/b}[(u^{(0)}_{A'_{b/t}})^2 + 2u^{(1)}_{A'_{b/t}}u^{(1)*}_{A'_{b/t}}]$, $|\widetilde{V}^{(1)}_{t/b}|e^{i\varphi_{V_{t/b}}} = \int V^{(1)}_{t/b}(u^{(1)}_{A'_{b/t}})^2$, and we exploited the lowest harmonics of the Fourier series for the monolayer potentials

$$V_t(\boldsymbol{r}, z) = V^{(0)}_t + \sum_{j=1}^{3}\big\{V^{(1)}_t e^{i\boldsymbol{G}_j(\boldsymbol{r}-\boldsymbol{r}_0)} + \text{c.c.}\big\}, \quad V_b(\boldsymbol{r}, z) = V^{(0)}_t + \sum_{j=1}^{3}\big\{V^{(1)}_t e^{i\boldsymbol{G}_j\boldsymbol{r}} + \text{c.c.}\big\}. \tag{B14}$$

For A'' subbands, the terms $\Phi^{A''_{t/b}}_{\boldsymbol{k},\boldsymbol{G}}(\boldsymbol{r}_0)$ can be obtained from Eqs. (B12) and (B13) by exchanging $A' \leftrightarrow A''$ in all terms.

Having established the explicit form for the matrix elements of Hamiltonian Eq. (B1), we now exclude all but the lowest-energy A'' states to obtain a minimal effective Hamiltonian describing hybridization of top valence states at the Γ point:

$$
\begin{pmatrix}
\varepsilon_{A'} + \Phi^{A'_t}(\boldsymbol{r}_0) + \frac{[T^{A'_t,A''_b}(\boldsymbol{r}_0)]^2}{\varepsilon_{A'}-\varepsilon_{A''}} - E & T^{A'_t,A'_b}(\boldsymbol{r}_0) \\
T^{A'_t,A'_b}(\boldsymbol{r}_0) & \varepsilon_{A'} + \Phi^{A'_b}(\boldsymbol{r}_0) + \frac{[T^{A'_b,A''_t}(-\boldsymbol{r}_0)]^2}{\varepsilon_{A'}-\varepsilon_{A''}} - E
\end{pmatrix}
\begin{pmatrix}
\widetilde{C}_{A'_t} \\
\widetilde{C}_{A'_b}
\end{pmatrix} = 0. \tag{B15}
$$

The Hamiltonian Eq. (B15) comprises quite a few microscopic parameters that are impossible to extract independently using DFT-computed band structures for aligned P and AP bilayers. Therefore, below we will keep only its structure using a simplified expression

$$H^{P/AP}_\Gamma + \delta H^{P/AP}_\Gamma = \begin{pmatrix} \varepsilon^{P/AP}_\Gamma - \frac{S^{P/AP}_\Gamma}{2} & T^{P/AP}_\Gamma \\ T^{P/AP}_\Gamma & \varepsilon^{P/AP}_\Gamma + \frac{S^{P/AP}_\Gamma}{2} \end{pmatrix} + \begin{pmatrix} \delta\varepsilon^{P/AP}_\Gamma & \delta T^{P/AP}_\Gamma \\ \delta T^{P/AP}_\Gamma & \delta\varepsilon^{P/AP}_\Gamma \end{pmatrix}, \tag{B16}$$

with matrix elements defined in Eqs. (5) and (9) of the main text. To quantify the parameters in the model Eq. (B16), we calculate the band energies within the framework of DFT for several lateral offsets identified in Fig. 26, and multiple interlayer distances between the adhesion energy minima of

the lowest and highest configurations (see Fig. 2). To fit the interlayer distance dependencies of T_Γ, δT_Γ ε_Γ, $\delta\varepsilon_\Gamma$ and $S^{P/AP}_\Gamma$, we calculate the mean, $(E^{P/AP}_+ + E^{P/AP}_-)/2$, and the difference, $(E^{P/AP}_+ - E^{P/AP}_-)$, of the energy eigenvalues of Hamiltonian
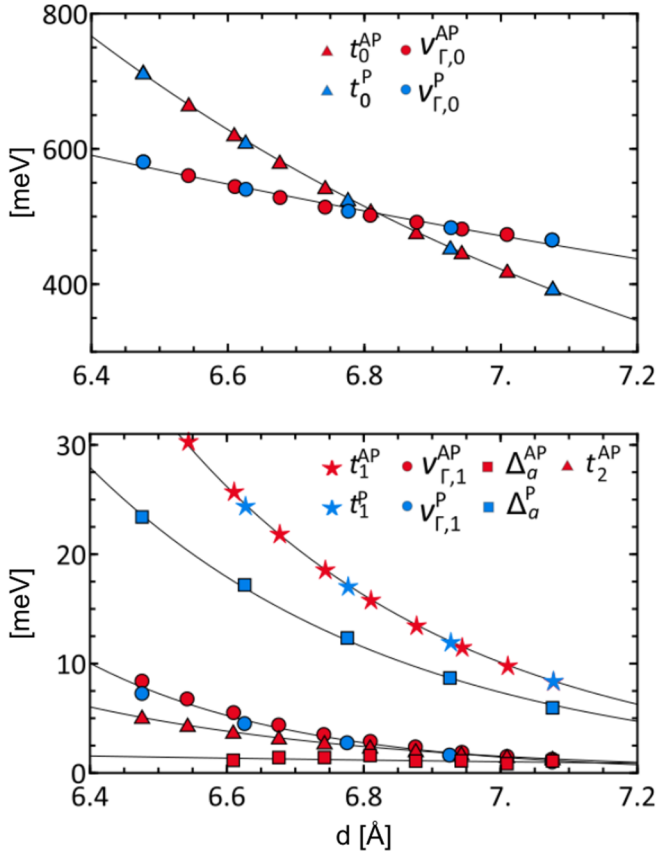
FIG. 21. z dependencies for $v_{\Gamma;0,1}^{P/AP}$, $t_{0,1}^{P/AP}$, t_2^{AP}, and $\Delta_a^{P/AP}$ extracted from DFT. Top panel shows that $v_{\Gamma,0}^{AP} = v_{\Gamma,0}^{P}$, $t_0^{AP} = t_0^{P}$. Bottom panel demonstrates validity of the following relations: $v_{\Gamma,1}^{AP} = v_{\Gamma,1}^{P}$, $t_1^{AP} = t_1^{P}$, and $\Delta_a^{AP} = 0$. $H_\Gamma^{P/AP}$, consisting of the greatest terms with $t_{0,1}^{P/AP}$, $v_{\Gamma,0}$ and $\Delta_a^{P/AP}$, determines major effects in the hybridization model Eq. (B16), while the other terms $v_{\Gamma,1}^{P/AP}$, $t_2^{P/AP}$, gathered in $\delta H_\Gamma^{P/AP}$, result in no more than $\approx 10\%$ amendments (compare dashed and solid lines in Figs. 22 and 23).

Eq. (B16),

$$E_{\pm}^{P/AP}(\boldsymbol{r}_0, z) = \varepsilon_\Gamma^{P/AP}(\boldsymbol{r}_0, z)$$
$$\pm \sqrt{\left(T_\Gamma^{P/AP}(\boldsymbol{r}_0, z)\right)^2 + \left(\frac{S_\Gamma^{P/AP}(\boldsymbol{r}_0, z)}{2}\right)^2}.$$
(B17)

The analysis of the z dependencies of different terms in the matrix elements of Eq. (B16) (see Fig. 21) allows us to fit them by exponential functions, with the parameters given in Table II, and leads to the following relations: $v_{\Gamma,0}^{P} = v_{\Gamma,0}^{AP}$, $v_{\Gamma,1}^{P} = v_{\Gamma,1}^{AP}$, $t_0^{P} = t_0^{AP}$, $t_1^{P} = t_1^{AP}$, and $S_\Gamma^{AP} = \Delta_a^{AP} f_a(\boldsymbol{r}_0) = 0$. Moreover, since the values of $t_{0,1}^{P/AP}$ and $v_{\Gamma,0}$ in $H_\Gamma^{P/AP}$ are much larger than the others gathered in $\delta H_\Gamma^{P/AP}$, the latter can be used as a perturbation to the former, which characterizes the main features of the hybridization model at the Γ point. In Figs. 22 and 23 we compare the DFT-computed (triangles) energies for splitting, average and individual energies of the hybridized A'-states in WSe$_2$ bilayers with those calculated

FIG. 22. DFT-computed values (triangles) for splitting, average, and individual energies of the two top-most valence band states in Γ point of AP-WSe$_2$ bilayers along the stacking configuration path in Fig. 26(b) vs. corresponding values obtained with $H_\Gamma^{AP} + \delta H_\Gamma^{AP}$ (solid) and H_Γ^{AP} (dashed). Dotted straight lines show results for the energies calculated with H_Γ^{AP} at $t_1^{AP} = 0$, (i.e., with account of only the largest interlayer-distance-dependent terms), emphasizing major role of interlayer distance variation on position of band edge in Γ point of the bilayers.

with the help of H_Γ (dashed) and $H_\Gamma^{P/AP} + \delta H_\Gamma^{P/AP}$ (solid). The figures demonstrate that the Γ-point state energy for the top valence band is mainly determined by the optimal interlayer distances of corresponding stacking configurations rather than r_0-dependencies of matrix elements at a fixed distance.

$$H_K^{\tau,s} = \begin{pmatrix} \varepsilon_{E'} + \varepsilon_{E',\mathrm{AP}}^{\tau,s} & T_{E',E'} & 0 & T_{E'',E'} & 0 & T_{A',E'} \\ T_{E',E'}^* & \varepsilon_{E'} - \varepsilon_{E',\mathrm{AP}}^{\tau,s} & T_{E',E''}^* & 0 & T_{E',A'}^* & 0 \\ 0 & T_{E',E''} & \varepsilon_{E''} + \varepsilon_{E'',\mathrm{AP}}^{\tau,s} & T_{E'',E''} & 0 & T_{A',E''} \\ T_{E'',E'}^* & 0 & T_{E'',E''}^* & \varepsilon_{E''} - \varepsilon_{E'',\mathrm{AP}}^{\tau,s} & T_{E'',A'}^* & 0 \\ 0 & T_{E',A'} & 0 & T_{E'',A'} & \varepsilon_{A'} + \varepsilon_{A',\mathrm{AP}}^{\tau,s} & T_{A',A'} \\ T_{A',E'}^* & 0 & T_{A',E''}^* & 0 & T_{A',A'}^* & \varepsilon_{A'} - \varepsilon_{A',\mathrm{AP}}^{\tau,s} \end{pmatrix}, \quad (C1)$$

for bands VB(K), VB-1(K), and VB-2(K) of the top and bottom layers, which transform like the irreducible representations E', E'', and A' of group C_{3h}, respectively (Table VII).

Here, we consider only interlayer hybridization terms ($\alpha = E', E'', A'$)

$$T_{\alpha_t,\alpha_b} = \langle \tau_t \mathbf{K}_t, \alpha_t | \left[(\varepsilon_{\alpha_b} + \varepsilon_{\alpha_t})\hat{T} - \frac{\hat{\mathbf{p}}^2}{2m_0} \right] | \tau_b \mathbf{K}_b, \alpha_b \rangle, \quad (C2)$$

up to first order in the interlayer overlap integrals, and ignore the potential scattering terms appearing in Eq. (A4). For P type bilayers the same-band spin-s levels in both layers coincide; for AP structures these levels are separated by the band's spin-orbit splitting. This is the origin of the terms

$$\varepsilon_{\alpha,\mathrm{AP}}^{\tau,s} = \begin{cases} 0, & \text{P stacking,} \\ \tau s \frac{\Delta_\alpha^{\mathrm{SO}}}{2}, & \text{AP stacking,} \end{cases} \quad (C3)$$

in Eq. (C1).

1. P stacking

Next, we do a Löwdin transformation to project out bands VB-1(K) and VB-2(K) of both layers up to second order in perturbation theory, keeping only the necessary second order terms to correctly fit the band splittings at the K point predicted by DFT calculations. In the case of P stacking, this means ignoring the VB-2(K) band altogether. Due to spin-valley locking in TMDs, the band edge at valley τ belongs to the spin $s = -\tau$ band, described by the Hamiltonian

$$H_{P,K}^\tau = \begin{pmatrix} \varepsilon_{\mathrm{VB}}^P(\mathbf{r}_0) - \frac{\Delta^P(\mathbf{r}_0)}{2} & T_{\mathrm{VB}}^P(\mathbf{r}_0) \\ T_{\mathrm{VB}}^{P*}(\mathbf{r}_0) & \varepsilon_{\mathrm{VB}}^P(\mathbf{r}_0) + \frac{\Delta^P(\mathbf{r}_0)}{2} \end{pmatrix}, \quad (C4)$$

TABLE VII. Character table for the point group C_{3h}, describing the symmetry of the K-point bands. Here, $\varepsilon = e^{i2\pi/3}$.

	E	$2C_3$	σ_h	$2S_3$
A'	1	1	1	1
A''	1	1	-1	-1
E'	1	ε	1	ε
	1	ε^*	1	ε^*
E''	1	ε	1	ε
	1	ε^*	1	ε^*

APPENDIX C: DERIVATION OF THE K-POINT HYBRIDIZATION HAMILTONIANS

Applying the formalism of Appendix A to the valence-band states of spin projection s at the τK point, we may write the effective three-band Hamiltonian

where we have abbreviated $T_{\mathrm{VB}} \equiv T_{E',E'}$ and defined

$$\varepsilon_{\mathrm{VB}}^P(\mathbf{r}_0) = \varepsilon_{E'} + \frac{|T_{E'',E'}^P(\mathbf{r}_0)|^2 + |T_{E',E''}^P(\mathbf{r}_0)|^2}{4(\varepsilon_{E'} - \varepsilon_{E''})},$$

$$\Delta^P(\mathbf{r}_0) = \frac{|T_{E'',E'}^P(\mathbf{r}_0)|^2 - |T_{E',E''}^P(\mathbf{r}_0)|^2}{2(\varepsilon_{E'} - \varepsilon_{E''})}. \quad (C5)$$

Note that on symmetry grounds we have obtained an interlayer splitting term, which we shall use to account for the interlayer bias $\Delta_P(\mathbf{r}_0)$ found in our *ab initio* calculations.

The hopping matrix elements $T_{\alpha,\beta}^P$ between bottom-layer band β and top-layer band α are obtained by Fourier expanding the corresponding Bloch functions at momentum $\tau \mathbf{K}$ in the in-plane coordinates, and keeping only those Bragg vectors $\mathbf{G}$ such that $\tau \mathbf{K} + \mathbf{G} = \tau C_3^\mu \mathbf{K}$, with $\mu = 1, 2$. This approximation gives

$$T_{\alpha,\beta}(\mathbf{r}_0) = \sum_{\mu=0}^{2} e^{i\tau C_3^\mu \mathbf{K} \cdot \mathbf{r}_0} t_{\alpha,\beta}(\tau C_3^\mu \mathbf{K}), \quad (C6)$$

where $t_{\alpha,\beta}(\mathbf{q})$ has the form

$$t_{\alpha,\beta}(\mathbf{q}) = t_{\alpha,\beta}^{(1)} \int dz\, u_{\alpha,t}^*(\mathbf{q}, z) u_{\beta,b}(\mathbf{q}, z)$$

$$+ t_{\alpha,\beta}^{(2)} \int dz\, \partial_z u_{\alpha,t}^*(\mathbf{q}, z) \partial_z u_{\beta,b}(\mathbf{q}, z). \quad (C7)$$

To relate the three coefficients $t_{\alpha,\beta}(\tau C_3^\mu \mathbf{K})$ in Eq. (C6), we use the following symmetry property of the Bloch functions at the $\tau \mathbf{K}$ point and of their Fourier coefficients:

$$u_{\alpha,t/b}(\tau C_3 \mathbf{K}) = \phi_{\alpha,\tau} u_{\alpha,t/b}(\tau \mathbf{K}), \quad (C8)$$

where (Table VII)

$$\phi_{E',\tau} = e^{-i\frac{2\pi}{3}\tau}, \quad \phi_{E'',\tau} = e^{i\frac{2\pi}{3}\tau}, \quad \text{and } \phi_{A',\tau} = 1. \quad (C9)$$

This immediately gives

$$T_{\alpha,\beta}(\mathbf{r}_0) = t_{\alpha,\beta} \sum_{\mu=0}^{2} e^{i\tau C_3^\mu \mathbf{K} \cdot \mathbf{r}_0} \phi_{\alpha,\tau\mu}^* \phi_{\beta,\tau\mu}, \quad (C10)$$
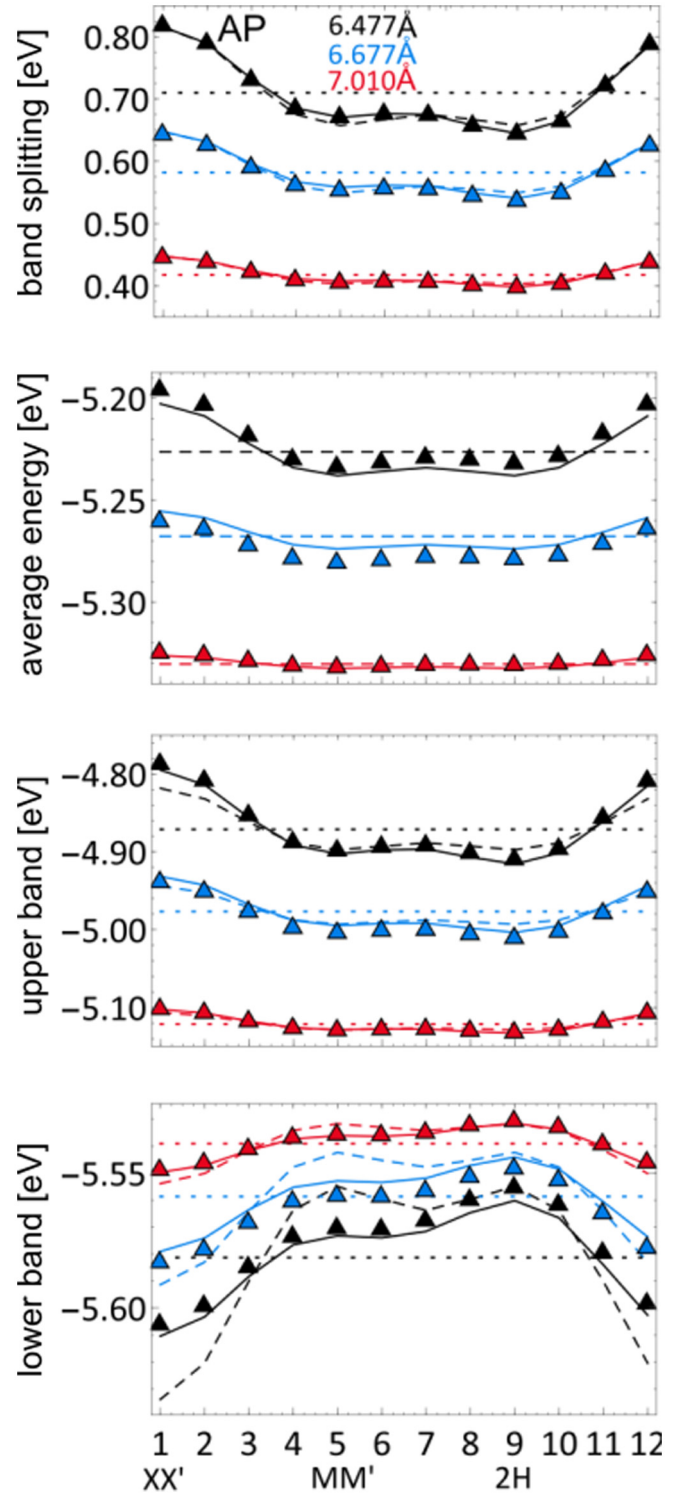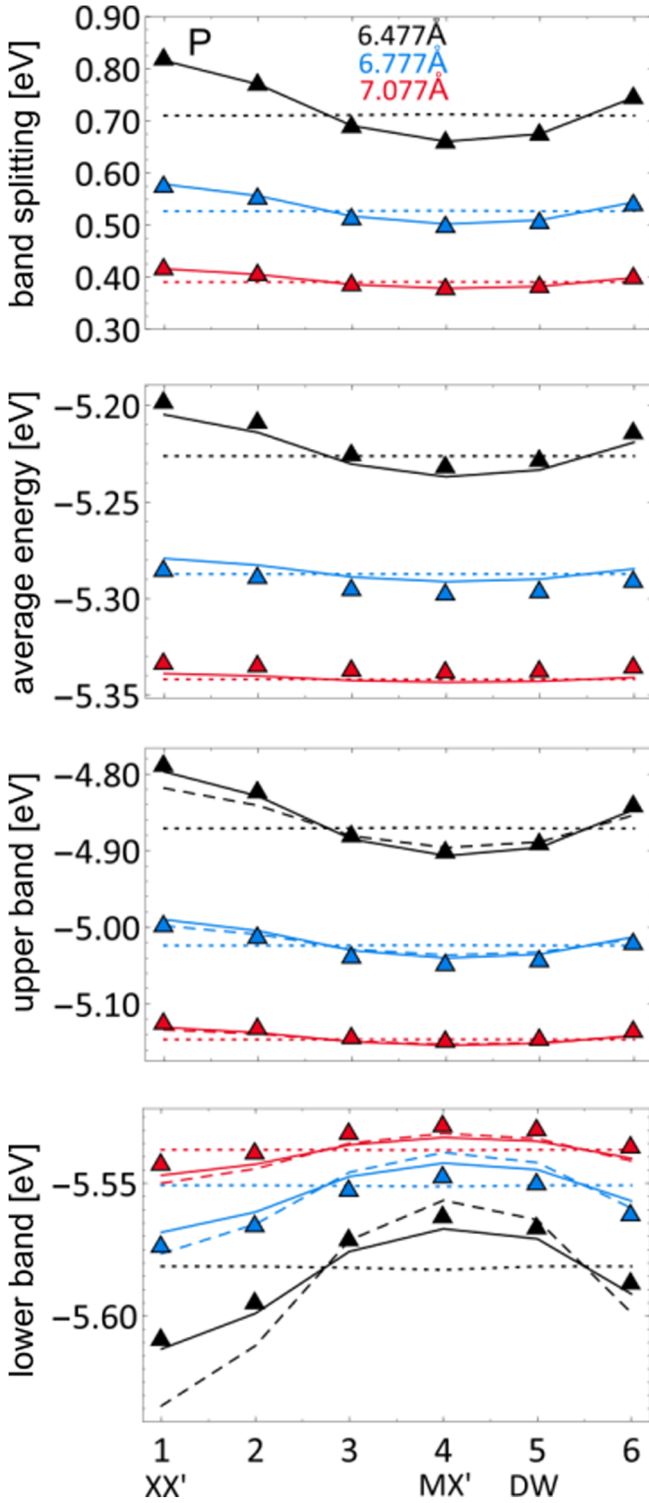
FIG. 23. DFT-computed values (triangles) for splitting, average, and individual energies of the two top-most valence band states in Γ point of P-WSe$_2$ bilayers along the stacking configuration path in Fig. 26(b) versus corresponding values obtained with $H_\Gamma^P + \delta H_\Gamma^P$ (solid) and H_Γ^P (dashed). Dotted straight lines show results for the energies calculated with H_{AP}^{AP} at $t_1^{AP} = 0$, (i.e., with account of only the largest interlayer-distance-dependent terms), emphasizing major role of interlayer distance variation on position of band edge in Γ point of the bilayers.

TABLE VIII. Fitting parameters for the exponential d dependence of the coefficients entering Eq. (C4). The interpolation formula used was $P(d) = Ae^{-qz}$.

	A (meV)	q (Å^{-1})
$v_{VB,0}^P$	10.8	1.8
$v_{VB,1}^P$	3.0	2.9
$|t_{VB}^P|$	17.2	1.5
Δ_P	7.8	2.3

with $t_{\alpha,\beta} \equiv t_{\alpha,\beta}(\tau\mathbf{K})$ for short. The hopping terms relevant to Eq. (C4) are

$$T_{VB}^P(\mathbf{r}_0) = t_{VB}^P \sum_{\mu=0}^{2} e^{iC_3^\mu \tau\mathbf{K}\cdot\mathbf{r}_0},$$

$$T_{E',E''}^P(\mathbf{r}_0) = t_{E',E''}^P \sum_{\mu=0}^{2} e^{iC_3^\mu \tau\mathbf{K}\cdot\mathbf{r}_0} e^{-i\frac{2\pi}{3}\tau\mu}, \quad \text{(C11)}$$

$$T_{E'',E'}^P(\mathbf{r}_0) = t_{E'',E'}^P \sum_{\mu=0}^{2} e^{iC_3^\mu \tau\mathbf{K}\cdot\mathbf{r}_0} e^{i\frac{2\pi}{3}\tau\mu},$$

where inversion symmetry (simultaneous layer exchange and $\mathbf{r}_0 \to -\mathbf{r}_0$) requires that $t_{E',E''} = t_{E'',E'}$. Note, however, that $T_{E',E''}^P$ and $T_{E'',E'}^P$ depend differently on $\mathbf{r}_0$. Substitution into Eq. (C5) finally gives

$$\varepsilon_{VB}^P(\mathbf{r}_0) = \varepsilon_{E'} - v_{VB,0}^P - v_{VB,1}^P \sum_{j=1}^{3} \cos(\mathbf{G}_j \cdot \mathbf{r}_0),$$

$$\Delta^P(\mathbf{r}_0) = \Delta_a^P \sum_{j=1}^{3} \sin(\mathbf{G}_j \cdot \mathbf{r}_0), \quad \text{(C12)}$$

where the expression obtained for $\Delta^P(\mathbf{r}_0)$ matches that of Eq. (5) for the ferroelectric potential energy difference between the layers.

Each parameter appearing in Eq. (C12) was fitted to DFT data for different interlayer distances, and interpolated as $P(d) = Ae^{-q(d-d_0)}$. The results are shown in Table VIII, and a comparison between the DFT band structures and the fitted model Eq. (C4) is shown in Fig. 24.

2. AP stacking

The same analysis for AP stacking, this time including also band A', gives the Hamiltonian

$$H_{AP,K}^\tau = \begin{pmatrix} \varepsilon_{VB}^{AP}(\mathbf{r}_0) + \tau s\frac{\Delta_{VB}^{SO}(\mathbf{r}_0)}{2} & T_{VB}^{AP}(\mathbf{r}_0) \\ T_{VB}^{AP*}(\mathbf{r}_0) & \varepsilon_{VB}^{AP}(\mathbf{r}_0) - \tau s\frac{\Delta_{VB}^{SO}(\mathbf{r}_0)}{2} \end{pmatrix},$$
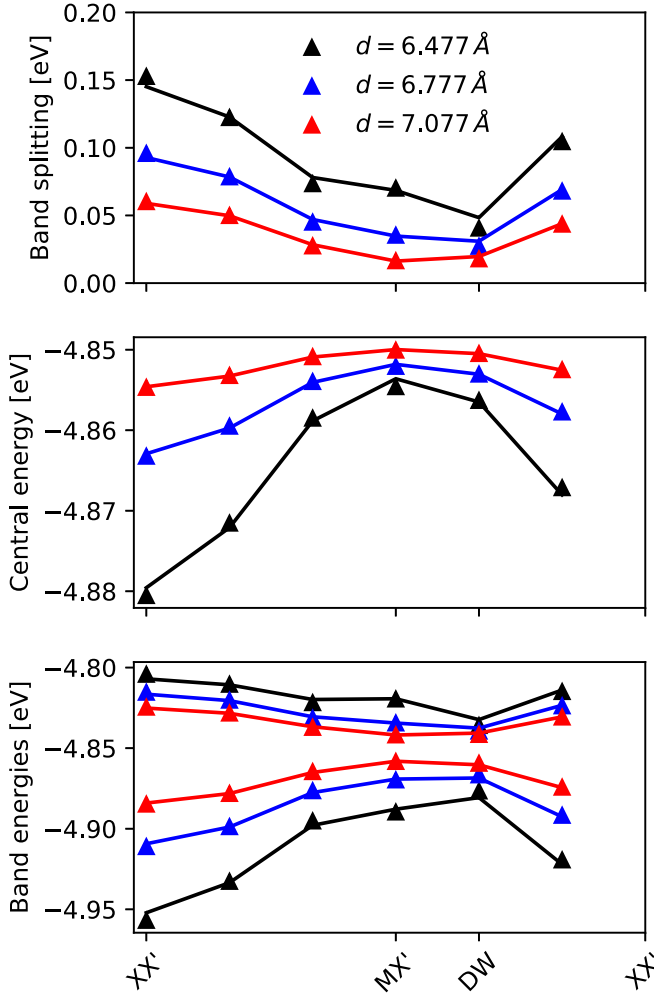
(C13)

FIG. 24. Comparison between the DFT results and the model Eq. (C4) for (top) the band splitting, (middle) central energy, and (bottom) band energies as a function of stacking configuration, using the parameters of Table VIII.

where

$$\varepsilon_{VB}^{AP}(\mathbf{r}_0) = \varepsilon_{E'} + \frac{1}{2} \sum_{\alpha=E'',A'}^{2} \frac{(\varepsilon_{E'} - \varepsilon_{\alpha})|T_{\alpha,E'}^{AP}(\mathbf{r}_0)|^2}{(\varepsilon_{E'} - \varepsilon_{\alpha})^2 - \frac{(\Delta_{E'}^{SO}+\Delta_{\alpha}^{SO})^2}{4}},$$

$$\Delta_{VB}^{SO}(\mathbf{r}_0) = \Delta_{VB}^{SO} + \frac{1}{2} \sum_{\alpha=E'',A'}^{2} \frac{(\Delta_{E'}^{SO}+\Delta_{\alpha}^{SO})|T_{\alpha,E'}^{AP}(\mathbf{r}_0)|^2}{(\varepsilon_{E'} - \varepsilon_{\alpha})^2 - \frac{(\Delta_{E'}^{SO}+\Delta_{\alpha}^{SO})^2}{4}}.$$

(C14)

The corresponding hopping terms are

$$T_{VB}^{AP}(\mathbf{r}_0) = t_{VB}^{AP} \sum_{\mu=0}^{2} e^{iC_3^{\mu}\tau\mathbf{K}\cdot\mathbf{r}_0} e^{i\frac{2\pi}{3}\tau\mu},$$

$$T_{E',E''}^{AP}(\mathbf{r}_0) = t_{E',E''} \sum_{\mu=0}^{2} e^{iC_3^{\mu}\tau\mathbf{K}\cdot\mathbf{r}_0},$$

$$T_{E'',E'}^{AP}(\mathbf{r}_0) = t_{E'',E'} \sum_{\mu=0}^{2} e^{iC_3^{\mu}\tau\mathbf{K}\cdot\mathbf{r}_0},$$

TABLE IX. Fitting parameters for the exponential d dependence of the coefficients entering Eq. (C13). The interpolation formula used was $P(d) = Ae^{-qz}$.

	A (meV)	q (Å^{-1})
$v_{VB,0}^{AP}$	10.5	1.6
$v_{VB,1}^{AP}$	1.1	2.8
$v_{VB,2}^{AP}$	−1.3	3.3
$|t_{VB}^{AP}|$	9.8	1.5
$\tilde{\Delta}_{VB,1}^{SO}$	−0.9	2.9
$\tilde{\Delta}_{VB,2}^{SO}$	−0.8	2.9

$$T_{E',A'}^{AP}(\mathbf{r}_0) = t_{E',A'} \sum_{\mu=0}^{2} e^{iC_3^{\mu}\tau\mathbf{K}\cdot\mathbf{r}_0} e^{-i\frac{2\pi}{3}\tau\mu},$$

$$T_{A',E'}^{AP}(\mathbf{r}_0) = t_{A',E'} \sum_{\mu=0}^{2} e^{iC_3^{\mu}\tau\mathbf{K}\cdot\mathbf{r}_0} e^{-i\frac{2\pi}{3}\tau\mu}. \quad (C15)$$

Contrary to the case of P stacking, the matrix elements $T_{E',E''}^{AP}$ and $T_{E',A'}^{AP}$ have the same $\mathbf{r}_0$ dependence as $T_{E'',E'}^{AP}$ and $T_{A',E'}^{AP}$, respectively. However, they appear with different denominators in Eq. (C14) due to spin-orbit coupling. Substituting Eq. (C15) into Eq. (C14) gives

$$\varepsilon_{VB}^{AP}(\mathbf{r}_0) = \varepsilon_{E'} - v_{VB,0}^{AP} - v_{VB,1}^{AP} \sum_{j=1}^{3} \cos(\mathbf{G}_j \cdot \mathbf{r}_0)$$

$$- v_{VB,2}^{AP} \sum_{j=1}^{3} \sin(\mathbf{G}_j \cdot \mathbf{r}_0),$$

$$\Delta_{VB}^{SO}(\mathbf{r}_0) = \Delta_{VB}^{SO} + \tilde{\Delta}_{VB,0}^{SO} + \tilde{\Delta}_{VB,1}^{SO} \sum_{j=1}^{3} \cos(\mathbf{G}_j \cdot \mathbf{r}_0)$$

$$+ \tilde{\Delta}_{VB,2}^{SO} \sum_{j=1}^{3} \sin(\mathbf{G}_j \cdot \mathbf{r}_0),$$

(C16)

where inversion symmetry dictates that $|T_{E',\alpha}^{AP}|^2 = |T_{\alpha,E'}^{AP}|^2$.

Fitting the model parameters to the DFT data reveals that $v_{VB,2}^{AP} \approx -v_{VB,1}^{AP}$, that $\tilde{\Delta}_{VB,2}^{SO} \approx \tilde{\Delta}_{VB,1}^{SO}$ and $\tilde{\Delta}_{VB,0}^{SO}$ is negligible by comparison to all other SO terms (Table III), and that the constant energy shift $v_{VB,0}^{AP} \approx v_{VB,0}^{P}$ (see Tables VIII and IX). The results are shown in Fig. 25.

3. Hybridization models for the conduction bands

The effective models for the bilayer conduction bands in P- and AP-type bilayers can be constructed in analogy with Eqs. (C4) and (C13). The symmetry rules for the matrix elements $T_{\alpha,\beta}$, where $\alpha, \beta = A', E'', E'$ for CB(K), CB+1(K), and CB+2(K), respectively, are given by

$$\phi_{A',\tau} = 1, \quad \phi_{E'',\tau} = e^{-i\frac{2\pi}{3}\tau}, \quad \text{and} \quad \phi_{E',\tau} = e^{i\frac{2\pi}{3}\tau}. \quad (C17)$$
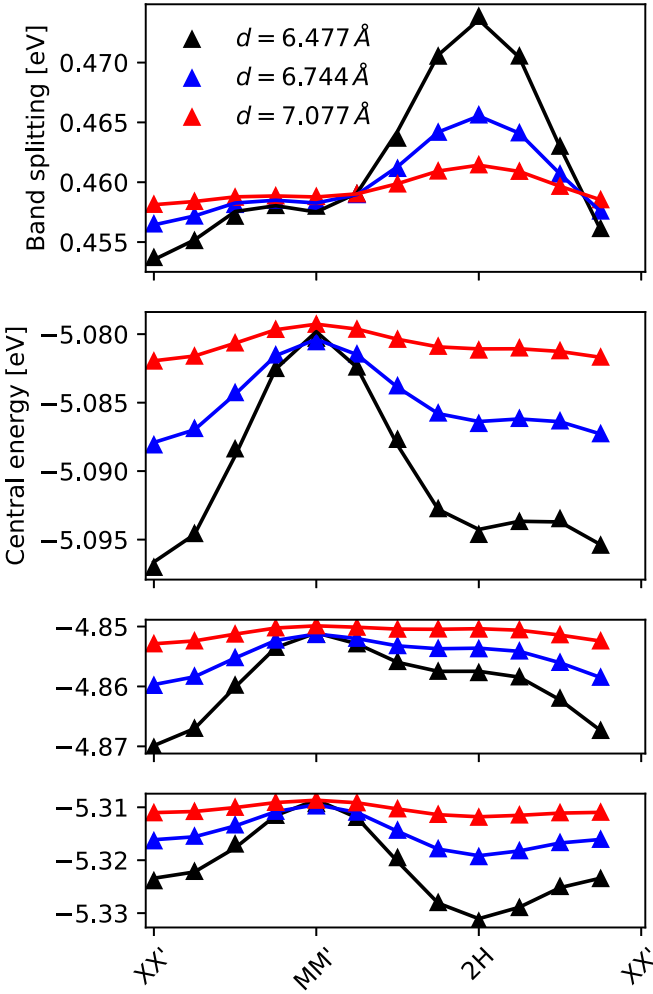
FIG. 25. Comparison between the DFT results and the model Eq. (C13) for (top) the band splitting, (middle) central energy and (bottom) band energies as a function of stacking configuration, using the parameters of Table IX.

The corresponding minimal Hamiltonians for P and AP stacking are

$$H_{P,\tau\mathbf{K}}^{(CB)} = \begin{pmatrix} \varepsilon_{CB}^{P}(\mathbf{r}_0) - \frac{\Delta^{P}(\mathbf{r}_0)}{2} & T_{CB}(\mathbf{r}_0) \\ T_{CB}^{*}(\mathbf{r}_0) & \varepsilon_{CB}^{P}(\mathbf{r}_0) + \frac{\Delta^{P}(\mathbf{r}_0)}{2} \end{pmatrix}, \quad (C18a)$$

$$H_{AP,\tau\mathbf{K}}^{(CB)} = \begin{pmatrix} \varepsilon_{CB}^{AP}(\mathbf{r}_0) - \frac{\tau s \Delta_{CB}^{SO}}{2}(\mathbf{r}_0) & T_{CB}(\mathbf{r}_0) \\ T_{CB}^{*}(\mathbf{r}_0) & \varepsilon_{CB}^{AP}(\mathbf{r}_0) + \frac{\tau s \Delta_{CB}^{SO}}{2}(\mathbf{r}_0) \end{pmatrix}, \quad (C18b)$$

with the definitions

$$\varepsilon_{CB}^{P}(\mathbf{r}_0) = \varepsilon_{A'} - v_{CB,0}^{P} - v_{CB,1}^{P} \sum_{j=1}^{3} \cos{(\mathbf{G}_j \cdot \mathbf{r}_0)}, \quad (C19a)$$

$$\varepsilon_{CB}^{AP}(\mathbf{r}_0) = \varepsilon_{A'} - v_{CB,0}^{AP} - v_{CB,1}^{AP} \sum_{j=1}^{3} \cos{(\mathbf{G}_j \cdot \mathbf{r}_0)}$$

$$- v_{CB,2}^{AP} \sum_{j=1}^{3} \sin{(\mathbf{G}_j \cdot \mathbf{r}_0)}, \quad (C19b)$$

TABLE X. Fitting parameters for the exponential d dependence of the coefficients entering Eq. (C18a). The interpolation formula used was $P(d) = Ae^{-qz}$.

	A (meV)	q (Å^{-1})
$v_{CB,0}^{P}$	11.2	1.8
$v_{CB,1}^{P}$	1.5	2.7
$|t_{CB}|$	3.7	1.5

$$\Delta_{CB}^{SO}(\mathbf{r}_0) = \Delta_{CB}^{SO} + \tilde{\Delta}_{CB,1}^{SO} \sum_{j=1}^{3} \cos{(\mathbf{G}_j \cdot \mathbf{r}_0)}$$

$$+ \tilde{\Delta}_{CB,2}^{SO'} \sum_{j=1}^{3} \sin{(\mathbf{G}_j \cdot \mathbf{r}_0)}, \quad (C19c)$$

$$T_{CB}(\mathbf{r}_0) = t_{CB} \sum_{\mu=0}^{2} e^{i\tau C_3^{\mu}\mathbf{K} \cdot \mathbf{r}_0}. \quad (C19d)$$

Our DFT calculations show that (i) $|\tilde{\Delta}_{CB,2}^{SO}| \ll |\tilde{\Delta}_{CB,1}|, |\Delta_{CB}^{SO}|$, and thus can be safely neglected, whereas $\tilde{\Delta}_{CB,1}^{SO} \approx \tilde{\Delta}_{VB,1}^{SO}$; (ii) as in the valence band case, the constant energy shifts $v_{CB,0}^{P} \approx v_{CB,0}^{AP}$, and in fact they coincide with $v_{VB,0}^{P/AP}$ to within $\sim$1 meV; moreover, (iii) the conduction-band hopping parameters t_{CB} coincide for P and AP stacking (see Tables VIII–XI); and (iv) $v_{CB,2}^{AP} \approx v_{CB,2}^{P}$. Importantly, the DFT results also show that the same splitting $\Delta^{P}(\mathbf{r}_0)$ appearing for the K-point valence bands, as well as for both the conduction and valence bands at the Γ point, is also present for the K-point conduction bands, which is consistent with a purely electrostatic interlayer bias acting on the metallic orbitals.

4. Summary

Put together, our symmetry analysis and DFT results show that the effective Hamiltonian for the top two valence sub-bands at the K point is given by

$$H_{VB,K} = \begin{pmatrix} \varepsilon_{VB}(\mathbf{r}_0, d) - \frac{S_{VB}^{P/AP}(\mathbf{r}_0)}{2} & T_{VB,\tau}^{P/AP}(\mathbf{r}_0, d) \\ T_{VB,\tau}^{P/AP*}(\mathbf{r}_0, d) & \varepsilon_{VB}(\mathbf{r}_0, d) + \frac{S_{VB}^{P/AP}(\mathbf{r}_0)}{2} \end{pmatrix}, \quad (C20)$$

TABLE XI. Fitting parameters for the exponential d dependence of the coefficients entering Eq. (C18b). The interpolation formula used was $P(d) = Ae^{-qz}$.

	A (meV)	q (Å^{-1})
$v_{CB,0}^{AP}$	11.2	1.3
$v_{CB,1}^{AP}$	0.7	2.9
$v_{CB,2}^{AP}$	0.4	2.3
$|t_{CB}^{AP}|$	3.7	1.0
$\tilde{\Delta}_{CB,1}^{SO}$	−1.6	2.0
$\tilde{\Delta}_{CB,2}^{SO'}$	0.1	1.3

with the definitions

$$\varepsilon_{\text{VB}}^{\text{P}}(\mathbf{r}_0, d) = \varepsilon_{E'} - v_0 - v_{\text{VB},1}^{\text{P}} \sum_{j=1}^{3} \cos(\mathbf{G}_j \cdot \mathbf{r}_0),$$

$$\varepsilon_{\text{VB}}^{\text{AP}}(\mathbf{r}_0, d) = \varepsilon_{E'} - v_0 - v_{\text{VB}}^{\text{AP}} \sqrt{2} \sum_{j=1}^{3} \cos\left(\mathbf{G}_j \cdot \mathbf{r}_0 + \frac{\pi}{4}\right),$$

(C21a)

$$S_{\text{VB}}^{\text{P}}(\mathbf{r}_0, d) = \Delta^{\text{P}}(\mathbf{r}_0, d); \quad \Delta_{\text{VB}}^{\text{AP}}(\mathbf{r}_0, d) = -\tau s \Delta_{\text{VB}}^{\text{SO}},$$

(C21b)

$$T_{\text{VB}}^{\text{P}}(\mathbf{r}_0, d) = t_{\text{VB}}^{\text{P}}(d) \sum_{\mu=0}^{2} e^{i\tau C_3^{\mu} \mathbf{K} \cdot \mathbf{r}_0},$$

$$T_{\text{VB}}^{\text{AP}}(\mathbf{r}_0, d) = t_{\text{VB}}^{\text{AP}}(d) \sum_{\mu=0}^{2} e^{i\tau C_3^{\mu} \mathbf{K} \cdot \mathbf{r}_0} e^{i\frac{2\pi}{3}\tau\mu},$$

(C21c)

where we have used the fact that $v_{\text{VB},2}^{\text{AP}} \approx -v_{\text{VB},1}^{\text{AP}}$ and the identity $\cos(x \pm \pi/4) = [\cos(x) \mp \sin(x)]/\sqrt{2}$ to simplify $\varepsilon_{\text{VB}}^{\text{AP}}(\mathbf{r}_0, d)$.

Similarly, the effective Hamiltonian for the bottom two conduction subbands takes the form

$$H_{\text{CB},K} = \begin{pmatrix} \varepsilon_{\text{CB}}(\mathbf{r}_0, d) - \frac{S_{\text{CB}}^{\text{P/AP}}(\mathbf{r}_0)}{2} & T_{\text{CB},\tau}(\mathbf{r}_0, d) \\ T_{\text{CB},\tau}^{*}(\mathbf{r}_0, d) & \varepsilon_{\text{CB}}(\mathbf{r}_0, d) + \frac{S_{\text{CB}}^{\text{P/AP}}(\mathbf{r}_0)}{2} \end{pmatrix},$$

(C22)

with the definitions

$$\varepsilon_{\text{CB}}^{\text{P}}(\mathbf{r}_0, d) = \varepsilon_{\text{CB}} - v_0 - v_{\text{CB},1}^{\text{P}} \sum_{j=1}^{3} \cos(\mathbf{G}_j \cdot \mathbf{r}_0),$$

$$\varepsilon_{\text{CB}}^{\text{AP}}(\mathbf{r}_0, d) = \varepsilon_{\text{CB}} - v_0 - v_{\text{CB},1}^{\text{AP}} \sqrt{2} \sum_{j=1}^{3} \cos\left(\mathbf{G}_j \cdot \mathbf{r}_0 - \frac{\pi}{4}\right),$$

(C23a)

$$S_{\text{CB}}^{\text{P}}(\mathbf{r}_0, d) = \Delta_{\text{P}}(\mathbf{r}_0, d); \quad S_{\text{CB}}^{\text{AP}}(\mathbf{r}_0, d) = \tau s \Delta_{\text{CB}}^{\text{SO}},$$

(C23b)

$$T_{\text{CB}}(\mathbf{r}_0, d) = t_{\text{CB}}(d) \sum_{\mu=0}^{2} e^{i\tau C_3^{\mu} \mathbf{K} \cdot \mathbf{r}_0},$$

(C23c)

using $v_{\text{CB},2}^{\text{AP}} \approx v_{\text{CB},1}^{\text{AP}}$. It is then convenient to rescale $\sqrt{2} v_{\text{CB},1}^{\text{AP}} \to v_{\text{CB},1}^{\text{AP}}$ and rewrite

$$\sum_{\mu=0}^{2} e^{i\tau C_3^{\mu} \mathbf{K} \cdot \mathbf{r}_0} = e^{i\tau \frac{4\pi x_0}{3a}} + 2 e^{-i\tau \frac{2\pi x_0}{3a}} \cos\left(\frac{2\pi y_0}{a\sqrt{3}}\right),$$

$$\sum_{\mu=0}^{2} e^{i\tau C_3^{\mu} \mathbf{K} \cdot \mathbf{r}_0} e^{i\frac{2\pi}{3}\mu\tau} = e^{i\tau \frac{4\pi x_0}{3a}} + 2 e^{-i\tau \frac{2\pi x_0}{3a}} \cos\left(\frac{2\pi y_0}{a\sqrt{3}} + \frac{2\pi}{3}\right),$$

(C24)

where we have used $\mathbf{K} = \frac{4\pi}{3a}\hat{\mathbf{x}}$. Finally, writing all sums of sines and cosines in terms of $f_s(\mathbf{r}_0)$ and $f_a(\mathbf{r}_0)$ [see Eq. (1)] gives the Hamiltonian shown in Sec. IV B.

APPENDIX D: DFT CALCULATIONS AND CONFIGURATIONS USED FOR MODEL PARAMETRIZATION

These calculations are carried out using the plane-wave based VASP code [80] with spin-orbit coupling taken into account using projector augmented wave (PAW) pseudopotentials. We approximated the exchange correlation functional using the generalized gradient approximation (GGA) of Perdew, Burke, and Ernzerhof [81]. The cutoff energy for the plane-waves is set to 600 eV with the in-plane Brillouin zone sampled by a 12×12 grid. Above, we introduced the effective Hamiltonians for the Γ- and K-point top valence band states in WSe$_2$ bilayers with phenomenological parameters fitted to energy bands calculated with DFT for 6 (P-stacked bilayers) and 12 (AP-stacked bilayers) in-plane shifts $\mathbf{r}_0$, repeated for 6(11)
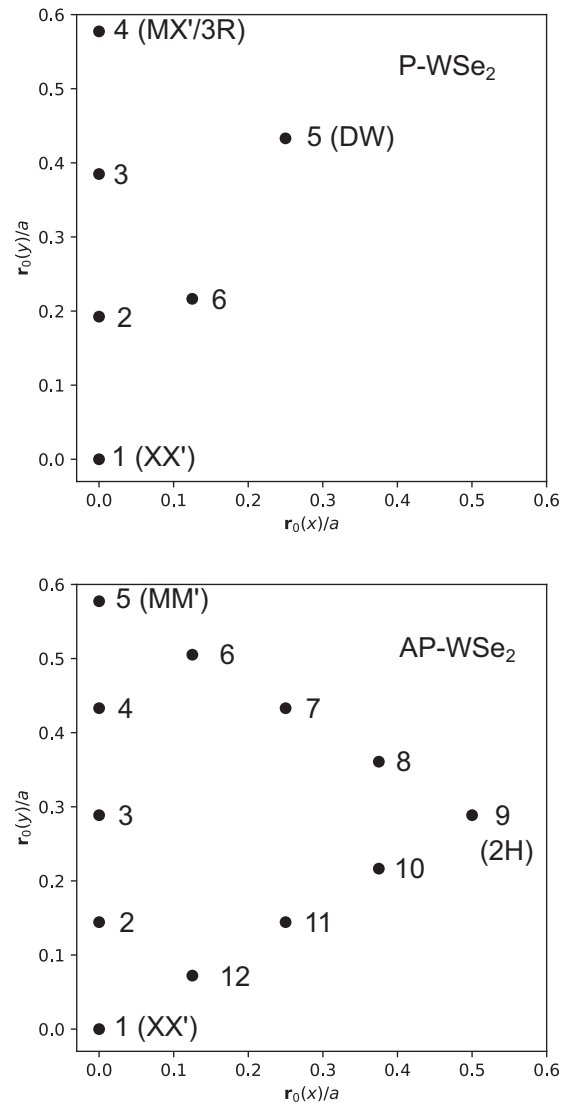

FIG. 26. Schematic of in-plane shifts, $\mathbf{r}_0$, in configuration space, used in the DFT parametrizations of the models described in Appendices B and C in units of the lattice constant $a = 3.282$ Å, for P-stacking and AP-stacking in the upper and lower panel, respectively. The points are numbered to identify their progression around the paths.

interlayer distances spanning $d = 6.477$ Å to $d = 7.077$ Å for P-(AP-)stacking. The paths in configuration space traced by the in-plane shifts are plotted in Fig. 26. From the point of view of the band energies, the paths form the boundary of the irreducible portion of in-plane shifts. To minimize the interaction between them, repeated images of bilayers are placed 30 Å apart, with P-stacked bilayers using supercells containing two σ_h-reflected images of the bilayers to maintain periodicity along z taking into account the potential drop across a P-stacked bilayer due to interlayer charge transfer, as set out in the main text. The structure parameters for the monolayer are taken from experimental measurements of the bulk crystal [34].

APPENDIX E: PIEZOELECTRIC POTENTIAL FOR WSe$_2$ BILAYERS ENCAPSULATED IN hBN

To calculate electric potential, $\varphi(\mathbf{r}, z)$, created by piezocharges in twisted AP/P-WSe$_2$ bilayers we expand the piezocharge densities in Fourier series over superlattice reciprocal vectors $\rho_{t/b} = \delta(z - z_{t/b}) \sum \rho_n^{t/b} e^{i g_n \mathbf{r}}$ and take into account polarization charges, $\rho_{\text{ind}}^{t/b} = \alpha_{2D}^{t/b} \delta(z - z_{t/b}) \nabla_{\mathbf{r}}^2 \varphi(\mathbf{r}, z_{t/b})$, which are induced by the piezocharges ($\alpha_{2D}^{t/b} = d_0(\varepsilon_{\|}^{t/b} - 1)/4\pi$ is the in-plane 2D polarizability of the top/bottom monolayer expressed via in-plane dielectric permittivity of bulk WSe$_2$ crystals [82].

The total charge densities in each layer are sum of the piezo- and polarization charge densities. To find piezo-electric potential created by the total charge densities, $\rho_{\text{tot}}^{t/b} = \rho_{\text{piezo}}^{t/b} + \rho_{\text{ind}}^{t/b}$ we solve the Poisson equation,

$$\big[\epsilon_\perp \partial_{zz}^2 + \epsilon_\| \nabla_{\mathbf{r}}^2 \big]\varphi = 0, \; z > z_1, \; z < z_2$$
$$\big[\partial_{zz}^2 + \nabla_{\mathbf{r}}^2\big]\varphi = -4\pi\big(\rho_{\text{tot}}^t + \rho_{\text{tot}}^b\big), \; z_2 \leqslant z \leqslant z_1, \quad \text{(E1)}$$

by expanding the potential in Fourier series over the superlattice reciprocal vectors, $\varphi(\mathbf{r}, z) = \sum_n \widetilde{\varphi}_n(z) e^{i g_n \mathbf{r}}$. In Eq. (E1) $\epsilon_\perp = 3.76$, $\epsilon_\| = 6.93$ are in-layer and out-of-layer dielectric permittivities of bulk hBN crystals (see Fig. 27). Solving the Poisson Eq. (E1) in each region with corresponding boundary conditions at interfaces we find amplitudes of the potential
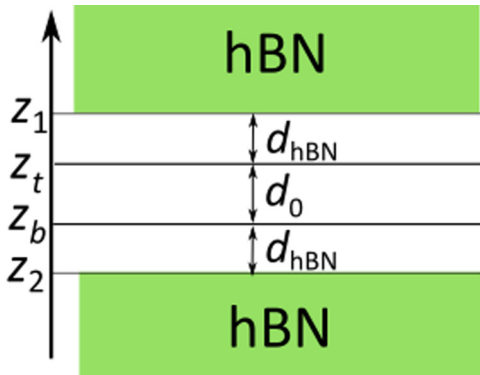

FIG. 27. Model used to calculate piezoelectric potential of WSe$_2$ bilayer encapsulated in hBN.

harmonics in the top and bottom layers:

$$\varphi_n(z_t) = \frac{2\pi}{g_n}[\cosh(g_n d_{\text{hBN}}) + \sqrt{\epsilon_\| \epsilon_\perp} \sinh(g_n d_{\text{hBN}})]$$
$$\times \frac{\rho_n^t\big(F_1^b e^{g_n d_0} + F_2^b\big) + \rho_n^b\big(F_1^b + F_2^b e^{g_n d_0}\big)}{F_1^t F_1^b - F_2^t F_2^b}, \quad \text{(E2)}$$

$$\varphi_n(z_b) = \frac{2\pi}{g_n}[\cosh(g_n d_{\text{hBN}}) + \sqrt{\epsilon_\| \epsilon_\perp} \sinh(g_n d_{\text{hBN}})]$$
$$\times \frac{\rho_n^t\big(F_1^t + F_2^t e^{g_n d_0}\big) + \rho_n^b\big(F_1^t e^{g_n d_0} + F_2^t\big)}{F_1^t F_1^b - F_2^t F_2^b}, \quad \text{(E3)}$$

where the Fourier amplitudes of piezo-charge density read as

$$\rho_n^{t/b} = e_{11}^{t/b}\big[2g_{nx}g_{ny}u_{nx}^{t/b} + \big(g_{nx}^2 - g_{ny}^2\big)u_{ny}^{t/b}\big], \quad \text{(E4)}$$

with $e_{11} = 2.03 \times 10^{-10}$C/m [36], and

$$F_1^{t/b} = e^{g_n(d_0 + d_{\text{hBN}})}\frac{1 + \sqrt{\epsilon_\| \epsilon_\perp}}{2} + 2\pi \alpha_{2D}^{t/b} g_n e^{g_n d_0}[\cosh(g_n d_{\text{hBN}})$$
$$+ \sqrt{\epsilon_\| \epsilon_\perp} \sinh(g_n d_{\text{hBN}})], \quad \text{(E5)}$$

$$F_2^{t/b} = e^{-g_n d_{\text{hBN}}}\frac{1 - \sqrt{\epsilon_\| \epsilon_\perp}}{2} - 2\pi \alpha_{2D}^{t/b} g_n[\cosh(g_n d_{\text{hBN}})$$
$$+ \sqrt{\epsilon_\| \epsilon_\perp} \sinh(g_n d_{\text{hBN}})]. \quad \text{(E6)}$$

Here, $d_{\text{hBN}} = z_1 - z_t = z_b - z_2 = (6.71 + 3.35)/2$ Å is distance between WSe$_2$ bilayer and hBN. In main manuscript we used the shorthand for potential on top and bottom layers as follows: $\varphi_{t/b}(\mathbf{r}) = \varphi(\mathbf{r}, z_{t/b})$. The total charge density in the top layer, $\rho_{\text{tot}}^t = \sum_n (\rho_n^t - 4\pi g_n^2 \alpha_{2D}^t \varphi_n^t) e^{i g_n \mathbf{r}}$.

TABLE XII. Coefficients of the reference vectors $\mathbf{g}_{3n+1}$, as defined in Eq. (F4).

	m_1	m_2
$\mathbf{g}_1$	1	0
$\mathbf{g}_4$	1	−1
$\mathbf{g}_7$	2	0
$\mathbf{g}_{10}$	3	2
$\mathbf{g}_{13}$	3	1
$\mathbf{g}_{16}$	3	0
$\mathbf{g}_{19}$	4	2
$\mathbf{g}_{22}$	4	1
$\mathbf{g}_{25}$	3	−1
$\mathbf{g}_{28}$	4	0
$\mathbf{g}_{31}$	5	3
$\mathbf{g}_{34}$	5	2
$\mathbf{g}_{37}$	5	4
$\mathbf{g}_{40}$	5	1
$\mathbf{g}_{43}$	5	0
$\mathbf{g}_{46}$	6	3
$\mathbf{g}_{49}$	6	4
$\mathbf{g}_{52}$	6	2
$\mathbf{g}_{55}$	6	1
$\mathbf{g}_{58}$	6	5

TABLE XIII. Coefficients of the moiré harmonics expansion Eq. (4) for the spatial variation of the interlayer distance in P-stacked bilayers with different twist angles. All values are given in units of 10^{-2} Å.

	$\theta_P = 1.4°$		$\theta_P = 2.0°$		$\theta_P = 3.0°$		$\theta_P = 4.0°$	
	z_n^s	z_n^a	z_n^s	z_n^a	z_n^s	z_n^a	z_n^s	z_n^a
$n = 0$	-25.58697	0.00000	-20.55009	0.00000	-12.39398	0.00000	-7.55040	0.00000
$n = 1, 2, 3$	5.94496	0.00000	7.99818	0.00000	10.56258	0.00000	11.81364	0.00000
$n = 4, 5, 6$	2.21727	0.00000	2.48982	0.00000	1.93853	0.00000	1.23485	0.00000
$n = 7, 8, 9$	3.34285	0.00000	3.19196	0.00000	2.12191	0.00000	1.22791	0.00000
$n = 10, 11, 12$	0.93257	0.00000	0.70117	0.00000	0.15368	0.00000	-0.01490	0.00000
$n = 13, 14, 15$	0.94016	0.00000	0.71081	0.00000	0.14847	0.00000	-0.02342	0.00000
$n = 16, 17, 18$	1.38383	0.00000	0.84737	0.00000	0.19193	0.00000	0.02006	0.00000
$n = 19, 20, 21$	0.33587	0.00000	0.11963	0.00000	-0.03378	0.00000	-0.03073	0.00000
$n = 22, 23, 24$	0.34418	0.00000	0.12695	0.00000	-0.02191	0.00000	-0.02212	0.00000
$n = 25, 26, 27$	0.34708	0.00000	0.13040	0.00000	-0.02701	0.00000	-0.02360	0.00000
$n = 28, 29, 30$	0.50022	0.00000	0.15393	0.00000	-0.00077	0.00000	0.00047	0.00000
$n = 31, 32, 33$	0.10877	0.00000	-0.01108	0.00000	-0.01406	0.00000	-0.00942	0.00000
$n = 34, 35, 36$	0.10720	0.00000	-0.02050	0.00000	-0.01697	0.00000	0.00252	0.00000
$n = 37, 38, 39$	0.12186	0.00000	-0.00057	0.00000	-0.00550	0.00000	0.00210	0.00000
$n = 40, 41, 42$	0.10738	0.00000	0.00533	0.00000	-0.01713	0.00000	0.00735	0.00000
$n = 43, 44, 45$	0.16345	0.00000	0.01498	0.00000	-0.00487	0.00000	0.00507	0.00000
$n = 46, 47, 48$	0.01585	0.00000	-0.01386	0.00000	-0.00050	0.00000	-0.00480	0.00000
$n = 49, 50, 51$	0.01925	0.00000	-0.01096	0.00000	-0.01046	0.00000	-0.00874	0.00000
$n = 52, 53, 54$	0.03639	0.00000	-0.00787	0.00000	-0.00559	0.00000	0.00228	0.00000
$n = 55, 56, 57$	0.03680	0.00000	-0.00700	0.00000	0.00607	0.00000	0.00735	0.00000
$n = 58, 59, 60$	0.03551	0.00000	-0.01305	0.00000	-0.01864	0.00000	-0.01080	0.00000

TABLE XIV. Coefficients of the moiré harmonics expansion Eq. (4) for the spatial variation of the interlayer distance in AP-stacked bilayers with different twist angles. All values are given in units of 10^{-2} Å.

	$\theta_{AP} = 1.4°$		$\theta_{AP} = 2.0°$		$\theta_{AP} = 3.0°$		$\theta_{AP} = 4.0°$	
	z_n^s	z_n^a	z_n^s	z_n^a	z_n^s	z_n^a	z_n^s	z_n^a
$n = 0$	-24.13399	0.00000	-19.05858	0.00000	-11.53592	0.00000	-6.65903	0.00000
$n = 1, 2, 3$	-5.50791	3.24141	-6.16899	4.52594	-6.74953	6.86940	-7.01133	7.94786
$n = 4, 5, 6$	2.82852	-0.00163	2.55399	-0.00287	1.74925	-0.00282	1.10190	0.00027
$n = 7, 8, 9$	0.67310	-2.56605	0.32295	-2.70102	0.04658	-1.84220	-0.00550	-1.14069
$n = 10, 11, 12$	-0.78417	-0.91178	-0.54056	-0.60187	-0.13118	-0.13734	-0.01039	-0.01058
$n = 13, 14, 15$	-0.80308	0.90362	-0.54585	0.59891	-0.14142	0.13902	-0.02071	0.00816
$n = 16, 17, 18$	0.45891	0.87199	0.41816	0.64093	0.10759	0.18354	0.01592	0.04758
$n = 19, 20, 30$	0.44231	-0.00065	0.19873	0.00296	-0.00732	0.00295	-0.01067	0.00541
$n = 31, 32, 33$	-0.02988	-0.52235	0.00011	-0.21693	0.00789	0.00567	0.00169	0.01213
$n = 34, 35, 36$	-0.03029	-0.52334	-0.00259	-0.22186	0.00403	0.00447	-0.00242	0.01619
$n = 37, 38, 39$	-0.30441	-0.10434	-0.15945	-0.06188	-0.00915	-0.01331	0.00372	-0.00496
$n = 40, 41, 42$	-0.11498	-0.14544	-0.03342	-0.03053	0.00412	0.00503	-0.00269	0.00408
$n = 43, 44, 45$	-0.11432	0.13318	-0.02114	0.03925	0.01359	-0.00473	0.00616	-0.00671
$n = 46, 47, 48$	0.13680	-0.15399	0.03093	-0.04459	0.00227	0.01083	0.00313	-0.00780
$n = 49, 50, 51$	0.13037	0.15145	0.03238	0.01842	-0.00111	-0.00694	-0.00064	-0.00027
$n = 52, 53, 54$	0.10133	-0.03621	0.03233	-0.00575	0.00822	0.00331	0.00154	-0.00116
$n = 55, 56, 57$	0.05078	-0.00077	-0.00051	-0.00329	-0.00340	-0.00109	-0.00098	0.00211
$n = 58, 59, 60$	-0.01020	0.06517	-0.00164	0.00853	0.00487	-0.00159	0.00676	0.00567
$n = 61, 62, 63$	0.00405	-0.06227	-0.00889	-0.00860	-0.00023	-0.00410	-0.00004	-0.00092
$n = 64, 65, 66$	-0.05478	-0.01542	-0.00834	0.00509	-0.00092	0.00175	0.00065	-0.00239
$n = 67, 68, 69$	-0.06405	0.02779	-0.01315	-0.00370	0.00997	0.00561	0.00515	0.00170

TABLE XV. Coefficients of the moiré harmonics expansion Eq. (31) for the piezoelectric potential $\varphi(\mathbf{r})$, for P bilayers with different twist angles. The top- and bottom-layer potential coefficients are given by $\varphi_n^t = \varphi_n$ and $\varphi_n^b = -\varphi_n$. All values are in units of mV.

	$\theta_{\mathrm{P}} = 1.4°$		$\theta_{\mathrm{P}} = 2.0°$		$\theta_{\mathrm{P}} = 3.0°$		$\theta_{\mathrm{P}} = 4.0°$	
	Re φ_n	Im φ_n	Re φ_n	Im φ_n	Re φ_n	Im φ_n	Re φ_n	Im φ_n
$n = 0$	0.00000	0.00000	0.00000	0.00000	0.00000	0.00000	0.00000	0.00000
$n = 1, 2, 3$	0.00000	−14.22201	0.00000	−12.33073	0.00000	−7.45156	0.00000	−4.45439
$n = 4, 5, 6$	0.00000	−0.00115	0.00000	0.00900	0.00000	0.00219	0.00000	0.00051
$n = 7, 8, 9$	0.00000	−2.59835	0.00000	−1.03104	0.00000	−0.02926	0.00000	0.11522
$n = 10, 11, 12$	0.00000	0.02994	0.00000	−0.06365	0.00000	−0.05794	0.00000	−0.02529
$n = 13, 14, 15$	0.00000	−0.03119	0.00000	0.06768	0.00000	0.05796	0.00000	0.02520
$n = 16, 17, 18$	0.00000	−0.52157	0.00000	−0.02203	0.00000	0.04614	0.00000	0.01982
$n = 19, 20, 21$	0.00000	−0.00040	0.00000	0.00090	0.00000	0.00002	0.00000	0.00000
$n = 22, 23, 24$	0.00000	−0.00543	0.00000	0.03772	0.00000	0.00979	0.00000	0.00000
$n = 25, 26, 27$	0.00000	−0.00543	0.00000	0.03788	0.00000	0.00973	0.00000	0.00000
$n = 28, 29, 30$	0.00000	−0.04928	0.00000	0.02671	0.00000	0.00597	0.00000	0.00000

APPENDIX F: FOURIER COMPONENTS OF THE INTERLAYER DISTANCE VARIATION AND PIEZOELECTRIC POTENTIAL

Below, we report the first Fourier components necessary to reconstruct the interlayer distance modulation [Eq. (4)] and piezoelectric potential [Eq. (31)] for twisted P and AP WSe$_2$ bilayers, and the in-plane relaxation field [Eq. (41)] for P bilayers. In all cases, the monolayer basis Bragg vectors are defined as

$$\mathbf{G}_1 = \frac{4\pi}{\sqrt{3}a}\left(\frac{\sqrt{3}}{2}\hat{\mathbf{x}} + \frac{1}{2}\hat{\mathbf{y}}\right),$$

$$\mathbf{G}_2 = \frac{4\pi}{\sqrt{3}a}\left(-\frac{\sqrt{3}}{2}\hat{\mathbf{x}} + \frac{1}{2}\hat{\mathbf{y}}\right). \tag{F1}$$

The basis moiré Bragg vectors for twist angle $\theta \ll 1$ (in radians) are then defined as

$$\mathbf{g}_1 \equiv \theta(G_{1,y}\hat{\mathbf{x}} - G_{1,x}\hat{\mathbf{y}}) \approx (1 - \mathcal{R}_\theta)\mathbf{G}_1,$$

$$\mathbf{g}_2 \equiv \theta(G_{2,y}\hat{\mathbf{x}} - G_{2,x}\hat{\mathbf{y}}) \approx (1 - \mathcal{R}_\theta)\mathbf{G}_2. \tag{F2}$$

Note that $\mathbf{G}_2 = C_3\mathbf{G}_1$ and $\mathbf{g}_2 = C_3\mathbf{g}_2$, and we can define additional vectors $\mathbf{G}_3 = C_3^2\mathbf{G}_1$ and $\mathbf{g}_3 = C_3^2\mathbf{g}_1$. Together, $\mathbf{G}_1$, $\mathbf{G}_2$, $\mathbf{G}_3$ ($\mathbf{g}_1$, $\mathbf{g}_2$, $\mathbf{g}_3$) form the first star of (moiré) Bragg vectors. Higher stars of moiré vectors are generated as

$$\mathbf{g}_{3n+2} = C_3\mathbf{g}_{3n+1}, \quad \mathbf{g}_{3n+3} = C_3^2\mathbf{g}_{3n+1}, \, n = 0, 1, 2, \ldots, \tag{F3}$$

TABLE XVI. Coefficients of the moiré harmonics expansion Eq. (31) for the piezoelectric potential $\varphi(\mathbf{r})$, for AP bilayers with different twist angles. The top- and bottom-layer potential coefficients are given by $\varphi_n^t = \varphi_n^b = \varphi_n$. All values are in units of mV.

	$\theta_{\mathrm{AP}} = 1.4°$		$\theta_{\mathrm{AP}} = 2.0°$		$\theta_{\mathrm{AP}} = 3.0°$		$\theta_{\mathrm{AP}} = 4.0°$	
	Re φ_n	Im φ_n	Re φ_n	Im φ_n	Re φ_n	Im φ_n	Re φ_n	Im φ_n
$n = 0$	0.00000	0.00000	0.00000	0.00000	0.00000	0.00000	0.00000	0.00000
$n = 1, 2, 3$	−6.61064	14.27250	−6.87717	11.26287	−4.64673	6.26576	−2.89876	3.65027
$n = 4, 5, 6$	0.76037	−0.04281	0.20305	−0.00240	0.01545	0.00166	−0.00019	0.00041
$n = 7, 8, 9$	2.14124	−1.28374	1.30934	−0.51315	0.14263	−0.09730	−0.04870	−0.02681
$n = 10, 11, 12$	−0.28241	−0.10708	−0.01306	−0.03063	0.03092	0.02756	0.01409	0.01381
$n = 13, 14, 15$	−0.30460	0.11894	−0.01335	0.03088	0.03070	−0.02760	0.01403	−0.01380
$n = 16, 17, 18$	−0.54968	−0.05502	−0.16047	0.00781	0.01366	0.02401	0.01061	0.00995
$n = 19, 20, 21$	0.01943	−0.00310	−0.00039	−0.00202	0.00196	−0.00096	0.00162	−0.00099
$n = 22, 23, 14$	0.09423	−0.02802	−0.07428	0.08013	−0.03231	0.02338	−0.01548	0.01025
$n = 25, 26, 27$	0.10478	−0.03522	−0.01666	−0.01082	−0.00502	−0.00678	−0.00194	−0.00352
$n = 28, 29, 30$	0.13256	0.06584	0.01107	0.01535	−0.00211	0.01218	−0.00192	0.00883
$n = 31, 32, 33$	0.01198	0.00096	0.00000	0.00000	0.00000	0.00000	0.00000	0.00000
$n = 34, 35, 36$	0.00965	−0.00181	0.00000	0.00000	0.00000	0.00000	0.00000	0.00000
$n = 37, 38, 39$	−0.00539	−0.02158	0.00000	0.00000	0.00000	0.00000	0.00000	0.00000
$n = 40, 41, 42$	−0.01071	0.02171	0.00000	0.00000	0.00000	0.00000	0.00000	0.00000

TABLE XVII. Coefficients of the moiré harmonics expansion Eq. (41) for the in-plane displacement field $\mathbf{u}^t(\mathbf{r}) - \mathbf{u}^b(\mathbf{r})$, for P bilayers with different twist angles. All values are in units of 10^{-2} Å.

	$\theta_P = 1.4°$		$\theta_P = 2.0°$		$\theta_P = 3.0°$		$\theta_P = 4.0°$	
	$u_{n,x}$	$u_{n,y}$	$u_{n,x}$	$u_{n,y}$	$u_{n,x}$	$u_{n,y}$	$u_{n,x}$	$u_{n,y}$
$n = 0$	0.00000	0.00000	0.00000	0.00000	0.00000	0.00000	0.00000	0.00000
$n = 1, 2, 3$	32.10502	18.54762	24.52676	14.12421	13.51045	7.79985	7.75407	4.47794
$n = 4, 5, 6$	0.09762	0.00252	0.10202	−0.01842	−0.74473	−0.00429	−0.73187	−0.00097
$n = 7, 8, 9$	4.76970	2.75402	1.79569	0.51747	0.04853	0.02943	−0.19064	−0.10945
$n = 10, 11, 12$	−0.02784	0.05540	−0.11962	−0.25275	−0.07374	−0.19879	−0.03032	−0.08454
$n = 13, 14, 15$	0.06456	0.00422	−0.16781	−0.23527	−0.13555	−0.16468	−0.05791	−0.06877
$n = 16, 17, 18$	0.90220	0.52294	0.03769	0.02018	−0.07590	−0.04364	−0.03225	−0.01850
$n = 19, 20, 21$	0.00744	0.01132	−0.06797	−0.11426	−0.01627	−0.02812	−0.00573	−0.01457
$n = 22, 23, 24$	0.01042	0.00646	−0.06962	−0.07217	−0.01777	−0.01755	0.06136	0.03422
$n = 25, 26, 27$	0.01028	0.00614	−0.09693	−0.02481	−0.02398	−0.00656	−0.00433	0.00763
$n = 28, 29, 30$	0.08308	0.04820	−0.04402	−0.02567	−0.00973	−0.00556	0.01205	0.00590

where the reference vectors $\mathbf{g}_1, \mathbf{g}_4, \ldots, \mathbf{g}_{3n+1}, \ldots$ are listed in Table XII in the form

$$\mathbf{g}_{3n+1} = m_1^{(3n+1)}\mathbf{g}_1 + m_2^{(3n+1)}\mathbf{g}_2. \qquad \text{(F4)}$$

Tables XIII–XVII list the expansion coefficients for the interlayer distance variation, piezoelectric potential and in-plane displacement field, associated with the $\mathbf{g}_n$ moiré vectors.

[1] L. J. McGilly, A. Kerelsky, N. R. Finney, K. Shapovalov, E.-M. Shih, A. Ghiotto, Y. Zeng, S. L. Moore, W. Wu, Y. Bai, K. Watanabe, T. Taniguchi, M. Stengel, L. Zhou, J. Hone, X. Zhu, D. N. Basov, C. Dean, C. E. Dreyer, and A. N. Pasupathy, Visualization of moiré superlattices, Nat. Nanotechnol. **15**, 580 (2020).

[2] Y. Cao, V. Fatemi, S. Fang, K. Watanabe, T. Taniguchi, E. Kaxiras, and P. Jarillo-Herrero, Unconventional superconductivity in magic-angle graphene superlattices, Nature (London) **556**, 43 (2018).

[3] Y. Cao, V. Fatemi, A. Demir, S. Fang, S. L. Tomarken, J. Y. Luo, J. D. Sanchez-Yamagishi, K. Watanabe, T. Taniguchi, E. Kaxiras *et al.*, Correlated insulator behaviour at half-filling in magic-angle graphene superlattices, Nature (London) **556**, 80 (2018).

[4] M. Yankowitz, S. Chen, H. Polshyn, Y. Zhang, K. Watanabe, T. Taniguchi, D. Graf, A. F. Young, and C. R. Dean, Tuning superconductivity in twisted bilayer graphene, Science **363**, 1059 (2019).

[5] Z. Zhang, Y. Wang, K. Watanabe, T. Taniguchi, K. Ueno, E. Tutuc, and B. J. LeRoy, Flat bands in twisted bilayer transition metal dichalcogenides, Nat. Phys. **16**, 1093 (2020).

[6] L. Wang, E.-M. Shih, A. Ghiotto, L. Xian, D. A. Rhodes, C. Tan, M. Claassen, D. M. Kennes, Y. Bai, B. Kim, K. Watanabe, T. Taniguchi, X. Zhu, J. Hone, A. Rubio, A. N. Pasupathy, and C. R. Dean, Correlated electronic phases in twisted bilayer transition metal dichalcogenides, Nat. Mater. **19**, 861 (2020).

[7] H. Pan and S. Das Sarma, Interaction-Driven Filling-Induced Metal-Insulator Transitions in 2D Moiré Lattices, Phys. Rev. Lett. **127**, 096802 (2021).

[8] N. Morales-Durán, A. H. MacDonald, and P. Potasz, Metal-insulator transition in transition metal dichalcogenide heterobilayer moiré superlattices, Phys. Rev. B **103**, L241110 (2021).

[9] T. Li, S. Jiang, L. Li, Y. Zhang, K. Kang, J. Zhu, K. Watanabe, T. Taniguchi, D. Chowdhury, L. Fu, J. Shan, and K. F. Mak, Continuous Mott transition in semiconductor moiré superlattices, Nature, **597**, 350, (2021).

[10] A. Ghiotto, E.-M. Shih, G. S. S. G. Pereira, D. A. Rhodes, B. Kim, J. Zang, A. J. Millis, K. Watanabe, T. Taniguchi, J. C. Hone, L. Wang, C. R. Dean, and A. N. Pasupathy, Quantum criticality in twisted transition metal dichalcogenides, Nature, **597**, 345, (2021).

[11] E. M. Alexeev, D. A. Ruiz-Tijerina, M. Danovich, M. J. Hamer, D. J. Terry, P. K. Nayak, S. Ahn, S. Pak, J. Lee, J. I. Sohn, M. R. Molas, M. Koperski, K. Watanabe, T. Taniguchi, K. S. Novoselov, R. V. Gorbachev, H. S. Shin, V. I. Fal'ko, and A. I. Tartakovskii, Resonantly hybridized excitons in moiré superlattices in van der Waals heterostructures, Nature (London) **567**, 81 (2019).

[12] C. Jin, E. C. Regan, A. Yan, M. I. B. Utama, D. Wang, S. Zhao, Y. Qin, S. Yang, Z. Zheng, S. Shi *et al.*, Observation of moiré excitons in WSe₂/WS₂ heterostructure superlattices, Nature (London) **567**, 76 (2019).

[13] P. Rivera, H. Yu, K. L. Seyler, N. P. Wilson, W. Yao, and X. Xu, Interlayer valley excitons in heterobilayers of transition metal dichalcogenides, Nat. Nanotechnol. **13**, 1004 (2018).

[14] K. Tran, G. Moody, F. Wu, X. Lu, J. Choi, K. Kim, A. Rai, D. A. Sanchez, J. Quan, A. Singh *et al.*, Evidence for moiré excitons in van der Waals heterostructures, Nature (London) **567**, 71 (2019).

[15] K. L. Seyler, P. Rivera, H. Yu, N. P. Wilson, E. L. Ray, D. G. Mandrus, J. Yan, W. Yao, and X. Xu, Signatures of moiré-trapped valley excitons in MoSe₂/WSe₂ heterobilayers, Nature (London) **567**, 66 (2019).

[16] G. Scuri, T. I. Andersen, Y. Zhou, D. S. Wild, J. Sung, R. J. Gelly, D. Bérubé, H. Heo, L. Shao, A. Y. Joe, A. M. Mier Valdivia, T. Taniguchi, K. Watanabe, M. Lončar, P. Kim, M. D.

Lukin, and H. Park, Electrically Tunable Valley Dynamics in Twisted WSe$_2$/WSe$_2$ Bilayers, Phys. Rev. Lett. **124**, 217403 (2020).

[17] J. Sung, Y. Zhou, G. Scuri, V. Zólyomi, T. I. Andersen, H. Yoo, D. S. Wild, A. Y. Joe, R. J. Gelly, H. Heo *et al.*, Broken mirror symmetry in excitonic response of reconstructed domains in twisted MoSe$_2$/MoSe$_2$ bilayers, Nat. Nanotechnol. **15**, 750 (2020).

[18] A. Weston, Y. Zou, V. Enaldiev, A. Summerfield, N. Clark, V. Zólyomi, A. Graham, C. Yelgel, S. Magorrian, M. Zhou, J. Zultak, D. Hopkinson, A. Barinov, T. H. Bointon, A. Kretinin, N. R. Wilson, P. H. Beton, V. I. Fal'ko, S. J. Haigh, and R. Gorbachev, Atomic reconstruction in twisted bilayers of transition metal dichalcogenides, Nat. Nanotechnol. **15**, 592 (2020).

[19] M. R. Rosenberger, H.-J. Chuang, M. Phillips, V. P. Oleshko, K. M. McCreary, S. V. Sivaram, C. S. Hellberg, and B. T. Jonker, Twist angle-dependent atomic reconstruction and moiré patterns in transition metal dichalcogenide heterostructures, ACS Nano **14**, 4550 (2020).

[20] D. Edelberg, H. Kumar, V. Shenoy, H. Ochoa, and A. N. Pasupathy, Tunable strain soliton networks confine electrons in van der Waals materials, Nat. Phys. **16**, 1097 (2020).

[21] S. Shabani, D. Halbertal, W. Wu, M. Chen, S. Liu, J. Hone, W. Yao, D. N. Basov, X. Zhu, and A. N. Pasupathy, Deep moiré potentials in twisted transition metal dichalcogenide bilayers, Nat. Phys. **17**, 720 (2021).

[22] V. Enaldiev, F. Ferreira, S. Magorrian, and V. I. Fal'ko, Piezoelectric networks and ferroelectric domains in twistronic superlattices in WS2/MoS2 and WSe2/MoSe2 bilayers, 2D Mater. **8**, 025030 (2021).

[23] L. Li and M. Wu, Binary compound bilayer and multilayer with vertical polarizations: Two-dimensional ferroelectrics, multiferroics, and nanogenerators, ACS Nano **11**, 6382 (2017).

[24] Q. Tong, M. Chen, F. Xiao, H. Yu, and W. Yao, Interferences of electrostatic moiré potentials and bichromatic superlattices of electrons and excitons in transition metal dichalcogenides, 2D Mater. **8**, 025007 (2020).

[25] C. R. Woods, P. Ares, H. Nevison-Andrews, M. J. Holwill, R. Fabregas, F. Guinea, A. K. Geim, K. S. Novoselov, N. R. Walet, and L. Fumagalli, Charge-polarized interfacial superlattices in marginally twisted hexagonal boron nitride, Nat. Commun., **12**, 347 (2021).

[26] M. V. Stern, Y. Waschitz, W. Cao, I. Nevo, K. Watanabe, T. Taniguchi, E. Sela, M. Urbakh, O. Hod, and M. B. Shalom, Interfacial ferroelectricity by van der Waals sliding, Science **372**, 1462 (2021).

[27] K. Yasuda, X. Wang, K. Watanabe, T. Taniguchi, and P. Jarillo-Herrero, Stacking-engineered ferroelectricity in bilayer boron nitride, Science **372**, 1458 (2021).

[28] V. V. Enaldiev, V. Zólyomi, C. Yelgel, S. J. Magorrian, and V. I. Fal'ko, Stacking Domains and Dislocation Networks in Marginally Twisted Bilayers of Transition Metal Dichalcogenides, Phys. Rev. Lett. **124**, 206101 (2020).

[29] S. Carr, D. Massatt, S. B. Torrisi, P. Cazeaux, M. Luskin, and E. Kaxiras, Relaxation and domain formation in incommensurate two-dimensional heterostructures, Phys. Rev. B **98**, 224102 (2018).

[30] M. H. Naik and M. Jain, Ultraflatbands and Shear Solitons in Moiré Patterns of Twisted Bilayer Transition Metal Dichalcogenides, Phys. Rev. Lett. **121**, 266401 (2018).

[31] H. Fan, The fermion-ladder models: Extensions of the Hubbard model with η-pairing, J. Phys. A **32**, L509 (1999).

[32] A. Kormányos, G. Burkard, M. Gmitra, J. Fabian, V. Zólyomi, N. D. Drummond, and V. Fal'ko, k·p theory for two-dimensional transition metal dichalcogenide semiconductors, 2D Mater. **2**, 022001 (2015).

[33] F. Ferreira, S. J. Magorrian, V. V. Enaldiev, D. A. Ruiz-Tijerina, and V. I. Fal'ko, Band energy landscapes in twisted homobilayers of transition metal dichalcogenides, Appl. Phys. Lett. **118**, 241602 (2021).

[34] W. Schutte, J. De Boer, and F. Jellinek, Crystal structures of tungsten disulfide and diselenide, J. Solid State Chem. **70**, 207 (1987).

[35] J. Klimeš, D. R. Bowler, and A. Michaelides, Van der Waals density functionals applied to solids, Phys. Rev. B **83**, 195131 (2011).

[36] H. Rostami, F. Guinea, M. Polini, and R. Roldán, Piezoelectricity and valley Chern number in inhomogeneous hexagonal 2D crystals, npj 2D Mater. Appl. **2**, 15 (2018).

[37] F. Ferreira, V. V. Enaldiev, V. I. Fal'ko, and S. J. Magorrian, Weak ferroelectric charge transfer in layer-asymmetric bilayers of 2D semiconductors, Sci. Rep. **11**, 13422 (2021).

[38] The final expression in Eqs. (9) follows from even parity of the Hamiltonian Eq. (7) with respect to $\boldsymbol{r}_0 \to -\boldsymbol{r}_0$, for P-aligned bilayers (see Appendix B). We note here that for AP-bilayers the asymmetry of the Hamiltonian Eq. (7) with respect to $\boldsymbol{r}_0$ is only expressed in a small term $\propto t_2^{\mathrm{AP}}$.

[39] D. Xiao, G.-B. Liu, W. Feng, X. Xu, and W. Yao, Coupled Spin and Valley Physics in Monolayers of MoS$_2$ and Other Group-VI Dichalcogenides, Phys. Rev. Lett. **108**, 196802 (2012).

[40] H. Zeng, G.-B. Liu, J. Dai, Y. Yan, B. Zhu, R. He, L. Xie, S. Xu, X. Chen, W. Yao *et al.*, Optical signature of symmetry variations and spin-valley coupling in atomically thin tungsten dichalcogenides, Sci. Rep. **3**, 1608 (2013).

[41] The form of V_3 is chosen to describe at large distances the potential of three 120°-rotated domain walls intersecting at the same XX' region. For $r \gg \rho_1$ and $|\delta\phi| = |\phi - 2\pi n/3| \ll 1$ ($n = 1, 2, 3$), we can characterize the potential cross-section of a single domain wall as $V_3 \approx (V_1 - V_2\sqrt{\beta^2 + 9\xi^2/2l^2})/(1 + 9\xi^2/2l^2)^{1.5}$, where $\xi = r\delta\phi$. Then, the relation between parameters $V_{1,2}$ and β is governed by the condition that the total potential across a domain wall vanishes, i.e., $\int_{-\infty}^{+\infty} V_3 d\xi = 0$.

[42] F. Wu, T. Lovorn, E. Tutuc, and A. H. MacDonald, Hubbard Model Physics in Transition Metal Dichalcogenide Moiré bands, Phys. Rev. Lett. **121**, 026402 (2018).

[43] E. Codecido, Q. Wang, R. Koester, S. Che, H. Tian, R. Lv, S. Tran, K. Watanabe, T. Taniguchi, F. Zhang, M. Bockrath, and C. N. Lau, Correlated insulating and superconducting states in twisted bilayer graphene below the magic angle, Sci. Adv. **5**, 9770 (2019).

[44] W. Jin, P.-C. Yeh, N. Zaki, D. Zhang, J. T. Sadowski, A. Al-Mahboob, A. M. van der Zande, D. A. Chenet, J. I. Dadap, I. P. Herman, P. Sutter, J. Hone, and R. M. Osgood, Direct Measurement of the Thickness-Dependent Electronic Band Structure of MoS$_2$ using Angle-Resolved Photoemission Spectroscopy, Phys. Rev. Lett. **111**, 106801 (2013).

[45] H. Yang, A. Liang, C. Chen, C. Zhang, N. B. M. Schroeter, and Y. Chen, Visualizing electronic structures of quantum materials by angle-resolved photoemission spectroscopy, Nat. Rev. Mater. **3**, 341 (2018).

[46] Y. Zhang, T.-R. Chang, B. Zhou, Y.-T. Cui, H. Yan, Z. Liu, F. Schmitt, J. Lee, R. Moore, Y. Chen *et al.*, Direct observation of the transition from indirect to direct bandgap in atomically thin epitaxial mose 2, Nat. Nanotechnol. **9**, 111 (2014).

[47] $C_3 \psi_{VB,\tau K}(\boldsymbol{r}) = e^{\tau K \cdot C_3^{-1} \boldsymbol{r}} u_{VB,\tau K}(C_3^{-1} \boldsymbol{r}) = e^{i\tau \frac{4\pi}{3}} e^{i\tau (K+G_2) \cdot \boldsymbol{r}} u_{VB,\tau K}(\boldsymbol{r})$; $C_3 \psi_{CB,\tau K}(\boldsymbol{r}) = e^{i\tau K \cdot (C_3^{-1} \boldsymbol{r} - \boldsymbol{r}_0)} u_{CB,\tau K}(C_3^{-1} \boldsymbol{r} - \boldsymbol{r}_0) = e^{i\tau (K+G_2) \cdot (\boldsymbol{r} - \boldsymbol{r}_0 + \boldsymbol{a}_1)} u_{CB,\tau K}(\boldsymbol{r} - \boldsymbol{r}_0 + \boldsymbol{a}_1) = e^{i\tau \frac{2\pi}{3} + i\tau G_2 \cdot (\boldsymbol{r} - \boldsymbol{r}_0)} e^{i\tau K \cdot (\boldsymbol{r} - \boldsymbol{r}_0)} u_{CB,\tau K}(\boldsymbol{r} - \boldsymbol{r}_0) = e^{iG_2 \cdot \boldsymbol{r}} e^{i\tau K \cdot (\boldsymbol{r} - \boldsymbol{r}_0)} u_{CB,\tau K}(\boldsymbol{r} - \boldsymbol{r}_0)$, where in the last equality we substituted $\boldsymbol{r}_0 = (0, a/\sqrt{3})$, corresponding to XM' stacking.

[48] D. A. Ruiz-Tijerina and V. I. Fal'ko, Interlayer hybridization and moiré superlattice minibands for electrons and excitons in heterobilayers of transition-metal dichalcogenides, Phys. Rev. B **99**, 125424 (2019).

[49] More precisely, these states correspond to the A_1 representation of the C_{3v} point group of the band-edge energy about 2H sites [78].

[50] These states belong to the E representation of group C_{3v}, as discussed in Ref. [78].

[51] M. Angeli and A. H. MacDonald, γ valley transition metal dichalcogenide moiré bands, Proc. Natl. Acad. Sci. USA **118**, 826118 (2021).

[52] Y. Tang, L. Li, T. Li, Y. Xu, S. Liu, K. Barmak, K. Watanabe, T. Taniguchi, A. H. MacDonald, J. Shan, and K. F. Mak, Simulation of Hubbard model physics in WSe$_2$/WS$_2$ moirésuperlattices, Nature (London) **579**, 353 (2020).

[53] Y. Xu, S. Liu, D. A. Rhodes, K. Watanabe, T. Taniguchi, J. Hone, V. Elser, K. F. Mak, and J. Shan, Correlated insulating states at fractional fillings of moiré superlattices, Nature (London) **587**, 214 (2020).

[54] Y.-H. Zhang and D. Mao, Spin liquids and pseudogap metals in the su(4) Hubbard model in a moiré superlattice, Phys. Rev. B **101**, 035122 (2020).

[55] J. B. Marston and I. Affleck, Large-*n* limit of the Hubbard-Heisenberg model, Phys. Rev. B **39**, 11538 (1989).

[56] L. Wang, A. Kutana, and B. I. Yakobson, Many-body and spin-orbit effects on direct-indirect band gap transition of strained monolayer MoS2 and WS2, Ann. Phys. **526**, L7 (2014).

[57] A. Steinhoff, M. Rösner, F. Jahnke, T. O. Wehling, and C. Gies, Influence of excited carriers on the optical and electronic properties of MoS2, Nano Lett. **14**, 3743 (2014).

[58] R. Roldán, A. Castellanos-Gomez, E. Cappelluti, and F. Guinea, Strain engineering in semiconducting two-dimensional crystals, J. Phys.: Condens. Matter **27**, 313201 (2015).

[59] S. Horzum, H. Sahin, S. Cahangirov, P. Cudazzo, A. Rubio, T. Serin, and F. M. Peeters, Phonon softening and direct to indirect band gap crossover in strained single-layer MoSe$_2$, Phys. Rev. B **87**, 125415 (2013).

[60] M. Ghorbani-Asl, S. Borini, A. Kuc, and T. Heine, Strain-dependent modulation of conductivity in single-layer transition-metal dichalcogenides, Phys. Rev. B **87**, 235434 (2013).

[61] R. Frisenda, M. Drüppel, R. Schmidt, S. M. de Vasconcellos, D. P. de Lara, R. Bratschitsch, M. Rohlfing, and A. Castellanos-Gomez, Biaxial strain tuning of the optical properties of single-

[62] K. Zollner, Paulo E. Faria Junior, and J. Fabian, Strain-tunable orbital, spin-orbit, and optical properties of monolayer transition-metal dichalcogenides, Phys. Rev. B **100**, 195126 (2019).

[63] Y. Yan, S. Ding, X. Wu, J. Zhu, D. Feng, X. Yang, and F. Li, Tuning the physical properties of ultrathin transition-metal dichalcogenides via strain engineering, RSC Adv. **10**, 39455 (2020).

[64] S. B. Desai, G. Seol, J. S. Kang, H. Fang, C. Battaglia, R. Kapadia, J. W. Ager, J. Guo, and A. Javey, Strain-induced indirect to direct bandgap transition in multilayer WSe2, Nano Lett. **14**, 4592 (2014).

[65] W. Shi, J. Ye, Y. Zhang, R. Suzuki, M. Yoshida, J. Miyazaki, N. Inoue, Y. Saito, and Y. Iwasa, Superconductivity series in transition metal dichalcogenides by ionic gating, Sci. Rep. **5**, 12534 (2015).

[66] E. Mostaani, M. Szyniszewski, C. H. Price, R. Maezono, M. Danovich, R. J. Hunt, N. D. Drummond, and V. I. Fal'ko, Diffusion quantum monte carlo study of excitonic complexes in two-dimensional transition-metal dichalcogenides, Phys. Rev. B **96**, 075431 (2017).

[67] T. C. Berkelbach, M. S. Hybertsen, and D. R. Reichman, Theory of neutral and charged excitons in monolayer transition metal dichalcogenides, Phys. Rev. B **88**, 045318 (2013).

[68] K.-L. Barth, W. Fukarek, H.-P. Maucher, M. Plass, and A. Lunk, In situ characterization of cubic boron nitride film growth in the ir spectral region, Thin Solid Films **313**, 697 (1998).

[69] C. R. Dean, A. F. Young, I. Meric, C. Lee, L. Wang, S. Sorgenfrei, K. Watanabe, T. Taniguchi, P. Kim, K. L. Shepard, and J. Hone, Boron nitride substrates for high-quality graphene electronics, Nat. Nanotechnol. **5**, 722 (2010).

[70] G.-H. Lee, Y.-J. Yu, X. Cui, N. Petrone, C.-H. Lee, M. S. Choi, D.-Y. Lee, C. Lee, W. J. Yoo, K. Watanabe, T. Taniguchi, C. Nuckolls, P. Kim, and J. Hone, Flexible and transparent MoS2 field-effect transistors on hexagonal boron nitride-graphene heterostructures, ACS Nano **7**, 7931 (2013).

[71] A. V. Kretinin, Y. Cao, J. S. Tu, G. L. Yu, R. Jalil, K. S. Novoselov, S. J. Haigh, A. Gholinia, A. Mishchenko, M. Lozada, T. Georgiou, C. R. Woods, F. Withers, P. Blake, G. Eda, A. Wirsig, C. Hucho, K. Watanabe, T. Taniguchi, A. K. Geim *et al.*, Electronic properties of graphene encapsulated with different two-dimensional atomic crystals, Nano Lett. **14**, 3270 (2014).

[72] D. A. Bandurin, A. V. Tyurnina, G. L. Yu, A. Mishchenko, V. Zólyomi, S. V. Morozov, R. K. Kumar, R. V. Gorbachev, Z. R. Kudrynskyi, S. Pezzini, Z. D. Kovalyuk, U. Zeitler, K. S. Novoselov, A. Patanè, L. Eaves, I. V. Grigorieva, V. I. Falko, A. K. Geim, and Y. Cao, High electron mobility, quantum hall effect and anomalous optical response in atomically thin InSe, Nat. Nanotechnol. **12**, 223 (2016).

[73] S. Ogawa, T. Yamada, R. Kadowaki, T. Taniguchi, T. Abukawa, and Y. Takakuwa, Band alignment determination of bulk h-BN and graphene/h-BN laminates using photoelectron emission microscopy, J. Appl. Phys. **125**, 144303 (2019).

[74] N. R. Wilson, P. V. Nguyen, K. Seyler, P. Rivera, A. J. Marsden, Z. P. Laker, G. C. Constantinescu, V. Kandyba, A. Barinov, N. D. Hine, X. Xu, and D. H. Cobden, Determination of band offsets, hybridization, and exciton binding

in 2D semiconductor heterostructures, Sci. Adv. **3**, e1601832 (2017).

[75] J. H. Park, S. Vishwanath, X. Liu, H. Zhou, S. M. Eichfeld, S. K. Fullerton-Shirey, J. A. Robinson, R. M. Feenstra, J. Furdyna, D. Jena, H. G. Xing, and A. C. Kummel, Scanning tunneling microscopy and spectroscopy of air exposure effects on molecular beam epitaxy grown WSe2 monolayers and bilayers, ACS Nano **10**, 4258 (2016).

[76] M. Masseroni, T. Davatz, R. Pisoni, F. K. de Vries, P. Rickhaus, T. Taniguchi, K. Watanabe, V. Fal'ko, T. Ihn, and K. Ensslin, Electron transport in dual-gated three-layer Mos₂, Phys. Rev. Research **3**, 023047 (2021).

[77] N. Ubrig, E. Ponomarev, J. Zultak, D. Domaretskiy, V. Zólyomi, D. Terry, J. Howarth, I. Gutiérrez-Lezama, A. Zhukov, Z. R. Kudrynskyi, Z. D. Kovalyuk, A. Patané, T. Taniguchi, K. Watanabe, R. V. Gorbachev, V. I. Fal'ko, and A. F. Morpurgo, Design of van der Waals interfaces

for broad-spectrum optoelectronics, Nat. Mater. **19**, 299 (2020).

[78] D. A. Ruiz-Tijerina, I. Soltero, and F. Mireles, Theory of moiré localized excitons in transition metal dichalcogenide heterobilayers, Phys. Rev. B **102**, 195403 (2020).

[79] J. M. Luttinger and W. Kohn, Motion of electrons and holes in perturbed periodic fields, Phys. Rev. **97**, 869 (1955).

[80] G. Kresse and J. Furthmüller, Efficient iterative schemes for *ab initio* total-energy calculations using a plane-wave basis set, Phys. Rev. B **54**, 11169 (1996).

[81] J. P. Perdew, K. Burke, and M. Ernzerhof, Generalized Gradient Approximation Made Simple, Phys. Rev. Lett. **77**, 3865 (1996).

[82] A. Laturia, M. L. Van de Put, and W. G. Vandenberghe, Dielectric properties of hexagonal boron nitride and transition metal dichalcogenides: From monolayer to bulk, npj 2D Mater. Appl. **2**, 6 (2018).

[83] https://www.archer2.ac.uk.